



# **Adsorption of molecular thin films on metal and metal oxide surfaces**

ZAHRA BESHARAT

Doctoral Thesis in physics  
School of Information and Communication Technology  
KTH Royal Institute of Technology  
Stockholm, Sweden, 2016

TRITA-ICT 2016:37  
ISBN 978-91-7729-178-7

KTH School of Information and  
Communication Technology  
SE-164 40 Kista  
SWEDEN

Akademisk avhandling som med tillstånd av Kungl Tekniska högskolan framlägges till offentlig granskning för avläggande av doktorsexamen i fysik fredag den 9 December 2016 klockan 10.00 i Sal C , Electrum, Kungl Tekniska högskolan, Kistagången 16, Kista.

© Zahra Besharat 2016

Tryck: Universitetsservice US AB

*“Be happy for this moment. This moment is your life.”*

*Omar Khayyam*



## Abstract

Metal and metal oxides are widely used in industry, and to optimize their performance their surfaces are commonly functionalized by the formation of thin films. Self-assembled monolayers (SAMs) are deposited on metals or metal oxides either from solution or by gas deposition. The gas deposition enables the preparation of SAMs under very well controlled conditions in ultrahigh vacuum (UHV).

Thiols with polar terminal groups are utilized for creating the responsive surfaces which can interact electrostatically with other adsorbates. Surface charge affects wetting and adhesion, and many other surface properties. Polar terminal groups in thiols could be used to modify these factors. Mixed SAMs can provide more flexible surfaces, and selection of particular terminal groups in the mixed SAMs could change the resulting surface properties under the influence of factors such as pH, temperature, and photo-illumination. However, in order to control these phenomena by mixed polar-terminated thiols, it is necessary to understand the composition and conformation of the mixed SAMs and their response to these factors. In this work, mixtures of thiols with carboxylic and amino terminal groups were studied. Carboxylic and amino terminal groups of thiol interact with each other via hydrogen bonding in solution and form a complex. Complexes adsorb to the surface in non-conventional orientations. Unmixed SAMs from each type, either carboxylic terminated thiols or amino terminated thiols adsorbed on gold in standing up orientation while SAMs from complexes are in an axially in-plane orientation. The orientation of mixtures causes greater hydrophobicity. Thiolated surfaces with complexes are less responsive to the pH changes than for the unmixed thiolated surface with either carboxylic or amino termination. Contact angle changes significantly with pH change for the unmixed thiolated surfaces but there is no change in the contact angle with water on the mixed SAMs.

Selenol is an alternative to replace thiols for particular applications such as contact with biological matter which has a better compatibility with selenol than sulfur. However, the Se-C bond is weaker than the S-C bond which limits the application of selenol. Understanding the selenol adsorption mechanism on gold surfaces could shed some light on Se-C cleavage and so is investigated in this work. Se-C cleavage happens in the low coverage areas on the step since atoms at steps have lower coordination making them more reactive than atoms on the terraces. At higher dosage, the herring bone structure of the gold is lifted up, and at full coverage there is a smooth layer on the terraces.

Another area where the self-assembly of molecules is of importance is for dye sensitized solar cells, which are based on the adsorption of the dye onto metal oxides surfaces such as  $\text{TiO}_2$ . The interface between the self-assembled dye monolayer and the substrate is an important factor to consider when designing dyes and surfaces in

dye sensitized solar cells (DSSCs). The quality of the self-assembled monolayers of the dye on the  $\text{TiO}_2$  surface has a critical influence on the efficiency of the DSSCs. Creation of just a monolayer of dye on the surface could lead to an efficient current of photo-excited electrons to the  $\text{TiO}_2$  and degeneration of the dye by redox. On the other hand, multilayer formation or aggregation of dyes on the  $\text{TiO}_2$  surface causes indirect contact between the dye molecules and the surface, which reduces the efficiency of the DSSCs. Therefore, it is very important to investigate the amount of dye adsorption on the surface. In this work, T-PAC dye showed island growth with some ad-layer that is not in contact with the surface, whereas the MP13 dye adsorption occurs through laminar growth. Results for the sublimated samples were similar to those for the sample with deposition from a dye solution, except for the existence of water in the latter sample.

Cuprite ( $\text{Cu}_2\text{O}$ ) is an important initial and common corrosion product on copper under atmospheric conditions. Copper could be a good replacement for noble metal as catalysts for methanol dehydrogenation. Knowledge about the structure of  $\text{Cu}_2\text{O}(100)$  and  $\text{Cu}_2\text{O}(111)$  surfaces could be used to obtain a deeper understanding of methanol dehydrogenation mechanisms with respect to adsorption sites on the surfaces. In this work, a detailed study was done of  $\text{Cu}_2\text{O}(100)$  surface which revealed the possible surface structures as the result of different preparation conditions. Studies of the structure of  $\text{Cu}_2\text{O}(100)$  and  $\text{Cu}_2\text{O}(111)$  surfaces show that  $\text{Cu}_2\text{O}(100)$  has a comparatively stable surface and reduces surface reactivity. As a consequence, dehydrogenation of methanol is more efficient on the  $\text{Cu}_2\text{O}(111)$  surface. The hydrogen produced from methanol dehydrogenation is stored in oxygen adatom sites on both surfaces.

**Keywords :** Self assembled monolayer (SAM), dye synthesis solar cell (DSSC), thiol, selenol,  $\text{Cu}_2\text{O}(100)$ ,  $\text{Cu}_2\text{O}(111)$  and dehydrogenation

## Sammanfattning

Metaller och metalloxider har otaliga användningsområden inom industrin och för att optimera deras prestanda funktionaliseras ofta deras ytor med tunna beläggningar. Självassocierade monoskikt (SAMs) har här deponerats på metaller eller metalloxider, antingen från en lösning eller via gasdeponering. Den senare metoden möjliggör deponering av ett SAM i en väl kontrollerad miljö i ultrahögt vakuum (UHV).

Tioler med polära ändgrupper används ofta för att skapa responsiva ytor som elektrostatiskt kan samverka med andra adsorbat. Ytladdningen påverkar till exempel vätning och adhesion, men även många andra ytegenskaper. SAMs bestående av en blandning av olika typer av molekyler ger större möjligheter att skapa en yta med önskade egenskaper och med olika val av ändgrupper på molekylerna kan ytegenskaperna ändras med till exempel pH-värde, temperatur och belysning med ljus. För att kunna kontrollera ytans egenskaper när den till exempel är täckt med ett monoskikt av tioler med polära ändgrupper är det nödvändigt att ha kännedom om sammansättningen på ytan och även hur molekylerna är packade, som funktion av ovan nämnda parametrar. I denna avhandling har tioler med ändgrupper av karboxylsyra- och aminergrupper studerats. Blandningar av tioler med dessa ändgrupper binder till varandra med vätebindningar i lösning och bildar ett komplex och detta komplex adsorberar på ytan och orienterar sig på ett icke-konventionellt sätt. Monoskikt bestående av tioler med antingen karboxyl- eller aminändgrupper står upp på ytan, medan komplexen tenderar att ligga ned på ytan. Denna orientering av komplexen resulterar i att ytan blir mer hydrofob. Ytor med adsorberade komplex påverkas mindre av pH-ändringar än ytor belagda med endast en av de två tiolerna. Kontaktvinkeln ändras avsevärt när pH-värdet ändras för de icke blandade tiolerna, medan för blandningen av karboxyl- och aminioler så ändras inte kontaktvinkeln med vatten.

Selenoler är i vissa tillämpningar ett alternativ till tioler, till exempel i kontakt med biologiska material eftersom selenium i detta fall är mer kompatibelt än svavel som tiolerna innehåller. Dock är Se-C-bindningen svagare än S-C-bindningen, vilket begränsar användningsområdena för selenoler. En ökad förståelse av hur selenoler adsorberar på guldtytor kan leda till en djupare insikt om hur Se-C-bindningen klyvs och har därför undersökts i denna studie. Klyvning av Se-C-bindningen sker på områden med låg täckningsgrad på stegkanter eftersom atomerna på stegkanter har lägre koordinationsantal än atomerna på terrasser. Vid hög dosering av selenolen har guldatomerna inte längre fiskbensstruktur och vid full täckningsgrad bildar selenolen ett jämnt lager på terrasserna.

Ett annat område där spontant adsorberande molekyler är viktiga är i färgämnessolceller (DSSCs), som baseras på adsorption av färgmolekyler på metalloxidytor som till exempel  $\text{TiO}_2$ . Egenskaperna hos gränssytan mellan de

spontant adsorberade färgmolekylerna och substratet är av stor vikt vid design av färgmolekyler och substrat för solcellerna. Kvaliteten på monoskiktet av färgmolekyler på  $\text{TiO}_2$ -ytan är av stor betydelse för effektiviteten av solcellen. Bildandet av endast ett monoskikt av färgmolekyler på titandioxytan leder till en effektiv ström av fotoexciterade elektroner till titandioxiden och regenerering av färgmolekylerna av redoxämnet. Däremot, om multiskikt skapas eller om aggregering av färgmolekylerna sker på titandioxytan, så bildas en indirekt kontakt mellan färgmolekylerna och ytan, vilket reducerar effekten av solcellen. Det är därför av yttersta vikt att undersöka hur mycket av färgämnet som adsorberar på  $\text{TiO}_2$ -ytan. I denna studie bildade färgmolekylen T-PAC öar på ytan med även ett lager som inte var i kontakt med ytan, medan MP13 adsorberade med laminär tillväxt. Resultaten för adsorption via sublimering och via en lösning var liknande, förutom att den senare metoden innebar att vatten fanns på ytan.

Kuprit ( $\text{Cu}_2\text{O}$ ) är en viktig initial och vanlig korrosionsprodukt i atmosfärisk korrosion. För dehydrogenering av metanol kan koppar vara ett alternativ till katalysatorer av ädelmetaller och en ökad kunskap om ytstrukturen av  $\text{Cu}_2\text{O}(100)$  och  $\text{Cu}_2\text{O}(111)$  är värdefull för att uppnå en djupare förståelse av mekanismerna bakom dehydrogenering av metanol på olika adsorptionsplatser på ytan. Olika ytstrukturer av  $\text{Cu}_2\text{O}(100)$  observerades beroende på hur ytan preparerades. Studierna visar även att ytstrukturen av  $\text{Cu}_2\text{O}(100)$  är stabilare och reducerar ytreaktiviteten jämfört med  $\text{Cu}_2\text{O}(111)$ . En konsekvens av detta är att dehydrogenering av metanol är effektivare på ytan av  $\text{Cu}_2\text{O}(111)$  än  $\text{Cu}_2\text{O}(100)$ . Det väte som bildas vid dehydrogeneringen lagras på syreatomer på båda ytorna.

**Nyckelord :** självassocierade monoskikt (SAM), färgämnessolceller (DSSC), tiol, selenol,  $\text{Cu}_2\text{O}(100)$  ,  $\text{Cu}_2\text{O}(111)$  and dehydrogenering



## List of appended papers

This thesis is based on the following papers referred to in the text by their Roman numerals:

- I. **Mixed monolayers of alkanethiols with polar terminal group on gold: investigation of structure dependent surface properties**  
Z. Besharat, D. Wakeham, M. Johnson, G.S. Luengo, A. Greaves, I. Wallinder, M. Göthelid and M.W. Rutland., Journal of Colloid and Interface Science, **2016**, 484, 279-290
- II. **Se-C cleavage of hexane selenol at steps on Au(111)**  
Z. Besharat, M. G.Yazdi, D. Wakeham, M. Johnson, M.W. Rutland and M. Göthelid., Manuscript
- III. **In-situ evaluation of dye adsorption on TiO<sub>2</sub> using QCM**  
Z. Besharat, R.A. Asencio, H. Tian, Sh. Yu, M. Johnson<sup>1</sup>, M. Göthelid and M.W. Rutland., Submitted to European Physical Journal
- IV. **The Surface Structure of Cu<sub>2</sub>O(100)** M.  
 Soldemo, J.H. Stenlid, Z. Besharat, M. G.Yazdi, A. Önstén, Ch. Leygraf, M. Göthelid, T. Brinck and J. Weissenrieder., Journal of Physical Chemistry C, 2016, 120 (8), pp 4373–4381
- V. **Dehydrogenation of methanol on Cu<sub>2</sub>O(100) and (111)**  
Z. Besharat, M. Soldemo, J. Halldin Stenlid, A. Önstén, C. M. Johnson, J. Weissenrieder, T. Brinck and M. Göthelid., Manuscript

The author's contribution to the papers:

- I.** Major part of planning, major part of experimental work, major part of evaluation and major part of writing.
- II.** Major part of the planning, major part of experimental work (except minor part of STM), major part of evaluation and major part of writing.
- III.** Some part of planning, major part of experimental work, major part of evaluation and major part of writing.
- IV.** Part of planning, experimental work, evaluation and minor part of writing. I have not been involved in the DFT calculations.
- V.** Major part of planning, major part of experimental work and major part of evaluation major part of writing. I have not been involved in the DFT calculations.

This thesis also contains unpublished results.

Other conference papers not included in this thesis:

- I.** ZnO nanorods/nanoflowers and their applications  
D.B. Rihtnesberg, S. Almqvist, Q. Wang, A. Sugunan, X. Yang, M. Toprak, Z. Besharat, M. Göthelid, Nanoelectronics Conference (INEC), 2011 IEEE 4th International
- II.** Plasticity effects during the 4-point bending of intramedullary leg lengthening implants with telescopic structures  
M. Kanerva · Z. Besharat · R. Livingston · M. Rutland 6th International Conference on Mechanics and Materials in Design M2D2015

## Summary of papers

### Paper I

The aim was to investigate the adsorption of mixtures of thiols with cationic (amino) AUT and anionic (carboxylic) MPA terminal groups on gold surface in order to understand the nature of the layer and its response to pH changes. The amount of the adsorption and the orientation of the thiols were measured using quartz crystal microbalance with dissipation (QCM-D), X-ray photoelectron spectroscopy (XPS), and contact angle. Atomic force microscopy (AFM) was utilized for investigations of the morphology and the mechanical properties of the surface. The results from mixture thiols (AUT/MPA) are compared with self-assembled monolayer (SAM) created by the pure compounds. The SAMs formed by unmixed thiols are ordered molecular layers. The head group (sulfur) binds to the gold surface and the alkane chains protruded out of the surface, which normally happens on thiolated surfaces. Mixed SAMs show a more complex behavior. The measurements show a lower surface concentration of thiols for the mixed SAMs in the QCM and XPS measurements, particularly for the mixture of 75% MPA and 25% AUT in comparison to the pure cases. The results indicated the presence of a complex at the surface for the mixed solutions. The thiol terminal groups (amino group from AUT and carboxylic group from MPA) interact with each other through hydrogen bonds. Therefore, the complex which has more than one head group adsorbs to the surface in parallel orientation and an axially in-plane configuration. The orientation of complex molecules in mixed layers cause the wettability of the thiolated surface to decrease and the layers are less sensitive to pH changes. The layers oriented parallel to the surface for mixed thiols are mechanically robust and resist nano shaving with an AFM tip.

### Paper II

Selenols (the sulfur atom in thiols are replaced by a selenol atom) are in some applications used as an alternative to thiols in self-assembled monolayers (SAM). Therefore the reaction of selenols with gold surfaces is an alluring subject to be investigated more. In this research, the adsorption of hexaneselenol ( $\text{CH}_3(\text{CH}_2)_5\text{SeH}$ ) on Au(111) surfaces using gas phase deposition was studied by XPS and Scanning Tunneling Microscopy (STM). We find that at very low coverages, the Se-C bond is broken at steps on Au(111). At higher dosages (mid coverage), selenol adsorbed to Au adatoms in the form of diselenoate structure. Increasing the dosage up to full coverage results in lifting of the herringbone structure of the gold surface and creation of smooth selenolate monolayers on the terraces.

### **Paper III**

Dye sensitized solar cells (DSSCs) are an alternative replacement for conventional solar cells. The amount of adsorbed dye onto the  $\text{TiO}_2$  surface is an influential parameter for optimal output of the DSSC. In this work, the adsorption mechanism of T-PAC (TriPhenylAmin-Cyanoacrylic) dye molecules and the nature of the adsorbed layer are investigated by utilizing QCM-D and XPS. The adsorbed mass was compared with another type of dye molecule MP13 (Phenoxazine) which has a molecular mass close to the TPA-C dye with a similar anchoring group, but with otherwise different chemical structure. Monitoring the adsorbed and the rinsed amount of dye as a function of dye concentration in each cycle of adsorption and rinsing, leads to conclusions about the amount of chemisorbed and physisorbed dye, as well as the determination of equilibrium constants. The adsorption mechanism reveals a laminar growth for MP13 but island growth for T-PAC. The sublimation deposited dye (T-PAC) film was compared with the film made in dye solution by XPS. The results show that the film made in solution is inhomogeneous on the  $\text{TiO}_2$  surface. The dye molecules which deposited from solution are firmly adsorbed to the surface with a small amount of dye molecules not in contact with the surface.

### **Paper IV**

$\text{Cu}_2\text{O}$  is a very important material in many industrial applications. Therefore, a good knowledge of the surface structure of  $\text{Cu}_2\text{O}$  is very important. There are several studies on  $\text{Cu}_2\text{O}$  (111) and (100) surfaces but this work is the first one where the  $\text{Cu}_2\text{O}$  (100) surface was investigated by atomically resolved microscopy. Here by the aid of low-energy electron diffraction (LEED) and STM, the surface structures relative to the bulk unit cell were identified as  $(1 \times 1)$ ,  $c(2 \times 2)$  and two  $90^\circ$  rotational domains of the matrix  $(3,0;1,1)$ . DFT calculations were in agreement with the experimental results. However the results from LEED were not in agreement with previous work from Cox et.al on the  $\text{Cu}_2\text{O}$  (100) surface. A similar LEED pattern with lots of missing points which we are experimentally and theoretically proved to be  $(3,0;1,1)$  was described by a  $(3\sqrt{2} \times \sqrt{2})R45^\circ$  structure with two  $90^\circ$  rotational domains. For having the  $(3\sqrt{2} \times \sqrt{2})R45^\circ$  unit cell with two  $90^\circ$  rotational domains the unit cell should have one side directed along one of the principle directions with the unit length and the other side with  $3\sqrt{2}/2$  unit length directed  $45^\circ$  off from the chosen principal direction. The corresponding matrix for this unit cell is  $(1,0;1.5,1.5)$ .

## Paper V

In this study, the adsorption of methanol on  $\text{Cu}_2\text{O}$  (100) and (111) has been studied by PES and simulated by DFT. The (3,0;1,1) surface structure of the (100) surface is restructured to dimer  $c(2 \times 2)$  by adsorption of methanol. Methanol, methoxy and atomic hydrogen adsorb to the Cu bridge sites. On the intermediate  $\text{O}_{\text{ad}}-c(2 \times 2)$  structure which is created during the transition of (3,0;1,1) to dimer  $c(2 \times 2)$ , the oxygen adatoms are the storage sites for atomic hydrogens from methanol dehydrogenation. On the other hand, there are several sites on the (111) surface like oxygen and copper vacancies plus surface oxygen adatoms for adsorption of methanol and its dissociative products. The oxygen adatoms are proper collecting sites for adsorption of atomic hydrogen for both (111) and (100) surfaces but to a lesser extent for the latter one. Due to the structure of the (111) surface and the variation of adsorption sites, the dehydrogenation of methanol is more effective on the (111) than the (100) surface.

## Nomenclature

### Abbreviations

AFM	Atomic force microscopy
ATR-IR	Attenuated total reflectance infrared
Avg	Average
AUT	11-Amino-1-undecanethiol hydrochloride
bcc	Body-centered cubic
Cu <sub>cs</sub>	Coordinately saturated copper
Cu <sub>cus</sub>	Coordinately unsaturated copper
CA	Contact angle
CCD	Charge-coupled device
DFT	Density functional theory
fcc	face center cube
hcp	hexagonal close-packed
L	Length, Langmuir
LEED	low energy electron diffraction
MeO	Methoxy
MeOH	Methanol
MPA	3-mercaptopropionic acid
O <sub>cs</sub>	Coordinately saturated oxygen
O <sub>cus</sub>	Coordinately unsaturated oxygen
P	Phosphor
PES	Photo Electron Spectroscopy
QCM	Quartz Crystal Microbalance
S	Sulfur
Se	Selenium
SAM	Self-Assembled Monolayer
STM	Scanning Tunneling Microscopy
SEM	Scanning electron microscope
UHV	Ultra High Vacuum
UV	Ultraviolet
XPS	X-ray photoelectron spectroscopy
Å	Ångström

# Table of Contents

<b>ABSTRACT .....</b>	<b>VI</b>
<b>SUMMARY OF PAPERS .....</b>	<b>XII</b>
<b>TABLE OF CONTENTS .....</b>	<b>XVI</b>
<b>1. INTRODUCTION .....</b>	<b>1</b>
<b>2. FUNDAMENTALS AND BACKGROUNDS .....</b>	<b>4</b>
2.1. METAL AND METAL OXIDES SURFACES .....	4
2.1.1. <i>Au(111)</i> .....	4
2.1.2. <i>TiO<sub>2</sub></i> .....	5
2.1.3. <i>Cu<sub>2</sub>O</i> .....	5
2.2. SELF-ASSEMBLED MONOLAYERS (SAMs) .....	7
2.2.1. <i>Fabrication of self-assembled monolayers</i> .....	7
2.2.2. <i>General aspects of thiols</i> .....	8
2.2.3. <i>Self-assembly of thiols on metals</i> .....	9
2.2.4. <i>Mixed SAMs</i> .....	12
2.3. DYE SENSITIZED SOLAR CELLS (DSSCs) .....	13
2.3.1. <i>DSSCs functions</i> .....	13
2.3.2. <i>DSSC components</i> .....	14
2.3.3. <i>Mechanism of dye adsorption on TiO<sub>2</sub></i> .....	15
<b>3. EXPERIMENTAL .....</b>	<b>16</b>
3.1. SYNCHROTRON RADIATION .....	16
3.1.1. <i>Photoelectron Spectroscopy (PES)</i> .....	17
3.2. LOW ENERGY ELECTRON DIFFRACTION (LEED) .....	21
3.3. CONTACT ANGLE .....	22
3.4. QUARTZ CRYSTAL MICROBALANCE (QCM-D) .....	23
3.5. ATOMIC FORCE MICROSCOPY (AFM) .....	24
3.5.1. <i>AFM imaging</i> .....	25
3.5.2. <i>Peak force QNM</i> .....	26
3.6. SCANNING TUNNELING MICROSCOPY (STM) .....	27
3.7. MATERIALS .....	28
<b>4. RESULTS AND DISCUSSION .....</b>	<b>29</b>
4.1. SELF-ASSEMBLED MONOLAYERS .....	29
4.1.1. <i>Deposition from solution, mixture of thiols and effect of pH</i> .....	29

4.1.2. Deposition by sublimation .....	38
4.1.3. Evaluation of dye adsorption on $\text{TiO}_2$ : Adsorption from solution vs sublimation.....	44
4.2. $\text{Cu}_2\text{O}$ .....	47
4.2.1. The surface structure of $\text{Cu}_2\text{O}(100)$ .....	47
4.2.2. Dehydrogenation of methanol on $\text{Cu}_2\text{O}(100)$ and (111).....	53
<b>5. CONCLUSIONS.....</b>	<b>63</b>
<b>6. ACKNOWLEDGEMENTS .....</b>	<b>65</b>



## 1. Introduction

In recent decades, there have been many challenges and much motivation to discover and control the properties of surfaces. The initial step to achieve this aim is a detailed investigation of chemical and physical properties of interfaces between two different phases, such as the solid-gas, liquid-gas, solid-liquid, and even the solid-vacuum interface.

Research in this area is widely applied in technological products and industries including catalysis, electrochemistry, corrosion, wetting, lubrication, microelectronics, etc. Various scientific fields such as chemistry, physics, biology, and material science are strongly overlapping each other in order to modify the suitable surface for different applications. Thus, surface science involves with physical and chemical analysis techniques.

The initial motivation behind this thesis work is to achieve a fundamental understanding of the surfaces and the interfaces under atmospheric conditions (such as solid/air or solid/liquid interfaces) as well as benefit from methods which probe the topmost surface in a vacuum. The specific objective was to investigate molecular interaction of thin films on metal and metal oxide surfaces.

The first organic film on a solid surface was investigated by Irving Langmuir and Katharine Blodgett. The film was formed through a mechanical series of steps in order to achieve a monolayer or multilayer. A single homogenous monolayer or multilayer with accurate thickness was made by dipping the solid surface (glass) once or periodic times into liquid (water containing barium salts) covered by surfactant (stearic acid)[1, 2]. In contrast, the preparation of self-assembled monolayers (SAMs) is based on the spontaneous adsorption of, for example, thiols or surfactants onto the substrate. An important parameter affecting the film properties is the affinity of the head group of the adsorbate towards the substrate. Films are deposited onto the surfaces by immersion of the surface in the solution or through sublimation in vacuum [3, 4].

This thesis is divided into two parts. The first part of the study focuses on the adsorption mechanism for a self-assembled monolayer (SAM) on a gold surface. The surface chemistry, composition, and conformation of the SAMs by a selenol, dye, thiol or mixture of thiols were investigated. We prepared the self-assembled monolayers in two different ways:

- a) Immersion of the surface in a dilute ethanol solution.
- b) Sublimation (vapor deposition) in ultra-high vacuum (UHV).

Thiols with different polar terminal groups and their mixtures are deposited from 1 mM ethanol solutions. The response of the modified surfaces to stimuli such as pH was evaluated for thiols and their mixture.

Surface configurations, electronic states, and mechanisms of adsorption are investigated by sublimation of selenol and thiols on the Au(111) surface. Two types of dye deposition (from an ethanol solution and by sublimation) on TiO<sub>2</sub> are compared.

The second part of the thesis mainly focuses on the Cu<sub>2</sub>O(100) and (111) surfaces. Accurate knowledge about the structure and properties of Cu<sub>2</sub>O surfaces is of fundamental importance for improving our understanding of chemical reactions at these surfaces. Cu<sub>2</sub>O is extensively applied as a catalyst substance in chemical industries [5]. Copper-based catalysts are used for dehydration and oxidation of alcohols [6, 7]. To enable improvements of Cu<sub>2</sub>O catalysts, it is highly important to get an atomic level understanding of the alcohol interaction with Cu<sub>2</sub>O surfaces. Synchrotron radiation based photoelectron spectroscopy (PES) is a highly useful technique to study such surface chemical reactions. Moreover, ultra-high vacuum (UHV) conditions enable controlled studies of the adsorption/desorption mechanism on well-defined surfaces.

In continuation of a former colleague's investigation (Anneli Önsten) on the surface structures of Cu<sub>2</sub>O (111), we investigated the surface structures of Cu<sub>2</sub>O(100) by aid of several experimental methods based on UHV studies such as scanning tunneling microscopy (STM), PES, and low energy electron diffraction (LEED). Later, methanol adsorption/desorption was studied under UHV conditions on Cu<sub>2</sub>O(111) and (100) surfaces.

These studies contribute to the fundamental understanding of catalytic reactions and active sites on cuprous oxide surfaces. Furthermore, our results give insight into the mechanism of dehydrogenation of methanol on selective sites of copper oxide surfaces.

This work comes from collaboration with scientists in Surface and Corrosion and Applied Physical Chemistry at Department of Chemistry and Material Physics group at Department of Materials and Nano Physics. The overall aim of this work is to develop a relation between characterization and functional properties of molecular layers in atmospheric condition with the UHV study. In order to understand the mechanism of adsorption and properties of the surface, various techniques were employed.

Photoelectron spectroscopy (PES) was applied for evaluation of surface composition, packing density and coverage. In combination with PES, the scanning tunneling microscopy (STM) was applied in order to have atomic resolution images of surface structure. These UHV based measurements mainly were done at MAX LAB and by the Material Physics group.

The measurements and preparation in aqueous solution were mainly run by the surface chemistry and corrosion groups. The amount of adsorbed mass was measured by a quartz crystal microbalance (QCM). Contact angles are measured in order to measure the response of the modified surface to pH changes. The topography of the SAMs was determined using a Dimension Icon with ScanAsyst AFM powered by PeakForce Tapping.

## 2. Fundamentals and backgrounds

### 2.1. Metal and metal oxides surfaces

#### 2.1.1. Au(111)

The Au(111) surface has the lowest surface energy of the crystalline orientations in gold. Thus, deposited Au films propagate in the (111) direction [8, 9]. However, investigations of the other orientations of gold surfaces are also possible using single crystals in given orientations or by varying the morphology of Au films by changing the experimental methods for their fabrication[3].

The Au(111) surface with a herring bone reconstruction has a  $23 \times \sqrt{3}$  unit cell. This forms due to the presence of only 22 available sites for 23 surface atoms. Thus, the herring bone reconstruction is caused by a uniaxial 4.3% contraction along the  $\langle 1\bar{1}0 \rangle$  directions relative to the bulk plane [10]. The transition between fcc (ABC) stacking to hcp (ABA) stacking can be identified at double ridges; the so-called soliton wall. Soliton walls result from atoms in bridge sites (vertical displacement within 0.2 Å) (see Figure 1). The regions which are separated by the soliton wall are not equal. The larger regions correspond to fcc stacking which is more energetically favorable and the narrower regions correspond to hcp stacking. A superstructure on the large terraces with a zigzag pattern is formed by periodic bending of the ridges (soliton wall) by  $\pm 120^\circ$  angle [11, 12].

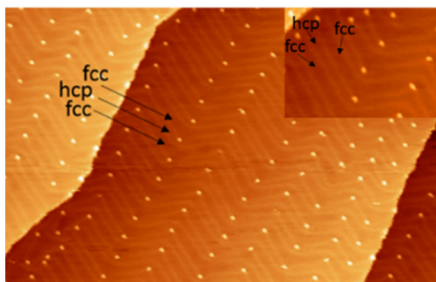


Figure 1: STM images of Au(111) surface 40x40nm<sup>2</sup> with large terraces separated by monoatomic steps (1.3Å) with visible herring bone structure. The fcc and hcp regions are shown by the arrows. Inset shows a zoom-in on these regions. [Paper I]

### 2.1.2. $\text{TiO}_2$

Titania have three different crystallographic forms: rutile, anatase, and brookite. It is possible to transform the anatase phase into the rutile phase by controlling impurities at high temperatures. The most thermodynamically stable phase is rutile and it is the most adopted phase in many applications such as photocatalysis [13, 14], gas sensors [15] and dye sensitised solar cells [16]. In the bulk structure of the rutile phase (Figure 2), Ti atoms are coordinated to 6 oxygen atoms (octahedral) and oxygen atoms are coordinated to three Ti atoms (trigonal planar). The rutile band gap is 3.1 eV which is quite high and thus this phase could be considered to be an insulator.

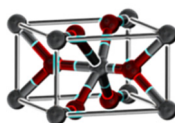


Figure 2: rutile unit cell in which Ti atoms (grey) are folded by 6 oxygens atoms (red) and oxygen atoms folded by three Ti atoms.

### 2.1.3. $\text{Cu}_2\text{O}$

Copper oxide ( $\text{Cu}_2\text{O}$  - cuprite) is a p-type conducting oxide with a band gap of 2.2 eV.  $\text{Cu}_2\text{O}$  has received considerable attention due to its versatile properties in different areas of research. For example,  $\text{Cu}_2\text{O}$  has the potential to be used as a solar cell material, a negative-electrode material in lithium batteries [17, 18], and as catalyst for synthesis of methanol [19].  $\text{Cu}_2\text{O}$  has been used as photocatalyst for splitting water molecules to produce  $\text{H}_2$  [20]. The unit cell of  $\text{Cu}_2\text{O}$  is shown in Figure 3. The crystal structure of  $\text{Cu}_2\text{O}$  contains two independent cristobalitelike interpenetrated lattices. This structure can be described as a bcc lattice with oxygen anions, where every anion is surrounded by a tetrahedron of copper ions[21]. The linear O-Cu-O bond is an unusual and interesting characteristic of this oxide. In this work, we study the (111) and (100) surfaces of  $\text{Cu}_2\text{O}$ . First in paper IV, we investigate the structure of the  $\text{Cu}_2\text{O}(100)$  surface in details and later in paper V, adsorption of methanol on both  $\text{Cu}_2\text{O}(111)$  and (100) is evaluated.

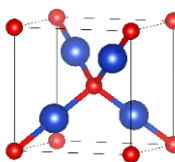


Figure 3: stick and ball model of the  $\text{Cu}_2\text{O}$  unit cell. The blue balls are copper (tetrahedron) and the red ones are oxygen (bcc)

### 2.1.3.1. $\text{Cu}_2\text{O}(111)$

The  $\text{Cu}_2\text{O}(111)$  surface with hexagonal symmetry (see Figure 4) and the most favorable termination gives a nonpolar surface with oxygen termination. Each copper plane (there are four cations ( $\text{Cu}^+$ ) per surface unit cell) is sandwiched between two oxygen planes (there is one anion  $\text{O}^{2-}$  per surface unit cell). Therefore, in each of the three repeated planes in the (111) direction (one copper plane between two oxygen planes), there is charge neutrality [22]. Copper ions in the bulk terminated surface are divided to two groups: the coordinately saturated ions  $\text{Cu}_{\text{CS}}$  (shown in Figure 4b in blue) which binds linearly with two oxygen atoms and the coordinated unsaturated ions  $\text{Cu}_{\text{CUS}}$  that bind with one oxygen in the plane below (shown in Figure 4 b in purple color). Similarly, oxygen has  $\text{O}_{\text{CS}}$  and  $\text{O}_{\text{CUS}}$ . Each  $\text{O}_{\text{CS}}$  binds with four copper atoms and  $\text{O}_{\text{CUS}}$  binds with three copper atoms [21]. The  $(1 \times 1)$  structure of  $\text{Cu}_2\text{O}(111)$  can be achieved by moderate ion bombardment and annealing in oxygen [21, 22]. By further annealing in UHV, the  $(\sqrt{3} \times \sqrt{3})R30^\circ$  reconstruction will appear. The reconstruction results from missing one-third of the outermost oxygen ions [21, 22].

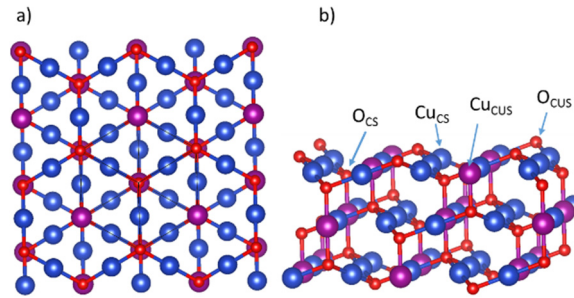


Figure 4: a) top view and b) side view of a stick and ball model of the  $\text{Cu}_2\text{O}(111)$  with three copper layers which are sandwiched with 6 oxygen layers: red (Oxygen), blue ( $\text{Cu}_{\text{CS}}$ ) and purple ( $\text{Cu}_{\text{CUS}}$ )

### 2.1.3.2. $\text{Cu}_2\text{O}(100)$

The  $\text{Cu}_2\text{O}(100)$  surface with square symmetry (see Figure 5) is a polar surface that could be both copper or oxygen terminated. The planes are alternatively copper and oxygen perpendicularly to the (100) direction. The planes that contain oxygen in parallel to the (100) surface have one oxygen ( $\text{O}^{2-}$ ) and the parallel copper planes in the (100) direction contain two copper ions ( $\text{Cu}^+$ ) [22]. Cox et.al described four different surface conditions for  $\text{Cu}_2\text{O}(100)$ . At 800 K, the surface structure is defined by the  $(3\sqrt{2} \times \sqrt{2})R45^\circ$ . By increasing the temperature to 1000 K, the surface changes to  $(3\sqrt{2} \times \sqrt{2})(\sqrt{2} \times \sqrt{2})R45^\circ$ . If the surface is kept at a similar temperature and goes through more than 30 ion bombardment cycles, the surface formed

is  $(3\sqrt{2} \times \sqrt{2})R45^\circ$ . The surface that is dosed with  $10^9$  L oxygen became a  $(1 \times 1)$  surface [22]. In Paper IV, we show that the structures described by Cox.et.al are not correct and  $\text{Cu}_2\text{O}(100)$  surfaces are  $(1 \times 1)$ ,  $(3,0;1,1)$  and  $c(2 \times 2)$  as the result of the different preparation methods [23]. The reason will be explain in details in Chapter 4.

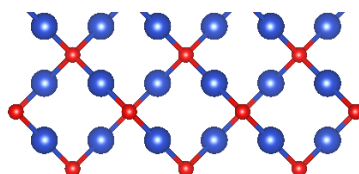


Figure 5: top view of a stick and ball model of  $\text{Cu}_2\text{O}(100)$ . Red (oxygen), blue (copper)

## 2.2. Self-assembled monolayers (SAMs)

### 2.2.1. Fabrication of self-assembled monolayers

The spontaneous adsorption of for example thiols, dithiols, and sulfides on substrates from solution or vapor phase results in molecular assemblies which are known as self-assembled monolayers (SAMs) [3]. This is very convenient and simple way to modify and manipulate the interfacial properties of surfaces. Surfaces on which SAMs are created can be planar such as thin films of metals, on glass or silicon slabs, metal foils, single crystals, or even semiconductors [24-26]. Other types of surfaces could be highly curved nanostructures such as colloids, nanoparticles, and nano rods [27, 28]. The choice of substrates and methods of preparation are directly dependent upon the type of adsorbate and what the application is for the SAM. Preferred surfaces for silanes or phosphonates are hydroxylated surfaces [29, 30]. Metal oxides surfaces are suited to material like fatty acid. The most commonly used substrate for alkanethiols is gold [31].

#### 2.2.1.1. Gold surface as standard

In spite of the fact that for many applications there are better alternatives than gold for the SAM substrate, gold is the most widely used substrate for thiolate SAMs. The reason for the popularity of gold as substrate is due to some of its properties. First of all, gold is easily obtainable as a thin film, single crystal, nano particles, and colloids. Moreover, gold is an inert metal which is not oxidized before its melting point. Gold does not react with  $\text{O}_2$  in the atmosphere, resulting in a simple preparation of the SAMs under atmospheric conditions [3]. Further, sulfur from thiols has high affinity for the gold surface which can easily replace contaminants if

they are present [32]. Finally, adsorbed thiols on gold are very stable for long periods of time, from days to weeks [33].

### 2.2.2. General aspects of thiols

The molecules which are used for preparation of SAMs typically contain three different parts.

The part of the molecule which binds to the substrate and guides the SAM process is known as a head group (linking group). Different head groups can bind with different kinds of metals and metal oxides surfaces. For example, S or Se groups from thiols or selenols form SAMs on gold [34] or phosphonic acid group from carboxyalkylphosphonic acids bind to metal oxides surface [35]. (Paper I, II, III)

The backbone or spacer connects the head groups to the terminal group. The intermolecular interactions between the backbones are van der Waals forces, the main driving force in forming well-defined assemblies of the adsorbed molecules [31]. By increasing of the length of the spacer, the structure gets more ordered [3, 4, 36].

The terminal group is the outermost part of the adsorbate molecule in the SAMs. By varying the selection of the organic terminal groups in the SAM (Paper I), it is possible to modify the surface properties, structure, and composition, via external stimuli such as pH, temperature, photo-illumination, and electrical potential [37, 38]. For example, the terminal group can be used for anchoring different molecules and biomolecules via a weak or covalent bond [32]. The wettability of the surface can be manipulated by choosing thiols with polar terminal groups like COOH, NH<sub>2</sub> (Paper I) and OH acting as a hydrophilic agent [3, 39, 40], or CH<sub>3</sub> and CF<sub>3</sub> as hydrophobic functional groups on the surface [41]. The schematic of the SAM is shown in Figure 6.

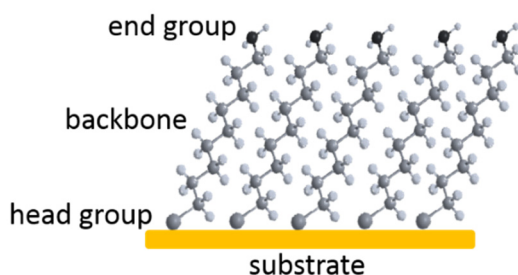


Figure 6: schematic of a self-assembled monolayer of an alkanethiol with NH<sub>2</sub> end group



### 2.2.3. Self-assembly of thiols on metals

There are two common methods to form self-assembled monolayers of thiols on metal surfaces. Gas deposition (sublimation) and immersion of the surface in a thiol solution having a specific concentration. The latter is more common due to its simplicity. The head groups (S, P, and Se) of the SAM molecules have strong affinity for noble and coinage metal surfaces [42-44]. Thus, the adsorption of thiols with similar head groups is kinetically fast and easy.

The first suggestion for the adsorption mechanism of SAMs was a Langmuir model, where the extent of adsorption is based on the number of available sites on the surface and the assumption that the adsorbed molecules do not interact with each other [4]. Later it was shown that the adsorption occurs in steps. First, thiols are physisorbed in the so-called gas phase. Molecules are mobile in the gas phase, which makes it difficult to capture this stage with scanning tunneling microscopy (STM). This initial stage occurs quickly after deposition and constitutes more than 80% of coverage [45-47]. The preparation of SAMs by sublimation allows detailed study in the early stage of SAM formation at low coverage. Several studies have been done in initial stage of SAM formation and STM images show an ordered assembly of alkane thiols lying down on the surface. This is known as the stripe phase [46, 48-52].

Thereafter, reorganization and straightening of thiols occur over several hours in order to reach equilibrium and saturation coverage in the next step. This step is mainly provoked by lateral interaction among the molecular moieties (intermolecular van der Waals forces). This van der Waals interaction has a very important role for ordering the thiols at high coverage after the head groups are pinned to the surface [45-47].

Particularly during gas deposition of thiols, by stepwise dosage it is possible to capture the transformation among the stripe phases at low coverage to a standing up phase at high coverage [48, 49]. Islands initially form between domain boundaries in the stripe structure. By increasing the dosage, the islands experience enhancement and grow bigger in a close packed configuration [49, 53]. A schematic of different phase in SAM formation is shown in Figure 7.

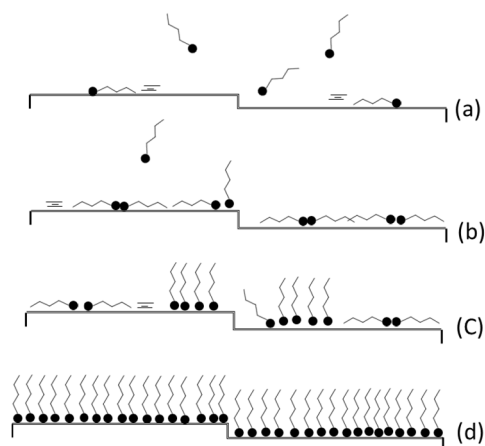


Figure 7: schematic of the steps in forming SAMs by alkanethiols on a metal surface. a) physisorption, b) lying down phase formation, c) island nucleation of the standing up phase, d) complete monolayer

### 2.2.3.1. Structure of adsorbed thiols on gold

The structure of adsorbed thiols on gold will change depending upon coverage, length of the alkane chain, and other properties of thiols. The  $(p \times \sqrt{3})$  structure where  $p$  is an integer or half integer, has been suggested for the early stage at low coverage on both constructed and reconstructed surfaces. The number  $p$  depends on the chain length of thiols lying down on the surface in different arrangements [49, 54, 55]. Recent studies have challenged the static adsorption of the thiols at a specific site on the unreconstructed Au(111) surface [56].

The new model is based on dynamic interaction between thiols and Au atoms which induce reconstruction of the Au(111) surface and the existence of Au adatoms [31]. (Paper II)

The complex of thiol-adatoms or dithiols-adatoms is the result of strong reconstruction of Au(111) surface atoms by the adsorption of thiols molecules [57-60]. Each adatom originates by lifting of the  $22 \times \sqrt{3}$  Au surface during reconstruction. This means that self-assembly is involve with Au adatoms thiols during SAM development [57].

After chemisorption of the sulfur group at a specific site on the substrate, thiols form an ordered lattice structure. The adsorbate lattice structure in the standing up phase is commensurate with full coverage of the Au(111) substrate. Hexagonal symmetry with  $(\sqrt{3} \times \sqrt{3})R30^\circ$  on the Au(111) surface has been frequently observed for alkanthiolate lattices. The molecule to molecule distance is 5 Å and the area per molecule is 21.4 Å<sup>2</sup> [31, 55, 61, 62]. However, the structure  $c(4 \times 2)$ , has been seen to

give full coverage too [63-65]. This  $c(4 \times 2)$  superlattice structure is four times larger than the  $(\sqrt{3} \times \sqrt{3})R30^\circ$  lattice and contains four molecules [31].

The adsorption site of thiols on Au substrates is still somewhat controversial in the field of self-assembled monolayers. Different sites were suggested: 3 fold hollow site (fcc or hcb) [66], bridge site [67] and intermediate site (between hollow and bridge site) [68]. For a while there was agreement on sites somewhere between the fcc hollow site and the bridge site [31]. However, this agreement did not last long. New experimental results showed that the top site and the hollow fcc adsorption site were competing for the  $(\sqrt{3} \times \sqrt{3})R30^\circ$  lattice [69]. The top site is not energetically favored as an adsorption site for alkane thiols based on DFT calculations. Since then, lots of experimental and theoretical research has been published regarding the strong reconstruction of the Au(111) surface upon thiol adsorption [59, 70-72]. The reconstruction on the Au(111) surface by adsorbed thiols causes Au vacancies or Au adatoms. The adatoms which constitute 1/3 of the gold surface are adsorbed at the fcc site on the gold surface while thiol chemisorbed on top of adatoms [73]. Grönbeck et al. used their DFT calculations [56] to propose a new configuration for  $c(4 \times 2)$  in which two thiols are adsorbed on top of Au adatoms (RS-Au-RS) in the cis configuration. The adsorption configuration of thiols via the adatoms is shown in the Figure 8.

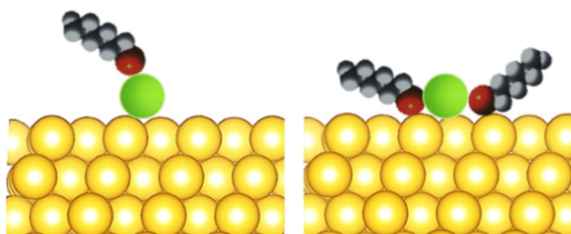


Figure 8: schematic of Au-adatom reconstruction models for adsorption of thiols on Au(111) surfaces. On the left, one thiol adsorbed on top of the Au-adatom which sits in a hollow site of surface Au atoms. On the right, two thiols bind to the Au-adatom. Color code is Au (yellow), Au-adatom (green), S,Se (red), C (grey) and H (light grey).

#### 2.2.3.2. Factors influencing the mechanism of SAM formation

Many factors could influence adsorption kinetics such as the concentration of the solution [74], the nature of the solvent [75, 76], the length of the alkane chain and the thiol's end group [27, 77]. The concentration is normally chosen to be 1 mM. However, a dilute solution could reach a similar coverage after a longer period of time. The average time to form well-ordered SAMs is reported to vary widely from two hours to several hours depending on the nature of the adsorbate molecules [31, 78]. Commonly used concentrations of the thiol solutions are in the range of 0.1 to 1 mM [79, 80].

The solvent is another influential factor for the kinetics of SAM formation. Interactions of the solvent with the substrate could cause a delay in the mechanism of thiol adsorption [3]. However, the effect of solvent on SAM formation remains controversial due to its complexity. The complexity comes from factors such as steric constraints, polarity, viscosity, mobility, and solubility of adsorbate [4]. Ethanol is widely used as the solvent. Properties such as high purity, non-toxicity and availability make ethanol a popular solvent in this field.

The purity of the solvent, adsorbate molecules, and cleanliness of the substrate are important factors to be considered in the formation of SAMs. It will take longer time to form ordered self-assembled monolayers in the presence of contaminants on the surface due to the time to replace the contaminants with thiol molecules [45]. A perfect self-assembly of thiols is not possible in the presence of surface defects which can be an obstacle in the application of SAMs.

The variation of chain length and its effect on the modification of the surface has been studied in different applications [27, 77, 81]. This factor also has very strong impact on adsorption kinetics. The initial quick adsorption step happening before the saturation step becomes longer with increasing chain length [47, 75]. The reason is possibly the lower mobility of longer chain molecules. In Paper I, the shorter chain adsorb faster than the longer chain thiols in the initial step. This will be explained more in chapter 4.

#### **2.2.4. Mixed SAMs**

Mixed SAMs are well-defined molecular structures in the monolayer on the surface made by different thiols with different termination groups. It is possible to customize surface properties through the mixture of thiols with different terminal groups. Therefore, thiol mixtures are utilized in a wide range of applications.

These mixed SAMs are formed from bulk solutions containing a mixture of all the participant thiols in the SAMs (RSH-R'SH). However, the mole fraction of each thiol in the mixed SAMs is not necessarily the same as the mole fraction in the bulk solution [3]. Lots of factors could affect the mole fraction of the participated thiols on the SAMs from bulk solution. One of the well-known factors for modification of mole fraction of compounds in the mixed SAMs is the choice of solvent for the thiol mixture [45, 82, 83]. The length of the carbon chain in thiols is another influential factor determining the fraction of thiols in the SAM [24]. The interaction between terminal groups also has an important role in the configuration of mixed SAMs [84, 85]. The effect of mixing thiols with different lengths and terminal groups is evaluated in Paper I.

## 2.3. Dye Sensitized Solar Cells (DSSCs)

Solar cells are attracting attention as a renewable energy source in the urgent fight to replace fossil fuels with renewable energy in order to reduce greenhouse gas emissions. Sunlight is converted into electricity by excitation of electrons with photons in solar cells. Dye-sensitized nanocrystalline solar cells consist of wide-bandgap nanostructured metal oxides with a chemisorbed dye for photon absorption. Titanium dioxide is the most commonly used wide-bandgap semiconductor that absorbs in the UV region of the spectrum. The structure and functionality of DSSCs are explained below.

### 2.3.1. DSSCs functions

Under illumination, excitation induces charge separation in dye. Donor electrons transfer out from HOMO (occupied orbitals) to the separated LUMOs (unoccupied orbitals). The photo-excited electrons are injected into the conduction band of  $\text{TiO}_2$  from LUMO and leave behind a hole in the HOMO. In this stage, dye molecules are oxidized and need to be regenerated by getting electrons from an iodide/triiodide redox couple. The process of photo excitation of electrons in DSSCs is schematically shown in Figure 9 [86, 87].

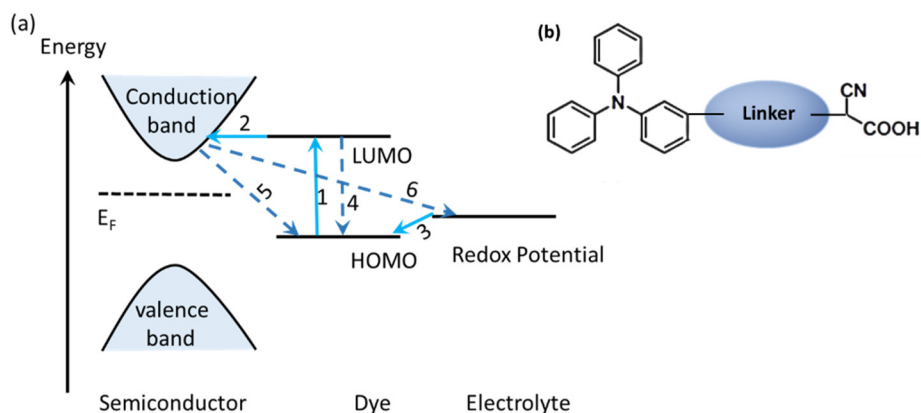


Figure 9: the energy level diagram of photoexcitation in DSSC process. Number 1 to 3 shows the excitation of electrons from HOMO to LUMO, thereafter injection to the conduction band and regeneration of HOMO by the electrolyte. Numbers 4 to 6 are not desirable recombinations of the electron - either (4) LUMO with HOMO or (5) conduction band with HOMO and (6) conduction band with iodine. b) Schematic of an organic chromophore dye: triphenylamine donor and cyanoacetic acid acceptor

### 2.3.2. DSSC components

Three main parts make the structure of dye sensitized solar cells. Solar cells contain two electrodes (working and counter electrodes) plus redox or conducting molecular system. (See Figure 10). The working electrode is a glass substrate coated with a thin layer of conducting material, mainly F:SnO<sub>2</sub>. On top of this conducting layer is placed a nanoporous semiconductor layer such as ZnO, SnO<sub>2</sub>, or (mainly) TiO<sub>2</sub> [88-90]. TiO<sub>2</sub> adsorbs a small fraction of the light due to its wide band gap. By covering the TiO<sub>2</sub> surface with dye (photoactive molecules), the small fraction of light absorption by TiO<sub>2</sub> will be compensated by the high surface area of the nanostructure of the semiconductor. A higher amount of dye adsorption is thus ensured. Organic dyes include a triphenylamin donor and a cyanoacetic acid acceptor (Figure 9) which are connected by various conjugated linkers for tuning the energy level of HOMO and LUMO [91]. The packing mode of the dye could be influenced by varying the dye's linker groups and expanding their  $\pi$ -conjugations [92] as well as changing the donor or acceptor parts of the dye molecules [93, 94]. The counter electrode is glass with conducting material (mainly F:SnO<sub>2</sub>) faced towards the working electrodes. The redox mediator (electrolyte) is typically liquid based containing the (I<sup>-</sup>/I<sup>-3</sup>) redox couple in the acetonitrile solution [95]. Redox mediators inject electrons to oxidized dye molecules in order to prepare them for new photo excitation and avoid electron recombination of the photo excited dye molecule with the semiconductor.

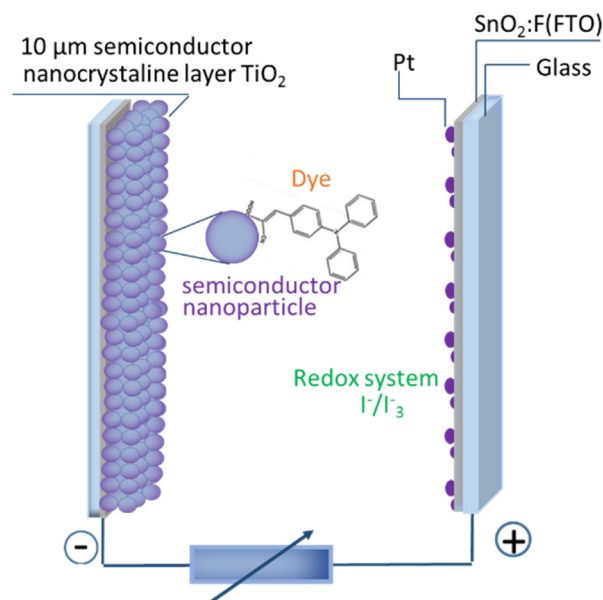


Figure 10: schematic picture of DSSC with electrolyte

### 2.3.3. Mechanism of dye adsorption on $\text{TiO}_2$

The interface between the self-assembled dye monolayer and the surface, and dye with the electrolyte solution are two important factors to consider when designing dyes and surfaces in DSSCs. According to Grätzel et. al, self-assembled monolayers of the dye on the  $\text{TiO}_2$  surface have a critical influence on the efficiency of the DSSCs for several reasons [96]. First, by having the amount of adsorbed dye and the extinction coefficient of the dye, it is possible to calculate the fraction of sunlight which can be harvested by the DSSCs. Second, having just and not exceeding more than a monolayer on the surface could lead to an efficient current of photo excited electrons to the  $\text{TiO}_2$  and degeneration of the dye by redox. On the other hand, multilayer formation or aggregation of dyes on the  $\text{TiO}_2$  surface result in the dye molecules not being in direct contact with the surface, which reduces the efficiency of the DSSCs. Finally, the SAM of dye should be a perfect blocking layer to avoid the recombination of the electrons injected into the  $\text{TiO}_2$  with the oxidized redox couple in the electrolyte [96]. Many surface studies have been done in vacuum in the field of DSSCs in which dyes have been deposited onto the surface of  $\text{TiO}_2$  in the gas phase as well as research in situ in which dye is deposited onto  $\text{TiO}_2$  surfaces from a solution. In Paper III, two types of dye deposition (from an ethanol solution and by sublimation) are compared.

### 3. Experimental

#### 3.1. Synchrotron radiation

Interaction between photons and matter can reveal many material properties. Synchrotron radiation sources fulfill important criteria desired for the characterization of surfaces such as a high photon flux, tunable photon energy, well defined polarization, and high brilliance\* and brightness. Synchrotron radiation is used in different types of experimental instruments for various research aims such as understanding electronic structure by photo emission of electrons or by absorption spectroscopy, and crystallography by diffraction or scattering.

Synchrotron radiation is based on radially accelerated charged particles causing emission of photon. In the generation of synchrotron radiation, confined electrons in the storage ring are radially accelerated in a circular path and emit radiation in a very wide spectral range (IR to X-rays). The emitted radiation is collected at the experimental stations such as the photoemission spectroscopy section. The storage ring and beam line is kept in UHV since collision of the beam with residual gas would cause energy loss. The use of bending magnets is the simplest way to change the direction of the electrons ( $v \sim c$ ) on the storage ring and cause emission. However, other insertion devices such as a wiggler and undulator, are used in the electron path line in the new generation of synchrotron radiation facilities. A periodic array of magnets at the base of the insertion device is used to create a back and forth motion of the electron beam, and to generate a stronger photon flux than traditional bending magnets are able to. The light distribution which is emitted from the charged particles forms a narrow cone shape distribution in the electron trajectory motion. The spectra from bending magnets, wigglers and undulators differ (See Figure 11). The magnetic field in the wiggler is stronger than for the undulator. The stronger magnetic field leads to higher intensity and larger divergence in the spectrum. Wigglers are generally utilized for hard X-rays. Conversely, an undulator has a weaker magnetic field which causes a smaller divergence and a partially coherent spectrum[97]. In the undulator, in order to use the strong peak of light interference at the desired photon energy, the proper undulator gap between magnetic arrays is necessary.

All emitted light in the storage ring is led to the end station, which contains a monochromator and mirrors in order to use the light in different technical instruments. The experiment in this study was done at Max-lab in Lund.[paper II, III, IV and V]



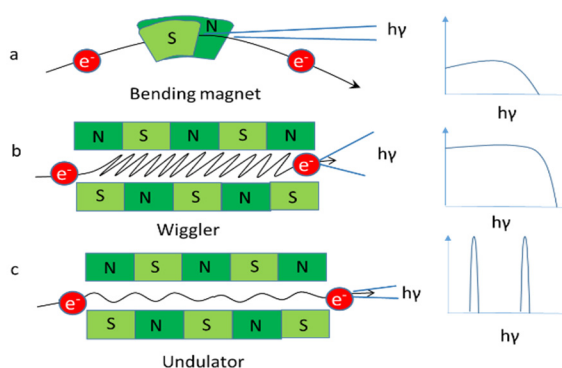


Figure 11: schematics of electron trajectories and their corresponding photon spectrum a) bending magnet b) wiggler c) undulator [97]

\*Brilliance is number of photons/ (time  $\times$  spot size  $\times$  convergence  $\times$  0.1% band width)

### 3.1.1. Photoelectron Spectroscopy (PES)

Photoelectron spectroscopy (PES) refers to the photo-electron interaction in a material and is a versatile technique to obtain information about the core level electrons (innermost in the atom), as well as valence band electrons (mixed with neighboring atom orbitals). Kai Siegbahn developed electron spectroscopy for chemical analysis (ESCA) in the 1950s which was named later x-ray photo electron spectroscopy (XPS). In this type of spectroscopy, the source of electron excitation is X-rays and they mainly probe the core level electrons. Another photoelectron spectroscopy technique is Ultraviolet photoelectron spectroscopy (UPS) which is used for valence band studies. Since synchrotron light sources are tunable through this energy range, there is no distinct border between UPS and XPS.

Photoelectron spectroscopy (PES) is utilized for surface characterization of materials. The principle of (PES) is based on the studies. Since the synchrotron light sources are tunable in the energy range, there is no distinct border between the UPS and XPS.

Photoelectron spectroscopy (PES) is utilized for surface characterization of materials. The principle of (PES) is based on the photoelectric effect, which was discovered by Hertz and theoretically described by Einstein. The kinetic energy of excited electrons depends on the frequency of the light, and is defined as a function of photon energy and binding energy of the emitted electron. Photons should have sufficient energy to be able to excite the electrons so as to break the material barrier (work function  $\phi$ ) and reach the vacuum level. Photoelectron excitation in terms of the energy conservation law is defined as:

$$E_{kin} = E_{photon} - E_{binding} - \phi \quad (3.1)$$

Figure 12 is an illustration of photo electron spectroscopy (PES) in terms of excitation of electron from core level (XPS) and excitation from valance band region (UPS).

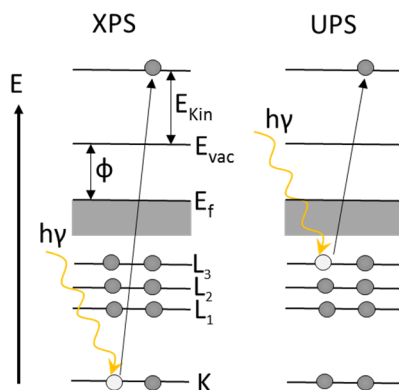


Figure 12: illustration of PES from core level (XPS) and from the valance band region (UPS)

The experimental setup of the PES is illustrated in Figure 13. The excited electrons are collected by the PES spectrometer. The spectrometer includes retarding lenses at the entrance in order to adjust the incoming photoelectron to defined pass energy. The concentric hemispherical analyzer (CHA) follows the electron trajectory, and includes a double layer electrode which is biased with a certain electrical potential to collect electrons with desirable kinetic energies. The electrons with kinetic energy lower or higher than the pass energy will be attracted to the inner positive or outer negative part of the hemisphere, respectively. (Figure 13). Finally, electrons with the desired kinetic energy travel to the micro channel plate (MCP) detector at the end of trajectory. Cascade amplifiers are used to enhance the signal. The intensity of the detected electrons is recorded in a final stage with a charge-coupled device (CCD) camera.

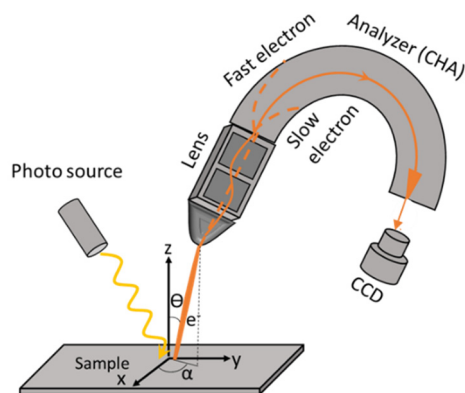


Figure 13: the experimental set up for PES

### 3.1.1.1. Cross section, surface sensitivity, depth distribution and emission angle

There is a wide range of energies available in synchrotron radiation. The photon – electron interaction cross section plays an important role for the choice of an appropriate photon energy for photo excitation in PES.

Since the X-rays penetrate into the material, they are able to excite electrons deep inside the material. Inelastic scattering of excited electrons is common - e.g. due to phonon excitation during the electron's trajectory out of the material. The electrons which contribute to the main peaks of PES are the elastic scattered ones which reach the analyzer. The inelastic scattered electrons may cause widening or effect on background of spectra. The mean free path of electrons is the average distance that electrons travel through the material without exchanging energy with the material and experiencing inelastic scattering. The mean free path depends on the material but more on the kinetic energy of the electron. There is a universal curve [98] for the mean free path of electrons as a function of their kinetic energy. The minimum of this curve which is located in the kinetic energy range 50 to 100 eV, is the most surface sensitive for PES experiments. (See Figure 14)

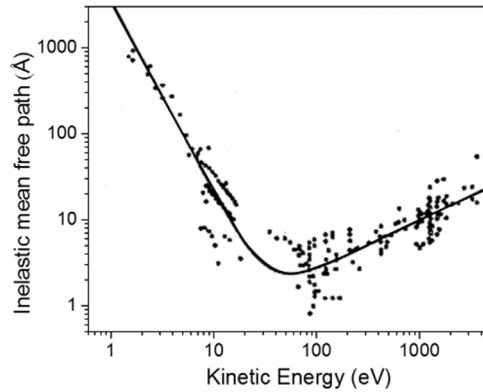


Figure 14: adopted from the Universal Curve of electron inelastic mean free path [99]

The traveling distance of the excited electrons in the material and the cross section of photon-electron interactions are influential factors for the intensity of peaks in PES.

$$I \propto I_0(\sigma) \cdot \exp\left(\frac{-d}{\lambda}\right) \quad 3.2$$

Where  $I_0$  is the emitted intensity from a (for example) ML. If it is a distance  $d$  from the surface, the signal will be attenuated by the factor of  $\exp(-\frac{d}{\lambda})$ . Thus,  $I$  is the intensity escaping the sample and  $\sigma$  is the cross section and  $\lambda$  is the mean free path. The intensity attenuates exponentially with increasing traveling distance of the excited electron to the vacuum (e.g. electrons which are located deeper inside the material). This property can be utilized for determination of film thicknesses by measuring the reduction in the intensity after film deposition. Thickness can be estimated by the intensity ratio after and before adsorption. It also could be used for making a depth distribution by changing photon energies.

The emission angle also influences the surface sensitivity. The distance travelled by the excited electrons inside the material increases by changing the direction of the detector from the normal to the grazing angle of emission. This results in a higher probability of inelastic scattering for the photoelectrons coming from deeper down in the material, and leads to a higher surface sensitivity due to detection of just photo excited electrons from the surface.

#### 3.1.1.2. XPS spectra and analysis:

Each core level electron for a specific material has a particular binding energy. Adsorption on the surface affects the chemical environment of atoms. In spite of the fact that core level electrons are localized, their binding energy will shift due to chemical adsorption on the surface of the material. The chemical shift is influenced by the charge density surrounding the emitting atoms. In other words, lower and higher surrounding charge density could shift the core level electrons to higher and lower binding energies, respectively. These shifts are utilized in surface chemistry and make PES a useful technique for characterization of chemical reactions occurring on the surface.

A proper calibration of the energy is very important in XPS measurements when chemical shifts are analyzed. In metal samples, the photoelectron energies are referenced to the Fermi energy of the sample. However, calibration for the semiconductor or insulator is not as simple as for conductive samples due to the low density of states at the Fermi level. Conductive surfaces are immediately neutralized after photoelectron excitation by the electron flux. However, insulator surfaces are only partially neutralized and a significant positive charge remains on the surface. Due to the surface charge, the Fermi level of the sample and spectrometer are not overlapping anymore. This charge on the surface is able to shift, split or broaden the peaks, which complicates the analysis of the data. There are several methods for charge elimination, e.g. blending the sample with impurities that increase conductivity or using a metal clip (tantalum) which is in direct contact with the sample. Sometimes the contamination in the sample could be used as a calibration of

the shifted binding energy. In our study of  $\text{Cu}_2\text{O}$ , potassium impurity peaks from the sample were used as a reference for correcting peak shifts.

Several components could be present in a spectrum of the core levels. These components are separated as well as their contribution estimated quantitatively by curve fitting. The experimental data points are theoretically fitted by varying parameters in a Voigt (Gaussian-Lorentzian) function. The Gaussian broadening comes from the light source or detector, and the Lorentzian width is due to core-hole lifetime. Parameters like binding energy, spin orbit splitting, and branching ratio can be varied in the fitting process in order to get good agreement with theory.

### 3.2. Low Energy Electron Diffraction (LEED)

LEED is based on the elastic scattering of electrons from the target surface. This technique is used for characterizing the crystalline structure of a surface, surface reconstruction, and for determining surface geometry. The LEED diffraction pattern shows the reciprocal lattice of the surface such that every diffracted beam correlates with the reciprocal vector. The principle of LEED is according to the de-Broglie hypothesis regarding the wave-like behavior of electrons which was discovered by Clinton Davisson in 1927[100]. The wavelength of an electron as defined by de-Broglie is

$$\lambda = \frac{h}{\sqrt{2m_0Ve}} \quad 3.3$$

Where  $h$  is Planck's constant,  $m_0$  is the rest mass of electron,  $V$  is the acceleration voltage and  $e$  is the electron charge. The acceleration voltage used for LEED is in the range of 10-500 V which results in an electron wavelength in the range of 0.87 to 2.75 Å. This wavelength, which is on the scale of atomic distances in a crystal, results in electrons being diffracted by the surface atoms and the elastically backscattered electrons create diffraction patterns.

The experimental setup shown in Figure 15 includes the electron gun which accelerates electrons towards the surface in the surface-normal direction. The electrons impinge the surface and are diffracted back towards the three grid system. The sample and first grid are grounded and the second grid is adjusted to have a negative potential. So the impinging electrons travel in a field-free region while that inelastic scattered electrons are filtered by the second grid. The third grid is located between negatively charged second grid and positively charged fluorescent screen as a separator. The electrons which land on the fluorescent screen cause a glowing pattern indicative of the crystal structure. The intensity of each spot depends on the

electron intensity. The intensity of the diffraction pattern is utilized for determination of the exact position of the surface atoms by an I-V curve.

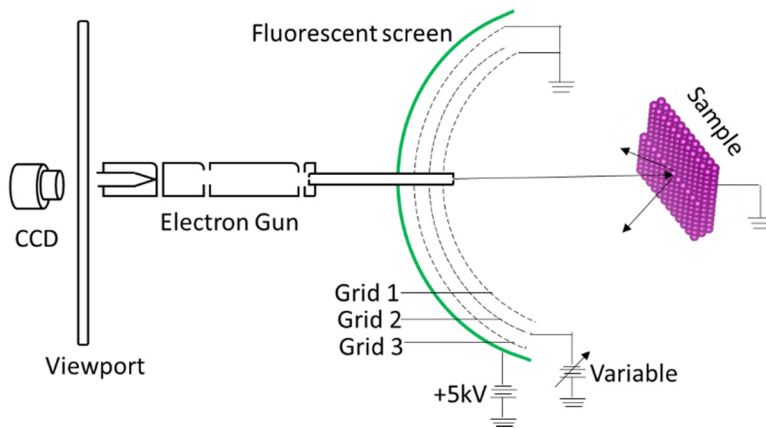


Figure 15: experimental setup for LEED

The diffracted pattern is mainly from the topmost layers due to the low-energy of the electrons in LEED. The energy of the electrons fit the minimum in the universal curve for mean free path of electrons in materials. So, the low energy electrons cannot penetrate the bulk without losing their energy. A sharp LEED pattern corresponds to a well-ordered surface. Defects in the crystalline structure could affect the shape and sharpness of the patterns.

### 3.3. Contact angle

This technique was used to determine the homogeneity and orientation of thiols in the SAMs. Generally speaking, this technique is very useful and convenient for surface characterization and for wettability studies. The contact angle is measured between the base line and the tangent line of a droplet. The energies of the three interfaces (air, liquid, and solid) at the meeting point influence the contact angle, which for a perfect surface is described by Young's equation (3.4) and is shown schematically in Figure 16:

$$\cos \theta = \frac{\gamma_{SG} - \gamma_{SL}}{\gamma_{LG}} \quad 3.4$$

Where  $\theta$  is the contact angle,  $\gamma_{SG}$  is the solid-gas interface energy,  $\gamma_{SL}$  is the solid-liquid interface energy and  $\gamma_{LG}$  the gas-liquid interface energy

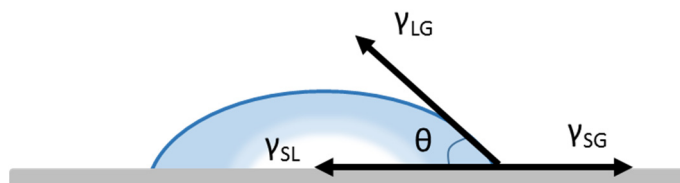


Figure 16: the interface between liquid, solid, and gas in a contact angle measurement.

The contact angle was measured using a DataPhysics OCA40micro instrument (DataPhysics GmbH, Germany) via the sessile drop method [101]. A liquid droplet is placed on the sample while it is illuminated. The changes in the shape of the sessile drop is captured by a high speed CCD camera (maximum 2200 images  $s^{-1}$ ) during deposition on the surface. Image analysis is done by the DataPhysics SCA20 software. The contact angle in our measurements were done by dispensing 5  $\mu L$  sessile drops. The droplet size should be chosen in a way to avoid shape deformation due to gravity [paper I].

### 3.4. Quartz Crystal Microbalance (QCM-D)

The Quartz Crystal Microbalance is an extremely sensitive balance which is able to detect mass variations on a nanogram scale with millisecond resolution. The measurement is based on the detection of the variation in the resonance frequency of a thin circular piezoelectric quartz crystal due to mass changes. The quartz crystal is coated with a thin film of interest. The amount of material adsorbed on the surface, or material removed from the surface in the case of corrosion, is evaluated. Adsorbed mass induces negative changes in the frequency while a positive shift in the frequency results from removal of material from the surface. It should be noted that adsorbed material is coupled with the solvent and the measured mass, the so called “sensed mass” in QCM-D is higher than optical techniques for measuring of actual adsorbed mass[102]. An example is that water trapped between the adsorbate molecules also contributes to the sensed mass. The QCM-D technique can also provide information about the structural or viscoelastic properties of the layer in order to determine the rigidity or softness of the adsorbed film via a dissipation parameter. Dissipation energy is measured as the decay rate of the oscillation amplitude while the applied oscillating driving voltage is off. The dissipation can be calculated by equation 3.5

$$D = E_{dissipated}/2\pi E_s \quad 3.5$$

Where  $E_{dissipated}$  is the energy lost from the oscillating crystal and  $E_s$  is the stored energy during the oscillation. More detailed information about the QCM-D technique information from the dissipation factor can be found in Rodahl et al [103].

In these studies an E4 instrument from Q-Sense (Sweden) was used for measuring adsorbed thiols from different solutions containing either a single type of thiol or thiol mixtures. This technique helps us to understand the structure of monolayers of mixed thiols and compare them with the monolayer from each individual thiol. It also enables us to study the surface titration for each case in the study.

There are couple of models which are suggested to convert the detected frequency changes to adsorbed mass. The choice of method depends on the structure and mechanical properties of the created film on the surface and viscoelasticity and density of the solvent. In this work, the simple Sauerbrey model was utilized to obtain the mass from the frequency changes since thiol monolayers create a rigid film and the frequency shift is not due to bulk properties.

According to the Sauerbrey equation, the changes in the resonance frequency can be converted to mass by using equation (3.6) [104].

$$\Delta m = -C \frac{1}{n} \Delta f_n \quad C = 17.7 \left( \frac{ng}{cm^2 s^{-1}} \right) \quad n = \text{overtone} \quad 3.6$$

Where  $\Delta m$  is the mass changes,  $\Delta f_n$  is the frequency change in the quartz crystal at the nth overtone and  $C$  is the mass sensitivity constant which depends on the physical properties of the crystal. In this work  $C$  equals 17.7 and  $n=7$  was used. The adsorbed mass calculated from (3.6) should be similar for normalized frequency changes for all overtones. This condition is fulfilled by the formation of a film with a high rigidity which normally has zero dissipation ( $\Delta D \sim 0$ ).

If the created film is not rigid enough (soft film  $\Delta D > 0$ ), the Sauerbrey equation is not a suitable model for calculating the adsorbed mass since the change in resonance frequency is not just due to the mass adsorption [105, 106]. Mechanical properties of the film like sheer modulus and viscoelasticity of the film will change the dissipation. Voinova described a model for the viscoelastic layer with high dissipation values [107], and Gordon and Kanazawa proposed a model for mass calculations from the frequency changes according to influence of solvent factors [108]. However, these types of models will not be presented here [paper I and III].

### 3.5. Atomic Force Microscopy (AFM)

Atomic force microscopy (AFM) is a tool which was initially utilized for surface topography and imaging. Later, the technique was found to be useful for surface force and friction studies by applying a suitable colloidal probe. The principle of AFM is



based on scanning over the sample with a sharp tip which is mounted on a cantilever. The piezoelectric crystal scanner is used to move sample and tip in the  $x$ ,  $y$  and  $z$  directions. The scanner is mounted either underneath the sample or in the head of the AFM to control tip-sample interactions. A laser is focused on the back side of the cantilever and reflects back to the 4 quadrant photodiodes. This enables recording the deflection of the cantilever by observing changes in the reflected position on the photodiode. The deflection of the cantilever gives information about the topography of the sample. A feedback system is needed to keep a constant amplitude set point or deflection for the tip. A schematic of an AFM is shown in Figure 17. There are several modes in AFM which are utilized for different of research aims. Here, some of the related modes to my work are presented [paper I and III].

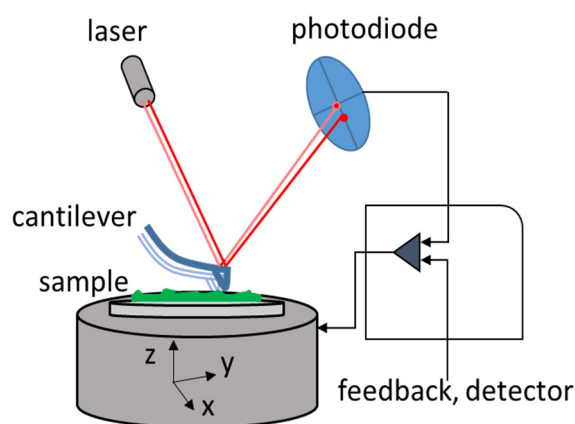


Figure 17: schematic of a basic AFM

### 3.5.1. AFM imaging

In these investigations the PeakForce QNM (Quantitative Nanomechanical Mapping) was used for imaging of the samples. However, there are two other types of imaging which are commonly used for topography studies in AFM. Contact mode (CM) in which the tip is in contact with the sample during the scan and the scanner moves up and down due to the feedback signal in order to keep a constant deflection value. Normally in CM, the cantilever has a low stiffness to deflect flexibly due to changes in the surface topography. Tapping modes (TM) is another mode for imaging, in which the cantilever is tapping near its resonance frequency and the tip lightly taps on the sample. A feedback system keeps a constant value for the oscillation amplitude during the scan. In this work, the contact mode was used for nano grafting of the thiolate surface in order to make a comparison between the depth profile of the nano shaved part in mixed thiols monolayer and unmixed thiols monolayer. After a part of the monolayer is shaved off in contact mode, the topography images were done in the QNM mode.

### 3.5.2. Peak force QNM

In the PeakForce tapping mode it is possible to control the tip-sample interaction accurately in order to decrease the lateral force during each line of the scan. The lateral force is a common issue in conventional contact mode imaging. In PeakForce QNM, the users are able to measure physical and mechanical properties of the surface during topography imaging [109]. The principle of this technique is to collect and analyze force curves which are produced in while the tip and sample are interacting. The tip is held by a cylindrical piezoelectric tube controlled in both the horizontal (X, Y) and the vertical (Z) direction. In each cycle of tip sample interaction, the feedback loop ensures a constant peak force determined by the maximum deflection of the calibrated cantilever. The position of the sample is controlled by a feedback system to have a cantilever deflection proportional to the initial set point value. It should be noted that the calibration of cantilever includes both optical lever sensitivity [110] and spring constant of lever [111]. By converting the information from piezo positioning and deflection of the cantilever to the force vs distance curve, quantitative mapping of surface material properties is possible. Each part of force curve gives information about the mechanical properties of the surface, as shown in Figure 18. The deformation depth on the surface due to the tip sample interaction is the distance between zero force along the approach curve to the peak force point. The adhesion between tip and sample is measured from zero force to the minimum force of retraction. The dissipated energy by the tip sample interaction can be measured as the area between the approach and retraction curves. By fitting the linear part of the retraction force curve with the Derjaguin-Muller-Toporov (DMT) model, the elastic modules of the sample can be calculated [112].

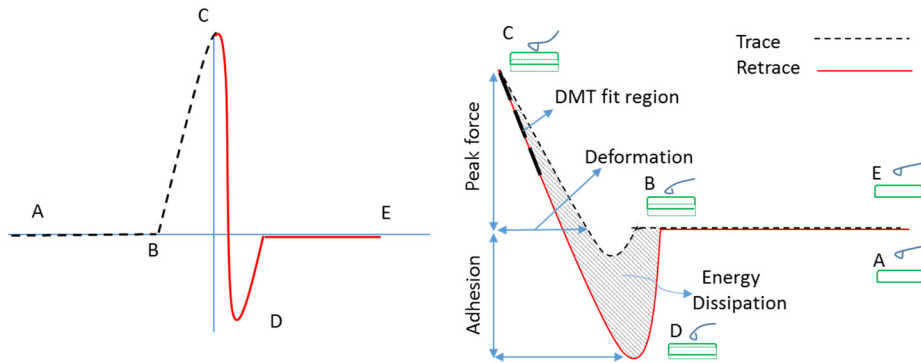


Figure 18: schematic illustration of force vs separation curve in each cycle of tip-sample interaction in peakforce QNM. The step for each cycle is labelled with a letter: A - tip is out of contact with the sample, B - the tip goes into contact with sample due to attractive forces, C - sample deformation due to the positive applied load, D- tip and sample are in contact due to the negative load from adhesion, E - the tip goes out of contact with the sample at the end of the cycle. Mechanical properties such as adhesion, deformation, and dissipation and DMT modules are calculated from the force-separation curves.

### 3.6. Scanning Tunneling Microscopy (STM)

Scanning tunneling microscopy (STM) is a microscopy technique based on quantum tunneling. This technique was developed by Binnig and Heinrich Rohrer at IBM in Zurich who were awarded by the Nobel Prize in 1986. An electron with energy  $E$  can tunnel through the potential barrier  $\phi$  between the conductive tip and the sample. The tip-sample separation should be in the order of a few Ångströms to make it possible for the electron wave functions of the tip and sample to overlap and allow tunneling through the barrier. The tunneling current has an exponential relation with the tip-sample separation ( $d$ ) (see equation 3.7). Thus, it is very sensitive to changes in  $d$ . The potential energy of this barrier should be larger than the energy of the electron which is tunneling across this barrier. The lateral resolution of STM is around 2Å and the vertical resolution is about 0.01Å.

$$I_T \propto e^{-2kd} \text{ where } k = \sqrt{2m(\phi - E)/\hbar^2} \quad (3-7)$$

Where  $d$  denotes the tip-sample separation and  $k$  is a constant depending on the height  $\phi$  of the potential barrier and  $m$  is the electron mass [113].

A voltage should be applied between the conductive tip and the sample. Due to the polarity of the applied voltage, the electrons are tunneling from (to) the tips to (from) the surface. Negative bias on the surface will lead the electrons from the surface to the tip. The electrons which move from an occupied state of the sample to the tip will reveal information about the occupied state of the sample (valence band states). Conversely, positive bias on the sample causes the electrons to tunnel from the tip to the unoccupied states of the sample and gives information about the conduction band states in the sample.

Figure 19 shows the experimental set up of the scanning tunneling microscopy (STM). The tip laterally scans the sample in the x-y direction. The vertical distance between the tip and sample is a very important factor for establishing the proper tunneling current and is controlled by a piezoelectric tube. A feedback system measures the tunneling current and keeps it constant by regulating the applied voltage. This mode of imaging is called constant current imaging. There is another mode of imaging for very flat surfaces, which is called constant height imaging. In this mode, the feedback loop is turned off in order to measure the changes in the tunneling current during scanning. Consequently, there is a high risk for tip crashing. To guarantee a suitable tunneling current, very good isolation of the system from internal and external vibration sources is needed. Pneumatic legs and damping systems inside the UHV system are commonly used for isolation [paper II and IV].

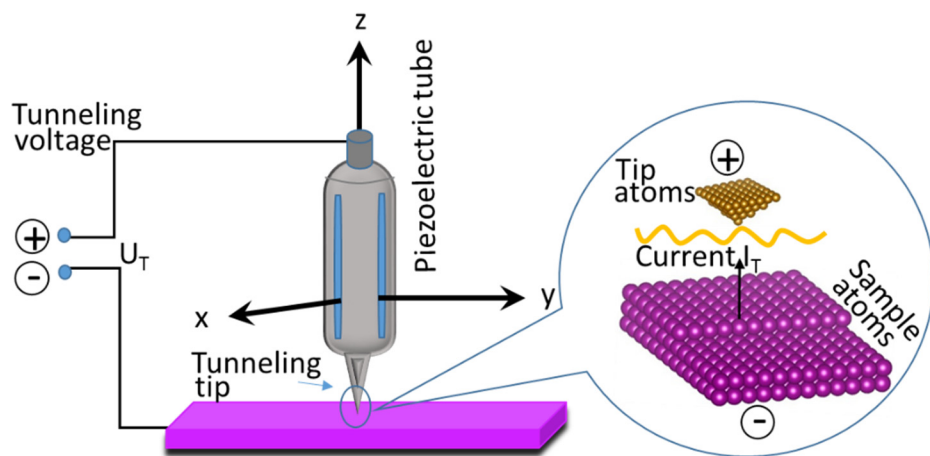


Figure 19: STM experimental set up

### 3.7. Materials

Table 1 summarizes the adsorbates on the different substrates used in this study:

Table 1: summarizes adsorbates and different substrates.

Adsorbate		Abbreviation	Substrate
Thiols	3-mercaptopropionic acid	MPA	QCM gold crystal & Au(111)
	11-amino-1-undecanethiol hydrochloride	AUT	
Selenol	Hexane selenol	-	Au(111)
Dye	Triphenylamin-cyanoacrylic acid	TPA-C	QCM TiO <sub>2</sub> crystal & TiO <sub>2</sub> (001)
	Phenoxazine	MP13	
Alcohol	Methanol	MeOH	Cu <sub>2</sub> O(111) ,(100)

## 4. Results and discussion

Self-assembled monolayers on gold surfaces will be discussed in this chapter. The surface properties of mixed monolayers of alkane thiols with different terminating polar groups and surface pH titration will be discussed under atmospheric conditions [paper I]. Then, the reaction of surface gold atoms in Au(111) and surface changes induced by low dosages of thiols will be discussed, followed by an investigation of the adsorption mechanism of selenol on Au(111) surfaces under UHV conditions [paper II]. Later, the self-assembly of dye molecules on TiO<sub>2</sub> substrates will be discussed under both atmospheric and ultra-high vacuum conditions [paper III]. In the last part of this chapter, Cu<sub>2</sub>O (100) surface structure will be evaluated in detail through experiments and theoretical calculations [paper IV]. Finally, the adsorption/desorption mechanisms for methanol on Cu<sub>2</sub>O single crystals in both the (100) and (111) directions will be discussed [paper V].

### 4.1. Self-assembled monolayers

#### 4.1.1. Deposition from solution, mixture of thiols and effect of pH

Engineering a surface responsive to external stimuli such as pH and humidity has been done by choosing oppositely charged polar terminal groups in the mixed self-assembled monolayer deposited from an ethalonic solution. The goal is to understand the nature of the SAM in the interface, such as the surface concentration of thiols from the mixture, the configuration of the thiols and their response to pH variation.

##### 4.1.1.1. Surface composition: results from QCM and XPS

The adsorbed mass from 1mM ethanol solution of pure (unmixed) AUT and MPA thiols and their mixture with different ratios was monitored by QCM-D. The adsorbed mass was calculated according to the Sauerbrey equation by measuring the shift of electro acoustic resonance frequency of gold QCM crystal upon loading thiols on the gold surfaces. Figure 20a shows the mass changes of pure AUT and MPA adsorbed on the Au-coated QCM crystal and figure 20b shows the mass changes from adsorption of AUT:MPA mixtures with different mixture ratios.

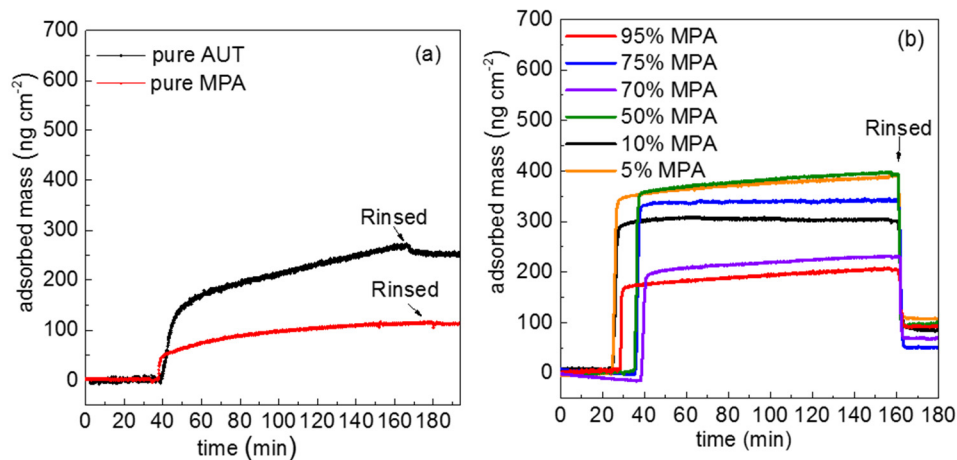


Figure 20: a) mass changes from pure (unmixed) thiols in ethanol solution (red line is MPA and black is AUT). B) Mass changes upon adsorption of mixed thiols

The adsorbed mass for the pure case and for different mixtures of thiols in solution are summarized in Table 1-4. It is necessary to mention that the mole fraction on the thiolate substrate is independent of the mole fraction of thiols in the bulk solution. The mole fraction of each thiol on the surface depends on factors such as type of solution, the alkane chain length, and it is not similar to the mole fraction of thiols in solution [3].

Table 1-4: Adsorbed mass (after rinse) from thiol solution (pure AUT, MPA and their different mixture ratios)

% of MPA in solution	Adsorbed mass (ng cm <sup>-2</sup> )	Rinsed mass loss (ng cm <sup>-2</sup> )
100	109±3	3±1
95	92±6	78±20
90	88±8	53±25
75	56±4	222±20
70	64±4	151±20
50	93±1	276±15
10	92±5	230±25
0	250±3	9±3

The adsorption mass curve for the pure thiols (Figure 20a) shows the trend which generally defines the formation of the SAM. The adsorption in the first step is very fast while rearrangement and ordering of adsorbed thiols second step takes longer [3, 80]. (The adsorption mechanism is explained in details in Chapter 2). The adsorption

mass curve of MPA reached a plateau after 2 hours (with  $109 \text{ ng cm}^{-2}$ ) and a small amount of adsorbed mass ( $3 \text{ ng cm}^{-2}$ ) was rinsed away from the surface. This result shows that MPA adsorption reached full coverage (i.e. a monolayer). By considering the ratio between adsorbed mass of MPA and its molecular weight, the surface concentration of MPA is calculated to be  $1.0 \times 10^{-9} \text{ mol cm}^{-2}$ . This agrees with the work of Sawaguchi et al [114]. The adsorbed mass curve of AUT is different from MPA and it did not reach a plateau before rinsing. Surface concentration of AUT is  $1.2 \times 10^{-9} \text{ mol cm}^{-2}$  which is more than MPA even though it is expected that MPA and AUT have comparable packing densities. Therefore, the higher amount of surface concentration in AUT indicates that the adsorption exceeds monolayer coverage. The amino terminal groups in AUT interact with each other via hydrogen bonds which leads to the creation of a second layer in the AUT SAM. This has been well studied with XPS measurements by other groups [115, 116].

Figure 20b also shows the adsorbed mass from different mixture solutions of AUT/MPA. The initial step of SAM formation from mixture solutions is faster than pure cases and the reorganization and ordering steps are not traceable. The missing second step in the SAM formation which belongs to reorientation of thiols reveals a significant change in the nature of adsorption. During this phase, there is a larger adsorbed mass for the mixture cases (except 95% and 70% MPA mixtures) in compare to the pure thiols just before rinsing. However, a significant amount of adsorbed mass is rinsed away. The adsorbed mass after rinsing for mixed cases are lower than the adsorbed mass in pure cases and there is no clear dependence between the removed mass and the bulk mixture concentration. Therefore, the easy removal of a significant amount of adsorbed mass in mixed cases is explained by considering them to be a physisorbed layer. If the adsorbed layer from mixture solution was just the mixed monolayer of two mentioned thiols, then the adsorbed mass should be a balance between the adsorbed masses for the pure cases. The chemisorbed mass in mixed SAMs are less than pure SAMs. The lowest adsorbed mass belongs to 70% MPA and 75% MPA.

A complementary experiment (XPS) was done to check the adsorbed amount of thiols in the SAM from mixed solutions and in pure cases. N1s which belongs to amino terminal group of AUT was not detected for the pure MPA, and C1s(O=C-O) from the carboxylic terminal group in MPA was not detected in AUT. Therefore, N1s and C1s(O=C-O) could be used to represent AUT and MPA in the signal for the respective samples. The XPS measurement is in agreement with QCM measurement. Figure 21a,b shows the normalized area under C1s (O=C-O) peaks and N1s peaks to the area under Au peaks for different mixture ratios of AUT/MPA and for the pure samples. The measured signal from N1s shows a weak increase when the percentage of MPA in mixture goes down, and in contrast, the C1s (O=C-O) signal decreases slowly by lowering the concentration of MPA in the mixture. However, these ascending N1s and

descending C1s (O= C -O) signals when lowering the MPA concentration in mixture is not very significant. The lowest signal is detected at 75% MPA for both N1s and C1s (O= C -O) (see Figure 21a and b) which is in agreement with the lowest adsorbed mass in 75% MPA recorded by QCM (Table 1-4). The ratio of C1s (O= C -O) signal to N1s in all mixtures is around 3:1.

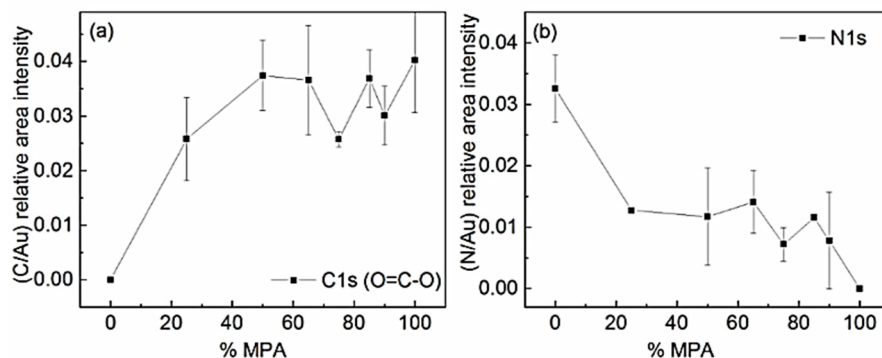


Figure 21: Areas under the a) C1s (O=C-O) peak and b) N1s ( $\text{-NH}_2/\text{NH}_3^+$ ) peak (normalized to gold) from XPS spectra for pure AUT and MPA and all their mixture SAMs.

According to both QCM and XPS results, there is a lower amount of adsorption in samples prepared from mixture solutions. The lowest adsorbed amount is recorded for the 75% MPA sample. Since we have full coverage in both pure cases, there is no evidence to encourage us to believe that some part of the surface in mixed samples are bare. However an explanation for the decreased adsorbed amount for the mixed samples is a significantly different conformation of the adsorbed molecules on the surface.

The molecules in the mixed samples are predominantly lying down parallel to the surface so the available sites for adsorption of more molecules are reduced. By considering the ideal condition for adsorption of thiols on the Au(111) surface and assuming that hollow sites are an adsorption site for the S head group of thiols on the Au(111) surface [4] having a standing up orientation, it is possible to calculate adsorbed mass for each of the AUT and MPA molecules. If the molecules stand in the hollow site, the calculated mass will be approximately 109 ng cm<sup>-2</sup> for MPA and 250 ng cm<sup>-2</sup> for AUT, which is similar to the experimentally measured adsorbed mass for pure MPA and AUT samples by QCM-D. Therefore, if we assume that the carbon chains lay down on top of Au atoms, calculated adsorbed mass will be roughly 70 ng cm<sup>-2</sup>. The calculated mass will be even less than 70 ng cm<sup>-2</sup>, if the alkane chain lies between the gold atoms since, more gold atoms will be occupied per molecule. The last calculated mass is close to the experimental result of QCM-D for mixed samples. Therefore, this calculation supports the idea of the laying down positioning of the thiols in the monolayer formed from mixture solutions.



There could be questioning that the huge amount of physisorbed mass prior to rinsing could block the surface from more chemisorption. The sequential adsorption from 75% MPA mixture solution followed by rinsing in each cycle of adsorption shows no changes in the adsorbed mass and the mass is similar after each cycle. Therefore, the physisorbed layer is not impeding the self-assembled monolayer. (See Figure 22)

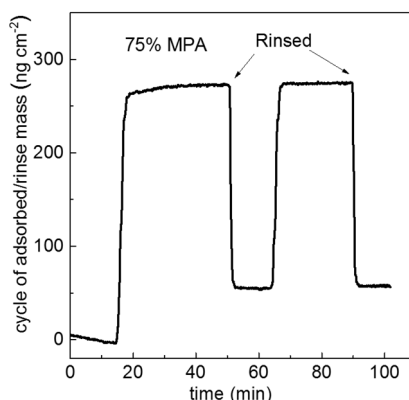


Figure 22: sequential adsorbed mass followed by rinsing for 75% MPA 25% AUT mixture.

The adsorbed molecules are arrested by the surface such that the interaction between alkane chains cannot straiten the thiols in the mixed samples. This is due to the formation of complexes in the mixed thiol solutions. The interaction between carboxylic and amino functional groups is well-known for a wide range of solvents via hydrogen bonding [117-124]. Formation of the complex among different carboxylic acids and amines have been reported for example in 1-octanol or in 2-ethyl-1hexanol [121, 125] and other solvents with different groups [122].

Complex formation (dimer, trimer etc) between short alkane chain MPA and long alkane chain AUT via the hydrogen bonds occurs in the bulk solution. The complex species consists of amine-carboxylic pairs which associated with the alkane chain protruded out with the sulfur head group in different directions. Therefore, each complex has more than one thiol with more than one possible anchoring sulfur head group. More than one anchoring group leads to the formation of the axial in-plane monolayer. In the bulk mixture solution there are possibilities for different stoichiometries for complex formation at the same time as having individual thiols in the bulk solution. (See Figure 23)

In 75% MPA mixture, assuming a 3:1 ratio of MPA: AUT in the complex leads to the participation of almost all available thiols in complex formation and, consequently, this leads to the lowest adsorbed mass and low signals for C1s and N1s in this mixture ratio.

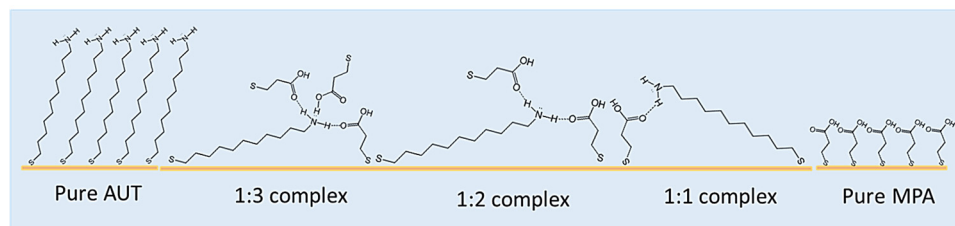


Figure 23: schematic of the pure AUT, mixtures with different possibility of stoichiometries for the complex formation and pure MPA.

#### 4.1.1.2. Physicochemical response of the SAMs

##### *contact angle measurements on the SAMs:*

Ionization of terminal groups of thiols in SAMs will change surface properties like wettability [39, 126]. Thus, contact angle measurements as function of pH are generally useful for investigation of the pH response of the SAMs. Contact angles for water on the MPA layer decrease from low pH ( $26 \pm 2^\circ$ ) to pH 8 ( $12 \pm 2^\circ$ ) but remain unchanged when the pH is increased to 9. This is due to ionization of the MPA terminal group. The terminal carboxylic acid groups in MPA are deprotonated (forming the negatively charged carboxylate ion) by increasing pH and consequently the surface becomes more hydrophilic. In contrast, the ionization of the AUT terminal group happens at low pH. Therefore, the lowest contact angle ( $21 \pm 2^\circ$ ) is recorded at pH 2 and it increases to a maximum ( $35 \pm 2^\circ$ ) at pH 9.

In contrast to unmixed SAMs, mixed SAMs are less sensitive to surface pH titration. However, the contact angles recorded for mixed SAMs are considerably higher (from  $36 \pm 2^\circ$  to  $47 \pm 2^\circ$ ) than for unmixed SAMs. As explained in previous section, the mixed SAMs have an axial in-plane orientation. Due to the orientation of mixed SAMs, hydrophobic alkane chains are exposed more to the interface between the SAMs and liquid. Thus, greater hydrophobicity is expecting in mixed SAMs. The lower sensitivity of the mixed SAMs to pH changes could be explained by either the complex between thiols occurring via hydrogen bonding where the participating groups are more resistant to be ionized [127, 128], or due to a fewer number of free thiols in mixed SAMs. Thus, it would be expected that the contact angle does not change as a function of pH.

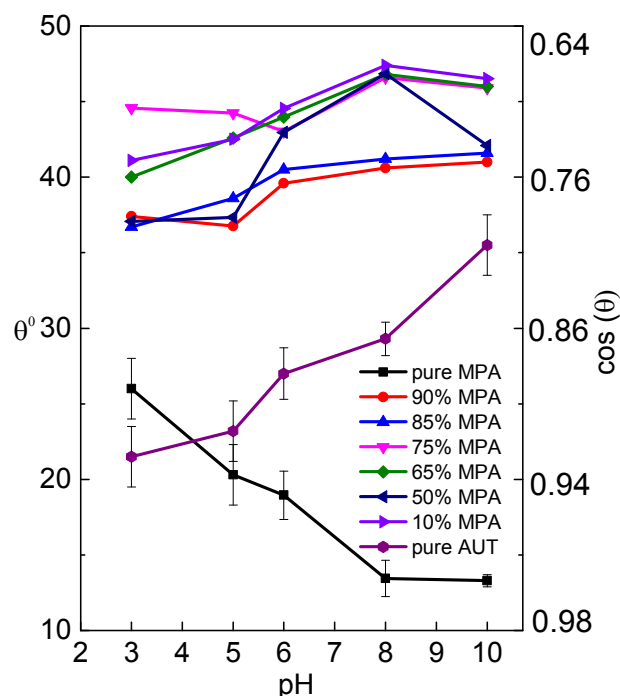


Figure 24: contact angle curves as a function of pH for pure AUT, MPA and their mixtures.

#### *Surface mass titration:*

Figure 25a shows the mass changes in the SAMs for pure MPA and mixtures of MPA/AUT with 95% MPA and 90% MPA. The mass is elevated by increasing the pH in all above mentioned monolayers. The elevation of the mass at higher pH is explained by two phenomena. First, the carboxylate group become negatively charged ( $\text{COO}^-$ ) at higher pH and consequently the polarization is increased. Therefore, more water molecules surround the charge moieties. Secondly, the negatively charged terminal groups interact coulombically with counterions of  $\text{Na}^+$  which are available in the electrolyte solution, and  $\text{Na}^+$  counterions are heavier than hydrogen ions [129]. By decreasing the pH, the mass loss observed is due to the protonation of terminal carboxylates groups of the SAMs. Thus, monolayers become neutral and the number of counterions and water molecules associated with the SAM decrease.

In contrast, for the SAMs of pure AUT and MPA/AUT mixtures with 10% MPA and 50% MPA, the mass decreases when pH is increased (see Figure 25b). These monolayers have a higher AUT percentage, so the terminal amino groups become protonated at low pH and the surfaces turn positively charged. The charged monolayer drives more association of water molecules towards the surface and coulombic interaction with counterion ( $\text{Cl}^-$ ) in the electrolyte.

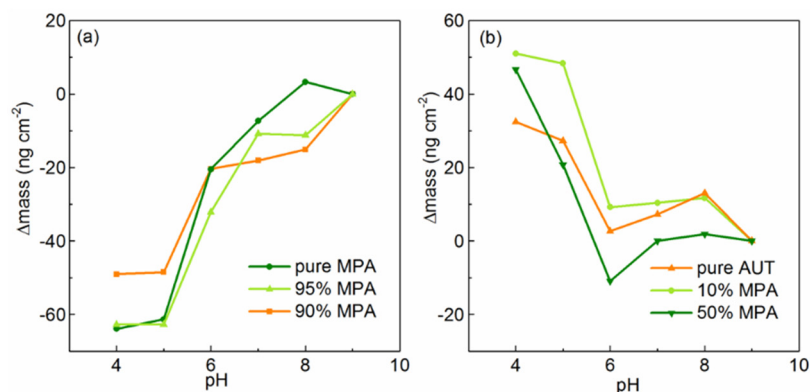


Figure 25: QCM-D measured mass changes of MPA/AUT SAMs as a function of pH changes (from 9 to 4). a) Pure MPA, MPA/AUT mixtures with 95% MPA, and 90% MPA; b) pure AUT, MPA/AUT mixtures with 10% MPA, and 50% MPA.

The mixed MPA/AUT with 75% MPA and 70% MPA shows almost no variation in the mass as function of pH except a small changes around pH 6 in the 70% MPA mixture. Complex formation in the mixed SAMs prevents ionization of polar group which could interact with each other via hydrogen bonding [127, 128]. Furthermore, this small amount of material may change the mass at a non-detectable level. (See Figure 26)

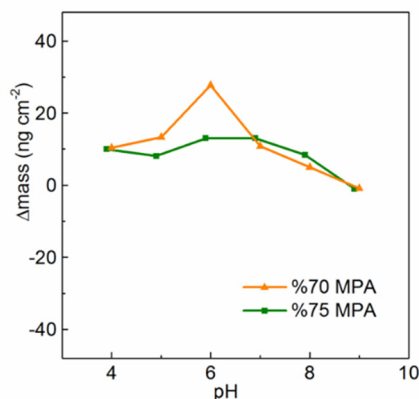


Figure 26: QCM-D measured mass changes of MPA/AUT mixtures SAMs with 75% MPA and 70% MPA as a function pH from 9 to 4.

#### 4.1.1.3. Imaging of the SAM

The SAMs on Au(111) surface were imaged by AFM in aqueous solution. The height images from bare Au(111), pure AUT and mixed MPA/AUT with 75% MPA are shown in Figure 27. A comparison of a bare surface with the surface modified by pure AUT shows the difference in morphology. A high density of circular features are observed in the pure AUT modified surface, which does not exist on the bare gold

surface and in very low number on the mixed 75% MPA adsorbed surface. These bright features are from the agglomeration of the AUT thiols caused by inter-plane hydrogen bonding between the terminal groups.

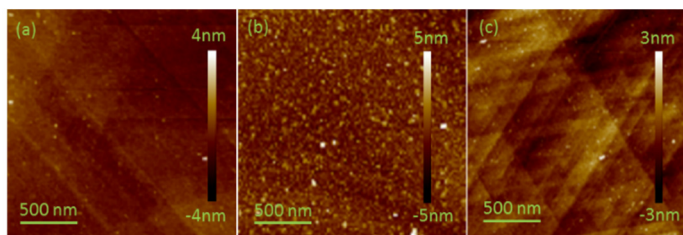


Figure 27: AFM height images of an Au (111) surface in Milli-Q water (a) bare surface, (b) AUT SAM, and (c) SAM of AUT/MPA mixture with 75% MPA. Scan size is  $2\ \mu\text{m} \times 2\ \mu\text{m}$  for all images.

The mechanical robustness of the SAMs were evaluated by AFM. Nano shaved AFM was performed by applying a higher loading force (around 15 nN) as used previously for shaving alkane thiols [130, 131] via the AFM tip which was swept 6 times over the particular area of the SAM in contact mode.

The height and adhesion images for the nano shaved area reveal the difference between pure AUT and 75% MPA /25% AUT mixture SAMs. In pure AUT SAMs, we had difficulty in shaving an area by tip due to tip involvement with the high density of agglomerates on the surface. In order to reduce the agglomeration, a pure AUT SAM was prepared according with a protocol suggested by Wang et al [115].

Figure 28 (a) to (f) shows the adhesion, height and depth profile images for the nano brushed pure AUT and 75% MPA/25% AUT mixed SAMs. Adhesion images for pure AUT show higher adhesion in the nano brushed area due to removal of the thiols from that area. The white walls in the height image could made by residual thiols that are not soluble in the water. The depth profile is around 1 nm in good agreement with the AUT length. This result suggests that pure AUT SAM has an upright orientation. (See Figure 28(a) to (c)).

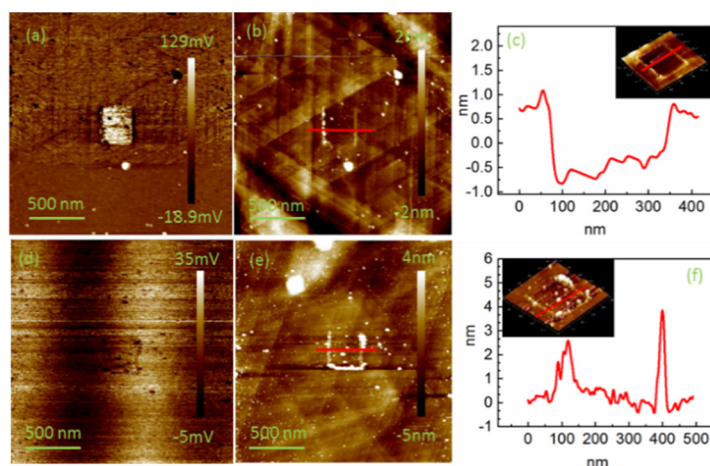


Figure 28: 2  $\mu\text{m}$  x 2  $\mu\text{m}$  scan size AFM images including a 300 nm x 300 nm nano-shaved area of pure AUT, and 75% MPA/25% AUT mixed SAM a)&d) adhesion b)&e) height c)&f). Adhesion images are qualitative only.

In contrast, there are no obvious changes in adhesion and height for the 75% MPA /25% AUT mixture in the nano brushed area. In the height image for mixed SAMs, there are white walls around the shaved part which may be created by tip-induced deposition. The depth profile also shows no obvious changes in height. No obvious changes in the nano brushed part of 75% MPA/25% AUT mixture SAM could mean that the axial in-plane orientation makes the surface more robust against of mechanical abrasion.

#### 4.1.2. Deposition by sublimation

##### 4.1.2.1. Gold reconstruction after thiol deposition

The structure of adsorbed thiols on the gold surface will be changed by increasing the dosage from low to high coverage. As explained in chapter 2, the  $(p \times \sqrt{3})$  structure (lying down on the surface in different arrangements) has been suggested for the early stage at low coverage for both constructed and unconstructed surfaces [49, 54, 55]. Recent studies provide a new dynamic model for thiol/gold interaction where the reconstruction is induced on the Au(111) surface by the existence of Au adatoms [31]. The thiol adsorption at low coverage causes a strong reconstruction of Au(111) surface atoms. The stimuli for this reconstruction are from thiol-adatoms or dithiol-adatoms formation during the initial dosage [57-60]. Each adatom originates through lifting of the  $22 \times \sqrt{3}$  Au surface reconstruction [57]. After chemisorption of S groups on specific sites on the substrate, they form an ordered lattice structure. The adsorbate lattice structure is in a standing up phase and is commensurate with full coverage of the Au(111) substrate.

Figure 29 shows low dosage of AUT thiols (10L) by sublimation deposition. The disturbance of the herringbone structure is clearly visible in the lower trace. There is no particular order in the style of reconstruction. The image shows the coexistence of intact and reconstructed herringbone in the lower terrace at low dosage.

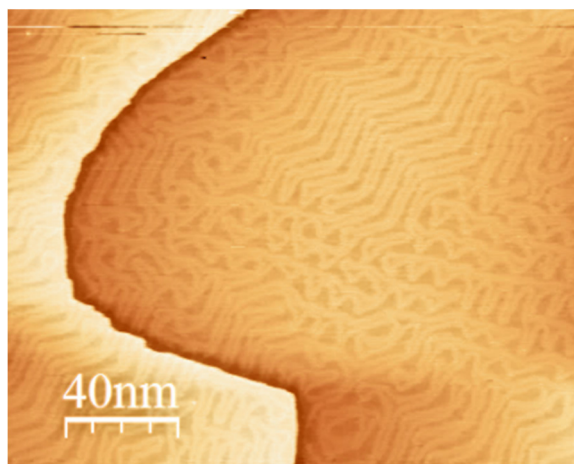


Figure 29: STM image of 10L sublimation of AUT on Au (111). 200x200 nm scan size with -1.49 V and current 14 pA

By adding a higher dosage of AUT (100L), the surface structure is changed drastically. The surface changes after each scan and the results show mobile Au atoms changing the structure of the surface. Shape of steps change and the big terraces of gold break into the smaller size islands. The island size decreases and leads to creation of voids between the islands on the surface. (See Figure 30)

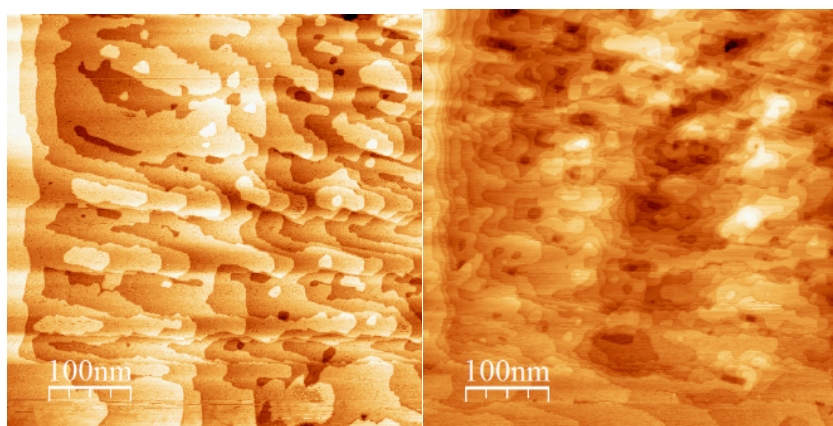


Figure 30: STM image of 100L sublimation of AUT a) immediately after deposition and b) 5 minutes after the first image. The scan size 500x500 nm with -1.46 V and current 65 pA.



At 300L dosage of AUT, the surface reached full coverage and Au atom movement stopped. The big terraces of gold covered by AUT with a striped pattern in different directions are formed. (See figure31)

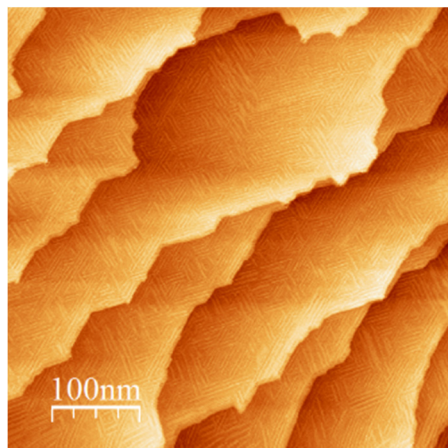


Figure 31: STM image of 300L sublimation of AUT a) scan size 500x500 nm with 0.35 V and current 26

#### 4.1.2.2. Se-C cleavage of hexane selenol at steps on Au(111)

Although, the thiolate SAMs are widely used for different characterizations, there is a chance for oxidation of sulfur groups or formation of disulfide during preparation of the SAMs [132]. Therefore, other chalcogenide elements like selenide are considered as alternatives to replace the sulfur groups in the SAMs. Furthermore, some of the chalcogenide anchors are more stable to external environmental factors like UV light, and temperature than sulfur groups [133-135].

However, the Se-C weak bond is considered a factor limiting selenol becoming as popular as thiols. The study shows that the Se-Au bond is stronger than an S-Au bond but that the Se-C bond is weaker than a S-C bond [136]. In this part, we investigate by PES and STM the stability of the Se-C bond.

Selenol was deposited on the Au(111) surface in gas phase and the experiment run in UHV to avoid any contamination of the surface. Contamination and impurities on the surface have been claimed as a source of Se-C cleavage [137, 138].

Figure 32 shows the core level spectra of Se3d, C1s and Au4f for the Au(111) surface at different dosages of selenol. In Se3d spectra (Figure 32a), only one component (Se1) at 53.42 eV appeared at very low dosage (10L). By considering no C1s signal at a similar dosage (Figure 32b), this Se3d (Se1) peak belongs to atomic Se from Se-C dissociation. By increasing the dosage from 50L to 130L, two new peaks are added to the Se3d spectra which are located at (Se2) 54.27 eV and (Se3) 55.22 eV. Therefore, at higher coverage, Se1 is representative of atomic Se, the second peak



(Se2) belongs to selenolate chemisorbed to Au(111) surfaces, and Se3 belongs to the second layer selenol [137].

C1s peaks (Figure 32b) appear at higher dosages (50L-130L). The strong C1s peak at 284.00 eV has broadened and shifted (+0.2 eV) at the 130L dosage in comparison to the C1s at 50L. The broadening and shift in the C1s peak at the higher coverage could be caused by core level energies being effected by their local environment. At higher dosage, the van der Waals interactions of the alkane chains cause the reorientation of the SAM from the lying to standing up position. This geometric change will cause core level shifts since the carbon is further from the Au surface. Secondly, the shifts and broadening could be caused by the second layer of selenol. However, both scenarios could contribute in broadening and shifts and it is not easy to extricate them. A very small second layer peak (Se3) makes it more tempting accept the former scenario which is a very well-known mechanism in selenol and thiol adsorption [80].

The Au4f clean surface (Figure 32c) has two peaks: the surface atom peak (S) at 83.67 eV and bulk peak (B) at 84.00 eV [139, 140]. The S peak is reduced and shifts from 0.33eV to 0.26 eV closer to B peak with adsorption of selenol. In spite of other studies [72], there are no other peaks having higher binding energy in Au 4f spectra in this work. A coverage of Au surface atoms (S peak) is 1.045 ML on the clean gold surface (1ML is for an unreconstructed (111) plane) [11]. Therefore, the comparison between the intensity fraction of the S peak in both clean and 130L dosed surfaces enable us to calculate the surface coverage of gold atoms (S peak) at the 130L dosage. The surface coverage (S) is reduced to 0.51 ML at the 130L dosage and the full width half maximum (FWHM) reduced from 0.42 eV for the clean surface to 0.36eV at 130L. At the same time, the bulk peak (B) is broadened from 0.28 eV to 0.36 eV from an unresolved surface contribution within B peak. The calculations from several research groups show that the most energetically stable surface structure for thiols and selenol on Au(111) surfaces involves complexation of Au- adatoms-dithiols or diselenol groups [57, 72, 73]. Au adatoms sits in the bridge site of the first Au-layer and S or Se groups bind on top of the Au adatoms [73]. The Au4f core level shifts (CLS) were calculated for the SAM made with methyl thiols according to the structure of the Au adatoms complex [56]. The negative CLS with respect to the bulk peak is assigned for surface gold atoms which either bind to Au adatoms or do not bind with sulfur. Au adatoms have positive CLS with respect to the bulk peak [56]. However, in this study, no positive CLS is observed due to lower electronegativity of Se compared to sulfur.

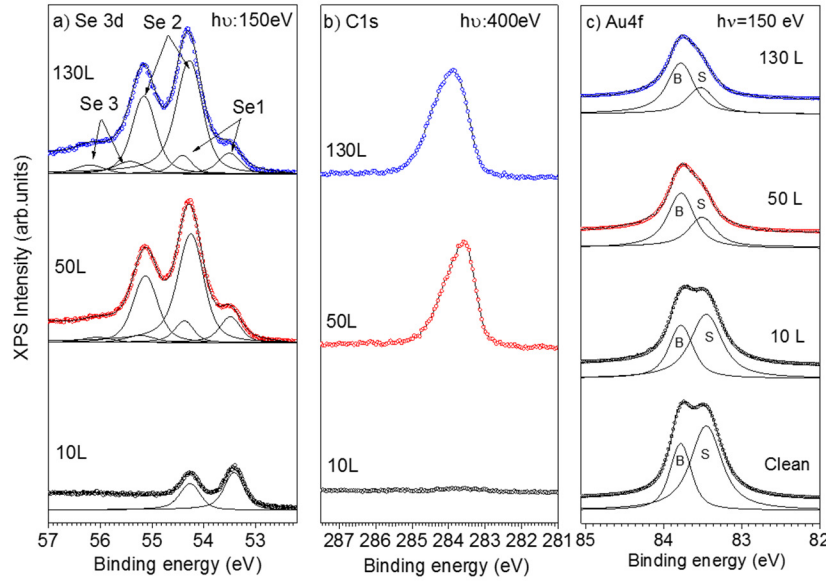


Figure 32: a) Se3d, b) C1s and c) Au4f spectra and their fitting curves recorded for the clean and hexane selenol exposed Au(111) surface. Selenol doses in Langmuir are given in the figure. All depositions and measurements were done at room temperature.

The coverage of Se is calculated from the intensity ratio of Se3d and Au4f. Some factors such as photon flux, the photoionization cross section, the electron mean free path and the surface concentration are used for determination of the intensity in a certain core level peaks. The mean free path is not considered when upper surface atoms are examined. The Au4f surface peak (S) and Se3d of atomic selenium (Se1) at the lowest coverage (10L) are used for calculating selenol coverage. Both peaks (S, Se1) have been measured by the same photon energy. Therefore, from the intensity ratio of Se3d to 10L (Se1) and surface Au4f (S) peaks we get:

$$\theta_{Se} = \frac{I_{Se}}{I_{Au}} \times \frac{\sigma_{Au}}{\sigma_{Se}} \times \theta_{Au} \quad (1 - 4)$$

where  $\theta$  is the surface coverage represented by a certain peak,  $I$  is the intensity of the peak and  $\sigma$  is the photoionization cross-section [141]. Au4f (S) in a clean sample represents the 1.045 ML of surface atoms in the herringbone reconstruction [11]. At the 10L dosage, the total intensity of Au4f is the same as for the clean surface. Se coverage at 10L dosage is calculated to be around 0.05ML by using the cross section of Se and Au, the corrected intensity of Au4f and Se3d, and the total coverage Au4f. The comparison between Se3d intensities for the 10L and 130L dosages makes it is possible to find the total coverage at the 130L dosage which is around 0.42 ML. Thus, Se3d components at 130L are 0.05ML for atomic Se, 0.33ML for selenolate and

0.04ML for hexane selenol in the second layer. However, intensities can be affected by photoelectron diffraction effects. Our calculation does however lead to a reasonable coverage since the expected saturation coverage of the selenolate surface with the Au adatom diselenolate structure is  $1/3$  ML [73] .

The STM image at low coverage (10L) shows the terrace edges decorated by an adsorbate while the herringbone structure is clearly visible and look intact. Scattered protrusions are also visible in the terraces. Considering the  $\text{Se}_{3d}$  peak at low dosage and these STM images suggests that Se-C dissociation occurs at the step edges (See Figure 33)

The calculated activation barrier for Se-C cleavage by DFT is 32.3 kcal/mol for  $\text{CH}_3\text{Se}$  and 23.5 kcal/mol for benzene selenol [142, 143]. These barrier activation energies are significantly higher for the Se-C dissociation. Therefore, the existence of catalysts such as oxidize species or contamination were suggested as the source of Se-C cleavage [143]. In this study, there were no oxygen or oxides species. From the STM images (Figure 33), it appears that the Se-C cleavage happens at the step edges. Atoms are more reactive at the steps than the terraces [144].

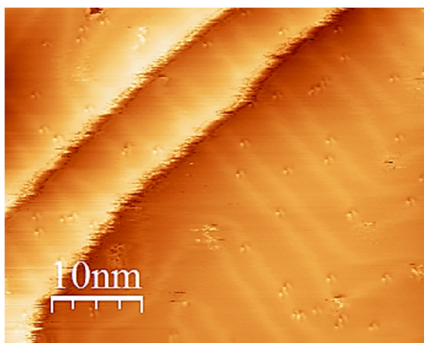


Figure 33: STM images from the Au(111) surface after 10 L hexane selenol dose ( $50 \times 50 \text{ nm}^2$ ) at +0.62 V sample bias and 98 pA tunnel current.

The STM images at higher coverage (50L and 130L) are shown in Figure 34. At the 50L dosage, there are a combination of different configurations of selenol on the surface. The stripe phase is visible in the right corner of Figure 34a. In the middle of the Figure 34a, the reconstructed herring bone is visible as a brighter points. The parts without any pattern are possibly fully covered by selenol. In the Figure 34b at 100L dosage, the herringbone structure is completely gone and the all terraces are covered. Near the edges of terraces, the upper edge is decorated by the protrusion line which could be the atomic Se. It is not possible to resolve more detail in the terraces which could be due to alkane chains being flexible and mobile at room temperature.

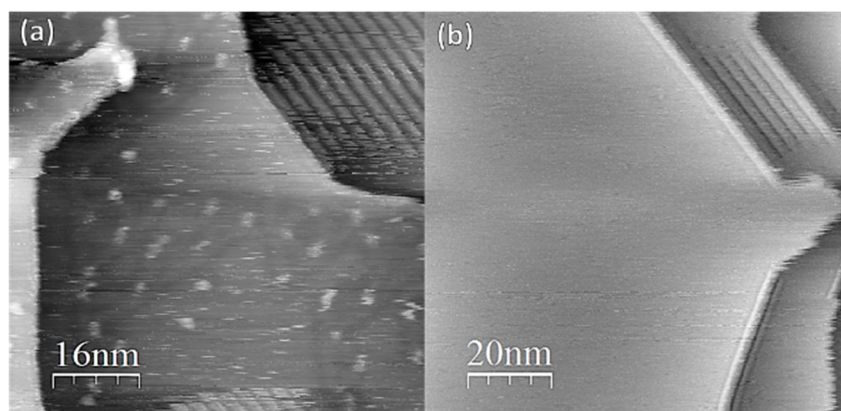


Figure 34: STM images from the Au(111) surface a) after 50 L hexane selenol dosage ( $80 \times 80 \text{ nm}^2$ ) at -1.93 V sample bias and 17 pA tunnel current b) after 100 L hexane selenol dosage ( $100 \times 100 \text{ nm}^2$ ) at -1.4 V sample bias and 14 pA tunnel current.

#### 4.1.3. Evaluation of dye adsorption on $\text{TiO}_2$ : Adsorption from solution vs sublimation

In DSSC, it is very important to have a maximum amount of dye adsorption which leads to maximizing photon absorption. On the other hand, aggregation of dye into large clusters or multilayer films leads to reduced efficiency [94, 145]. The amount of adsorbed dye just needed to create a monolayer on the surface would guarantee an efficient current from photo excitation into the  $\text{TiO}_2$  and thus, degeneration of dye by redox [96, 146, 147]. Conversely, multilayer or aggregation of dyes on the  $\text{TiO}_2$  leads to indirect contact between the physisorbed dye molecules with the surface which negatively effects the efficiency of the DSC [96, 148].

The objective of this study was to define the nature of the interface formed between the  $\text{TiO}_2$  and adsorbed dye in order to evaluate characteristics such as adsorbed amount, equilibrium constant and presence of aggregates or multilayers directly in solution. QCM and PES are applied for these characterization. In this work we compare thin layers of dye deposited from a dilute liquid solution with deposition through sublimation in UHV.

Figure 35a and b show the mass uptake by the  $\text{TiO}_2$  QCM-D sensor while the dye solutions (TPA-C, MP13 respectively) with concentrations from 0.1 mM to 1 mM are pumped through the system. After each injection of dye, pure ethanol is pumped into the system for 10 minutes to rinse off the physisorbed dye from the surface. Therefore, the mass after rinsing corresponds to the chemisorbed mass whereas, the mass before rinsing contains both physisorbed and chemisorbed mass. The chemisorbed masses for TPA-C and MP13 are shown in Figure 35c and d, respectively. There are separate curves for three different measurement cycles on the virgin  $\text{TiO}_2$  QCM crystal from the same batch. The black curve with square symbols

is the average of result from the three measurement cycles. The measured mass at each concentration is indicated by the symbols and solid lines are fitted curves according to the Langmuir equation which is shown in (2-4).

$$\theta = \theta_{max} \frac{Kc}{1 + Kc} \quad (2-4)$$

Where  $c$  is the concentration of dye solution,  $K$  is the equilibrium constant,  $\theta$  is the surface coverage at each concentration and  $\theta_{max}$  is the maximum coverage on each sample. Note that  $\theta_{max}$  changes for different sensors since the active surface area and the roughness change in each sensor, but the trends are comparable. The equilibrium constants for TPA-C and for MP13 are calculated from the fitted curves and they are  $0.8 \text{ mM}^{-1}$  and  $2.4 \text{ mM}^{-1}$  respectively. [149].

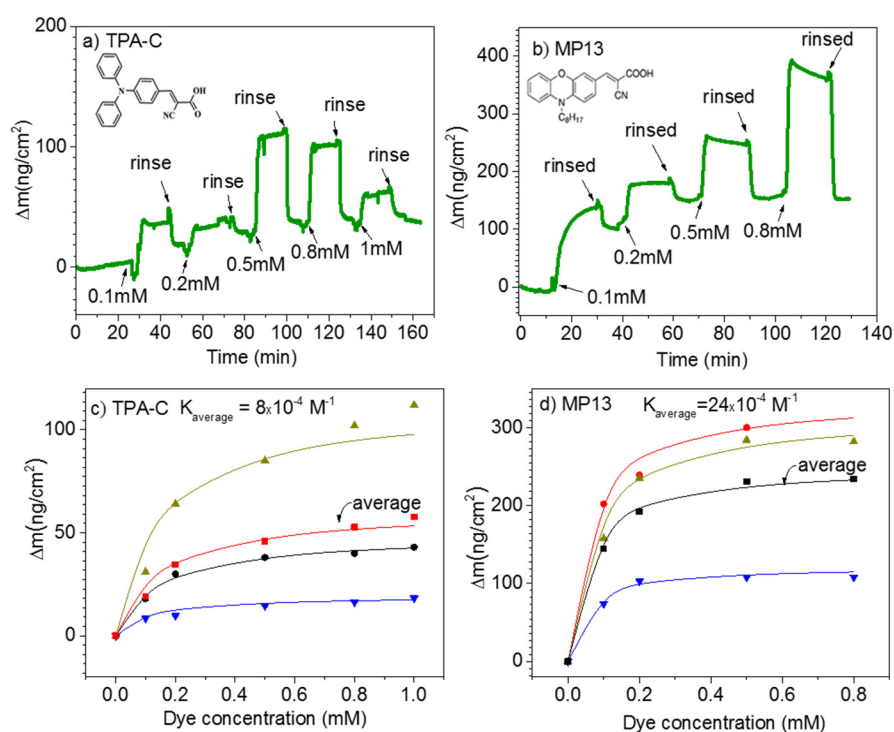


Figure 35: a, b) shows adsorbed mass of dye from a solution at different concentrations vs time a) TPA-C b) MP13. c), d) shows the chemisorbed mass vs concentration for TPA-C and MP13, respectively.

The molecular weight of MP13 dye is 1.14 times higher than TPA-C dye. By considering the variation in the adsorbed mass in each cycle (See Figure 35c and d), the ratio of adsorbed mass per unit area in MP13 is more than 3 times higher than TPA-C dye under similar conditions.

It is experimentally well proven that rinsing after adsorption causes more stability in the formation of the film. The rinsing step after each cycle of adsorption leads to the reorganization of dye molecules on the surface. Gusak et.al investigated the adsorption/desorption kinetics of the dye Z907 by indirect nanoplasmonic sensing. They found that the adsorbed film is more stable after intermittent rinsing steps. Their results showed the fraction of desorbed molecules to be lower after intermittent rinsing in compare to the case were dye was adsorbed continuously [149]. The physisorbed mass for MP13 increased while the dye concentration in the solution increased. In contrast, the physisorbed mass for TPA-C varies at each concentration and does not follow any order. IR studies of the phenyl-based dye shows that dye molecules are possibly dimerized through hydrogen bonding of the CN-group to the carboxylic group [150].

The dimer formation and lower chemisorption of TPA-C dye could be due to island-type adsorption growth on the surface while MP13 molecules look to have laminar growth.

The O1s and N1s from the TPA-C adsorbed on  $\text{TiO}_2$  are shown in Figure 36. Each panel contains spectra from the sublimation of dyes onto  $\text{TiO}_2(110)$  at different coverages plus spectra from the adsorbed layer on the  $\text{TiO}_2$  QCM crystal from the 0.5mM TPA-C dye solution.

TPA-C adsorbed on the  $\text{TiO}_2(110)$  surface is by the carboxylic anchoring group while the OH is deprotonated and TPA-C binds with two oxygens to the surface. Therefore, the O1s ( $\text{COO}^-$ ) component peak at +1.45 eV from the bulk O1s peak of  $\text{TiO}_2(110)$  is resolvable at all coverages [151]. Increasing the coverage above a monolayer leads to the appearance of a new component, (-OH) at 534 eV [151]. The carboxylic group in the second layer is not deprotonated (they are free and not anchoring to the surface). Therefore, two separate O1s components, (OH) and (-C=O), with a 1.66 eV separation at similar intensity are resolvable [151]. O1s in the dye film which adsorbed from solution is broader than the O1s in the sublimated samples. The numerical fit with four components (bulk oxygen, ( $\text{COO}^-$ ), (OH) and (-C=O)) shows that ( $\text{COO}^-$ ) is stronger than the same components in the sublimated samples. The broadening may be caused by OH groups from water in the film adsorbed during the transportation of the sample. The water cannot stay on the sample in the UHV condition but it could leave OH components on the surface which has the binding energy +1.6 eV from O1s bulk peak of  $\text{TiO}_2(110)$  [152] close to ( $\text{COO}^-$ ). O1s spectra from the sample prepared in solution shows a dominant layer of dye adsorbed on  $\text{TiO}_2$  which contains some water residues and a small percentage from dye molecules not bound to the surface.

N1s spectra contains two components: nitrogen atoms in CN and nitrogen atoms in  $(\text{C}_5\text{H}_6)_3\text{N}$ . The latter compound has higher relative intensity than CN which caused by the adsorption geometry of TPA-C dye. Dye molecules adsorb via

deprotonated carboxylic groups and triphenyl compounds protruding from the surface. N1s from the dye film adsorbed from solution has similar shape as for the sublimated sample but it is relatively difficult to determine the coverage.

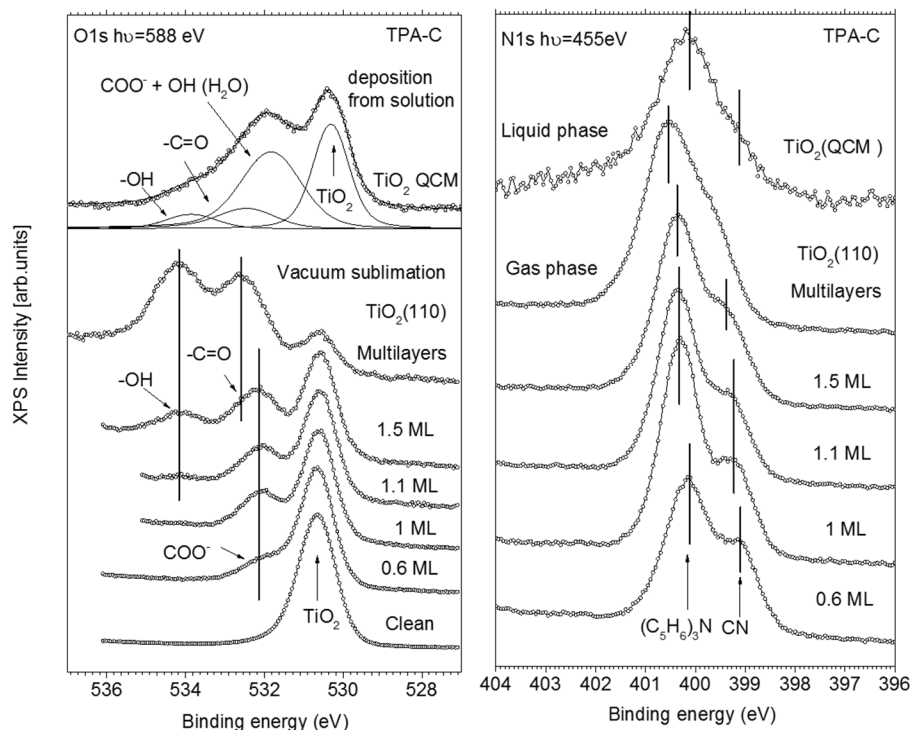


Figure 36: O1s and N1s core level spectra from TPA-C on TiO<sub>2</sub>. Photon energies are indicated in the figure.

## 4.2. Cu<sub>2</sub>O

### 4.2.1. The surface structure of Cu<sub>2</sub>O(100)

Cu<sub>2</sub>O is an important initial and common corrosion product on copper under atmospheric conditions, and thus it is important to understand its structure. In this study, the structure and nature of Cu<sub>2</sub>O is investigated by atomically resolved microscopy (STM) and LEED. The simulation by DFT (density functional theory) is in agreement with the experimental results.

The surface structures relative to the bulk unit cell are (1 × 1), *c*(2 × 2) and two 90° rotational domains of the matrix (3,0;1,1). Parameters like annealing temperature, extending time of annealing, and exposure to oxygen affect the creation of different ordered surface. A summary of surface structure as a function of preparation parameters is shown in table 2-4.

Table 2-4: Different surface structures as a function of preparation parameters (as observed in LEED and STM). Multiple cycles of sputter and anneal in UHV lead to increasing the coverage of  $c(2 \times 2)$  and reduction of the coverage of  $(3,0;1,1)$

Annealing Temperature (°C)	UHV	$3 \times 10^{-6}$ mbar $O_2$		$2 \times 10^{-5}$ mbar $O_2$		
	15 min	15 min	30 min	15 min	30 min	60 min
580	$(3,0;1,1)$ & $c(2 \times 2)$	$(3,0;1,1)$	$(3,0;1,1)$	$(3,0;1,1)$	$(3,0;1,1)$	
630	$(3,0;1,1)$ & $c(2 \times 2)$	$(3,0;1,1)$	$(3,0;1,1)$	$(3,0;1,1)$ & $(2 \times 2)$	$(3,0;1,1)$ & $c(2 \times 2)$	$(3,0;1,1)^{a,b)}$ & $(1 \times 1)^{b)}$
700	$(3,0;1,1)$ & $c(2 \times 2)$	$(3,0;1,1)$				

<sup>a)</sup>  $(3,0;1,1)$  with some double spots, <sup>b)</sup> strong background

Figure 37 shows three different surface termination groups which are measured by LEED and STM experimentally and their simulated STM images by DFT. All  $(1 \times 1)$ ,  $c(2 \times 2)$  and the matrix  $(3,0;1,1)$  structures are observed by STM measurement but the  $(1 \times 1)$  structure is not observed directly by LEED [23]. The reconstructed surface structure of  $(3,0;1,1)$  was gently sputtered to remove the long range atomic order on the surface in order to prepare a  $(1 \times 1)$  structure reflecting the bulk periodicity of  $Cu_2O(100)$  [23]. All three different surface structures measured by LEED and STM were simulated by DFT successfully (last row in Figure 37). The STM images confirmed the unit cell of all ordered surface structures observed in LEED. Since the surface orientation and the scanning direction in the STM measurement are kept similar, it is possible to compare the different structures. All unit cells in the lattice direction are shown in the STM images in red. The lattice structure for  $(1 \times 1)$  is the square with one protrusion per unit cell. Similar lattices are visible in the corresponding DFT-STM image [23]. The  $c(2 \times 2)$  surface structure has a square unit cell aligned  $[01\bar{1}]$  and  $[011]$  directions with one protrusion elongated in the  $[001]$  direction. The corresponding DFT-STM images also show similar elongation [23].

The unit cell of the  $(3,0;1,1)$  reconstructed surface is indicated in the STM image. Protrusions in the  $(3,0;1,1)$  reconstruction are aligned in the  $[011]$  direction but the protrusions are not aligned perpendicular to  $[011]$ . Instead, they aligned in  $[010]$ . Due to high corrugation in the real STM image, the details from the low lying features are not clearly visible. However, by aid of simulated STM images, there is the possibility of showing more details from the lower layers [23]. The wide STM images of the  $(3,0;1,1)$  reconstruction shows that both  $90^\circ$  rotational domains of the matrix  $(3,0;1,1)$  coexist on the same terraces with multiple domain boundaries which generally appear after annealing the surface to  $580^\circ\text{C}$ . Two rotational domains could also grow on the separate terraces which were observed after annealing the surface to  $630^\circ\text{C}$ .



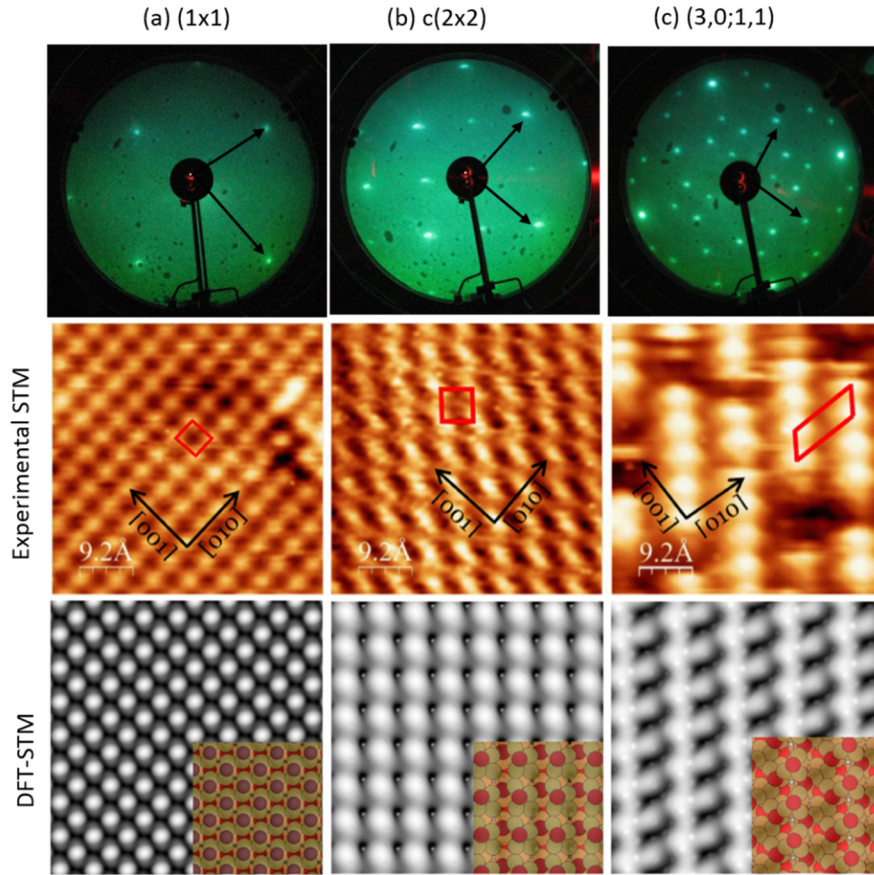


Figure 37: **LEED**-images of (a) (1 $\times$ 1) structure at electron beam energy of 27.6 eV (b)  $c(2\times 2)$  structure at electron beam energy of 37.8 eV (c) the reconstructed (3,0;1,1) surface at electron beam energy of 40.0 eV. The Black arrows indicate the (1 $\times$ 1)-spots. The (0,0) spot is located behind the electron gun at the center of the screen. **STM**-images (46 Å  $\times$  46 Å) of the surface structures. Experimental STM: (a) (1 $\times$ 1) collected at  $V = -1.79$  V,  $I = 0.46$  nA. (b)  $c(2\times 2)$   $V = 1.06$  V,  $I = 0.14$  nA, (c) (3,0;1,1)  $V = 2.78$  V,  $I = 0.31$  nA. **DFT-STM** settings: (a) at  $V = -3$  V bias and probe  $d = 1.9$  Å, (b)  $V = 1$  V,  $d = 2.4$  Å and (c)  $V = 3$  V,  $d = 2.9$  Å. Bright areas correspond to protrusions. Note in (b) that the experimental STM image is distorted by instrumental drift.

The coexistence of the  $c(2 \times 2)$  and (3,0;1,1) structures is recorded in both STM images and LEED patterns, as shown in Figure 38. In LEED patterns the blue and red spot indicate two rotational domains of (3,0;1,1) and yellow spots are representative of the  $c(2 \times 2)$  structure coexisting in the same LEED pattern. The STM image shows both mentioned structures which are adjusted in the same terraces. Both  $c(2 \times 2)$  and (3,0;1,1) structures are lined up in [011] or in an equivalent perpendicular direction [01 $\bar{1}$ ]. The line profile (green line) which is extending on both  $c(2 \times 2)$  and (3,0;1,1) structures show more corrugation in areas with (3,0;1,1) structure in comparison with those having  $c(2 \times 2)$  structure.

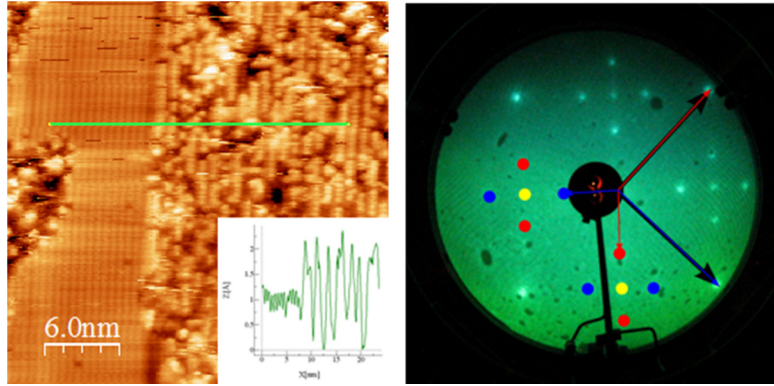


Figure 38: STM-image and LEED-image of coexistence of the  $(3,0;1,1)$ - and  $c(2\times 2)$ -surface structures. **STM** image,  $V = 2.1$  V,  $I = 96$  pA.  $c(2\times 2)$  on the left and  $(3,0;1,1)$  on the right. The line profile (inset) shows more corrugation in reconstructed  $(3,0;1,1)$  than  $c(2\times 2)$ . **LEED** image taken at an electron beam energy of 23.5 eV. The blue and red spots indicate the two rotational domains of  $(3,0;1,1)$  and the yellow spots indicate the  $c(2\times 2)$ -structure.

Figure 39 shows the coexistence of unordered structures within the  $(3,0;1,1)$  structure. Unordered structures were captured after annealing the surface in oxygen at a temperature of 580 °C. Other conditions like multiple cycles of annealing in UHV at similar temperatures, or increasing the annealing temperature in oxygen after sputtering did not result in unordered structure. The explanation for having unordered structure in this particular sample preparation could be due to preventing the surface from getting ordered by oxygen gas at low temperature since the mobility of the surface atoms is increased by the presence of oxygen [153].

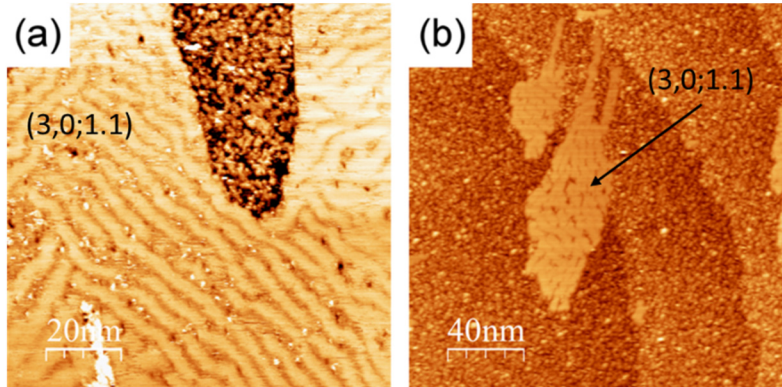


Figure 39: wide area STM-images. (a) Multiple domains of the  $(3,0;1,1)$  structure are surrounding non-ordered structure  $V = 2.32$  V,  $I = 0.212$  nA. (b) Initial formation of the ordered  $(3,0;1,1)$  structure located in the middle of non-ordered structure domains ( $V = 1.58$  V,  $I = 0.634$  nA)

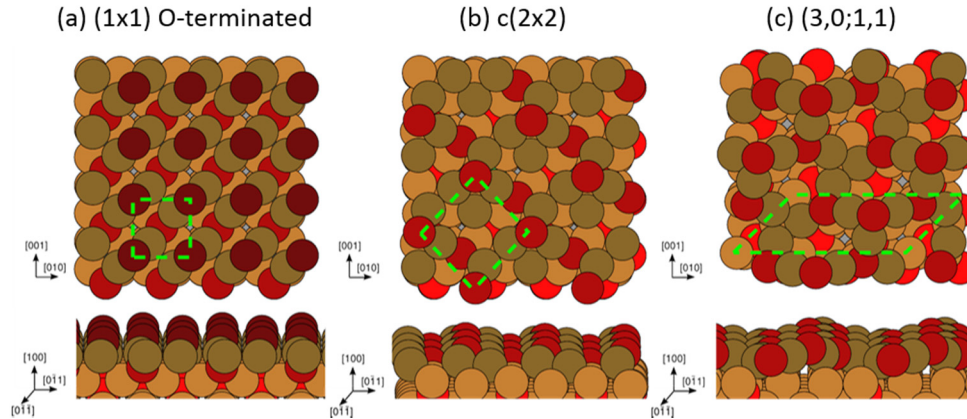


Figure 40: atomic models of the structures from the DFT calculations. The green lines show unit cells. The surface structures (a-c) indicate the experimentally observed surface patterns of  $(1 \times 1)$ ,  $c(2 \times 2)$  and  $(3,0;1,1)$  of  $\text{Cu}_2\text{O}(100)$ . The color codes are  $\text{Cu}_{(\text{surf})}$  (●),  $\text{Cu}_{(\text{bulk})}$  (●),  $\text{O}_{(\text{surf})}$  (●),  $\text{O}_{(\text{bulk})}$  (●) and  $\text{O}_{(\text{term})}$  (●)

The computation of energetically favored surface structures by DFT is shown in Figure 40. The  $(1 \times 1)$  structure is formed by annealing the surface at high oxygen pressure [22]. The  $(1 \times 1)$  oxygen terminated structure is the most stable computed structure under oxygen rich conditions [154]. On the other hand, at the low oxygen (lean) level, the copper termination is more favorably. However,  $(3,0;1,1)$  and  $c(2 \times 2)$  structures were detected experimentally at oxygen gas pressures up to  $2 \times 10^{-5}$  mbar in this work. (Table 2-4)

The spacing between the surface layers in  $(1 \times 1)$  unreconstructed copper termination at low oxygen levels (lean condition) is  $2.16 \text{ \AA}$ . The surface energy calculated is  $0.089 \text{ eV\AA}^{-2}$  which is in agreement with Soon et.al ( $0.091 \text{ eV\AA}^{-2}$ ) [154]. The spacing between the first and second top layers of  $\text{Cu}_2\text{O}$  after relaxation in the normal direction were reduced to  $2.05 \text{ \AA}$  and  $2.08 \text{ \AA}$ , respectively. Consequently, the surface energy of  $(1 \times 1)$  is reduced to  $0.088 \text{ eV\AA}^{-2}$  by normal contraction. With stabilization on the  $(1 \times 1)$  structure, the surface energy reached  $0.075 \text{ eV\AA}^{-2}$ . This reduction in the surface energy was caused by the dimerization of  $\text{Cu}^+$  ions in the  $[011]$  or equivalent directions which has been well studied in other works [22, 155]. The dimerization caused the distance between Cu atoms to change from  $3.05 \text{ \AA}$  to  $2.40 \text{ \AA}$ . More dimerization leads to making an extended one dimensional chain ridge in  $[011]$  with  $c(2 \times 2)$  structure having a surface energy of  $0.073 \text{ eV\AA}^{-2}$  [23]. (See Figure 41).

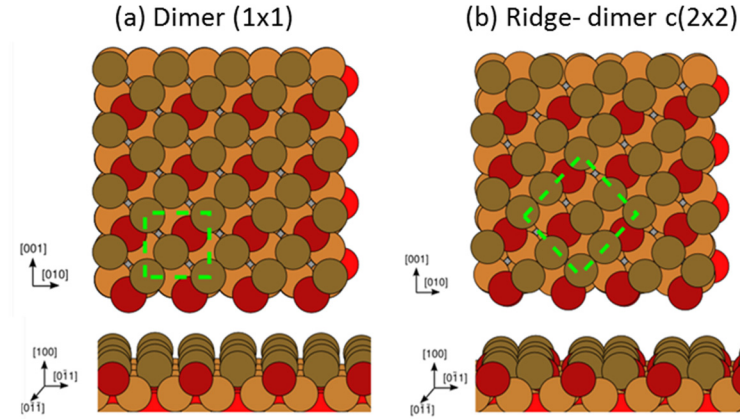


Figure 41: atomic structures indicated by DFT (a) the dimer (1x1) and (b) surface reconstructions of ridge-dimer c(2x2). The surface unit cells are indicated in green lines. The lowest energy structure belongs to both (3,0;1,1) and  $c(2 \times 2)$  unit cells by simulated annealing (SA). All calculated surface energies are summarized in Table 3-4.

The (3,0;1,1) and  $c(2 \times 2)$  structures are reconstructed in both normal and lateral directions which causes the O<sup>2-</sup> layer to intermix with the Cu<sup>+</sup> layer. The surface corrugation is higher for the (3,0;1,1) than  $c(2 \times 2)$  structure which was shown experimentally by STM . (See Figure 38). These properties of reconstructed structures reduce the surface normal dipole moment making these structures favorable surface configurations.

Table 3-4: shows calculated surface energies ( $E_s$ ) of Cu<sub>2</sub>O(100) surface structures by DFT, under lean oxygen conditions

Unit cell	Structure	$E_s$ [eV Å <sup>-2</sup> ]
(1×1)	Unrelaxed <sup>a)</sup>	0.089
(1×1)	Contracted <sup>b)</sup>	0.088
(1×1)	Dimer <sup>c)</sup>	0.075
c(2×2)	Ridge-dimer <sup>d)</sup>	0.073
c(2×2)	Low-energy <sup>e)</sup>	0.071
(3,0;1,1)	Low-energy <sup>e)</sup>	0.071

a) Unreconstructed (1×1) surface.

b) Unreconstructed (1×1) surface relaxed in surface normal direction.

c) Cu<sup>+</sup>-Cu<sup>+</sup> dimerization in the [011] direction.

d) [011]-directed Cu<sup>+</sup> ridge formation via [011] and [01̄1] dimerization.

e) Low-energy structures obtained by Simulated Annealing (SA) MD simulations.

Periodicity of  $(3\sqrt{2} \times \sqrt{2})(\sqrt{2} \times \sqrt{2})R45^\circ$  was proposed for the surface structure by Cox et.al [22]. In this work, the coexistence of (3,0;1,1) and  $c(2 \times 2)$  structures was



observed experimentally by STM and LEED. The presence of a center spot (from  $c(2 \times 2)$  structure) in the LEED pattern means that the coverage of different structures changed. (See Figure 38). The equivalent LEED pattern for the  $(3,0;1,1)$  structure observed in this work had lots of missing spots and was described as a  $(3\sqrt{2} \times \sqrt{2})R45^\circ$  structure with two  $90^\circ$  rotational domains [22].

The  $(3\sqrt{2} \times \sqrt{2})R45^\circ$  unit cell with two  $90^\circ$  rotational domains has one side directed along one of the principle directions with the unit length and the other side with  $3\sqrt{2}/2$  unit length directed  $45^\circ$  off from the chosen principal direction. The corresponding matrix for this unit cell is  $(1,0;1.5,1.5)$ . If  $c(2 \times 2)$  spots in the LEED pattern is misinterpreted as  $(1 \times 1)$  spots, then the proposed structure by Cox et.al was correct. The difference between the proposed structure in this work and Cox is shown in Figure 42.

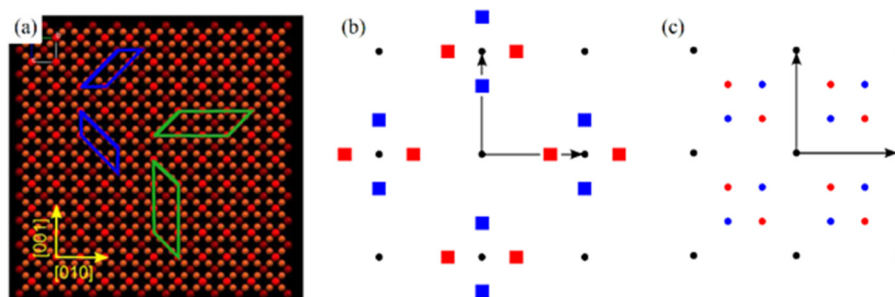


Figure 42: (a) the unit cells in the real space. The blue lines are unit cells which indicated by Shultz and Cox. The green lines are unit cells which are proposed by this study. (b) Structure (blue and red squares) shows The two rotational domains of the  $(1,0;1.5,1.5)$  with black dots that represent the  $(1 \times 1)$ -pattern. (c) The two rotational domains of the  $(3,0;1,1)$  with black dots which represent the  $(1 \times 1)$ -pattern.

#### 4.2.2. Dehydrogenation of methanol on $\text{Cu}_2\text{O}(100)$ and $(111)$

Copper could be a good replacement for noble metal as catalysts for methanol dehydrogenation in the fuel cells [156].  $\text{Cu}_2\text{O}$  is the most and thermodynamically stable phase of corrosion products of copper under catalytic conditions [157, 158]. Naturally, copper is partially or fully oxidized. Therefore, detail study of copper oxide interactions with alcohol is an interesting subject in the field of catalysis. This subject has been investigated by different groups and the studies show different product distribution for each  $\text{Cu}_2\text{O}(111)$  and  $(100)$  [159-161]. In this study,  $\text{Cu}_2\text{O}(111)$  and  $(100)$  surfaces with different structure models, their interaction with methanol (MeOH), and their adsorption sites are investigated in detail.

#### 4.2.2.1. Surface models and adsorption sites for methanol

Figure 43 shows a set of structures for  $\text{Cu}_2\text{O}$ (111) and (100) surfaces. Figure 43 (a) to (d) show the  $\text{Cu}_2\text{O}$  (100) surface including the unreconstructed Cu-terminated  $(1 \times 1)$  surface, ridge-dimer reconstructed  $c(2 \times 2)$  surface,  $\text{O}_{\text{ad}}$   $c(2 \times 2)$  (surface with a surface O atom moved from the lattice to a surface adatom position), and  $(3,0;1,1)$  reconstruction, respectively. Figure 43 (e) to (g) shows the  $\text{Cu}_2\text{O}$  (111) surface including the unreconstructed oxygen terminated  $(1 \times 1)$  surface, the reconstructed  $(\sqrt{3} \times \sqrt{3})R30^\circ$  surface with  $\frac{1}{3}$  monolayer (ML) oxygen vacancies, and  $(\sqrt{3} \times \sqrt{3})R30^\circ$ , with the  $\frac{1}{3}$  ML oxygen vacancies plus a full ML of  $\text{Cu}_{\text{CUS}}$  atom vacancies, respectively. Table 4-1 shows the energetically preferred sites and their respective adsorption energy for each model of both surfaces.

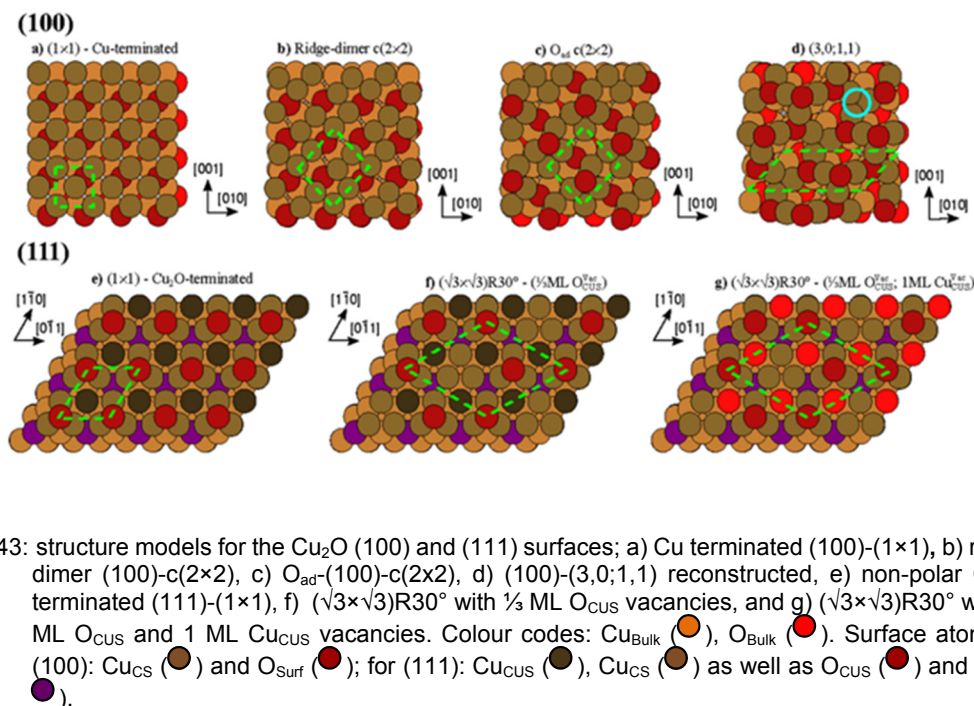


Figure 43: structure models for the  $\text{Cu}_2\text{O}$  (100) and (111) surfaces; a) Cu terminated (100)- $(1 \times 1)$ , b) ridge-dimer (100)- $c(2 \times 2)$ , c)  $\text{O}_{\text{ad}}$ -(100)- $c(2 \times 2)$ , d) (100)- $(3,0;1,1)$  reconstructed, e) non-polar  $\text{Cu}_2\text{O}$  terminated (111)- $(1 \times 1)$ , f)  $(\sqrt{3} \times \sqrt{3})R30^\circ$  with  $\frac{1}{3}$  ML  $\text{O}_{\text{CUS}}$  vacancies, and g)  $(\sqrt{3} \times \sqrt{3})R30^\circ$  with  $\frac{1}{3}$  ML  $\text{O}_{\text{CUS}}$  and 1 ML  $\text{Cu}_{\text{CUS}}$  vacancies. Colour codes:  $\text{Cu}_{\text{Bulk}}$  (orange),  $\text{O}_{\text{Bulk}}$  (red). Surface atoms of (100):  $\text{Cu}_{\text{CS}}$  (brown) and  $\text{O}_{\text{Surf}}$  (red); for (111):  $\text{Cu}_{\text{CUS}}$  (black),  $\text{Cu}_{\text{CS}}$  (brown) as well as  $\text{O}_{\text{CUS}}$  (red) and  $\text{O}_{\text{CS}}$  (purple).

#### *Simulated methanol adsorption on $\text{Cu}_2\text{O}$ (100)*

The unreconstructed (100) surface experiencing Cu-dimerization initiated by adsorption of methanol causes ridge dimer  $c(2 \times 2)$  structure. Methanol binds with the oxygen on the slightly asymmetric bridge site of Cu or binds alcohol hydrogen to the exposed surface oxygen in  $(1 \times 1)$ . However, the dissociation adsorption of methanol is more energetically (1.5 eV) favored than molecular adsorption. The first

step of methanol dissociative adsorption is methoxy (MeO) binding by oxygen to the Cu bridge site and the hydrogen from methanol dissociation adsorbed to the other Cu bridge site (see Table 4-1). As explained above, dimerization of Cu occurs by methanol adsorption. The Cu dimer stays intact under hydrogen, but Cu dimer is elongated by methoxy which will cause the ridge dimer structure to be distorted. Thus, the surface starts to readopt the unreconstructed  $(1 \times 1)$  structure. Cu atoms are flexible while adsorption and desorption processes occur. Dissociative adsorption of methanol on  $(3,0;1,1)$  needs some energy. Therefore, methanol adsorbed molecularly on  $(3,0;1,1)$  is preferred (see Figure 44(a)). By letting the surface atoms move, the reconstruction  $(3,0;1,1)$  will be lifted and the  $(1 \times 1)/c(2 \times 2)$  surface formed (see Figure 44 (d)) which let the dissociated products (methoxy and hydrogen) adsorb onto the surface (see Figure 44 (c)). During the transition from  $(3,0;1,1)$  to  $(1 \times 1)/c(2 \times 2)$  there is an energetically favored  $O_{ad}-c(2 \times 2)$  structure with O atoms moved from the lattice to the surface adatom position (figure 43 (c)) [23]. In the  $O_{ad} c(2 \times 2)$  structure, a hydrogen atom binds to an oxygen adatom and methoxy binds to the Cu bridge site (see Figure 44 (b)).

#### *Simulated methanol $Cu_2O(111)$*

The under coordinated  $Cu_{CUS}$  atom in unreconstructed (111) is the most favorable site for methanol and its dissociative products such as methoxy and hydrogen [162]. Methanol dissociation does not occur during the adsorption onto the unreconstructed ideal (111) surface according to DFT calculations in this work. By removing the  $O_{CUS}$  atoms, methanol dissociation occurs. Preferable sites for adsorption of hydrogen are  $O_{CS}$  and  $Cu_{CUS}$  atoms are suitable sites for methanol and methoxy. Further, the energetically favorable condition for dissociative adsorption is reached while the surface has both  $O_{CUS}$  and  $Cu_{CUS}$  vacancies. In this condition,  $Cu_{CUS}$  vacancies are the available sites for methanol adsorption,  $Cu_{CS}$  atoms are the sites for methoxy adsorption, and hydrogen prefers  $O_{CUS}$ . A particular surface reconstruction with vacancies (the  $(\sqrt{3} \times \sqrt{3})R30^\circ$  surface with  $\frac{1}{3}ML$   $O_{CUS}$  and  $1ML$   $Cu_{CUS}$  vacancies) is considered the best structure for dissociative adsorption, which corresponds to the experimental results for the (111) surface in this work. (See Figure 44)

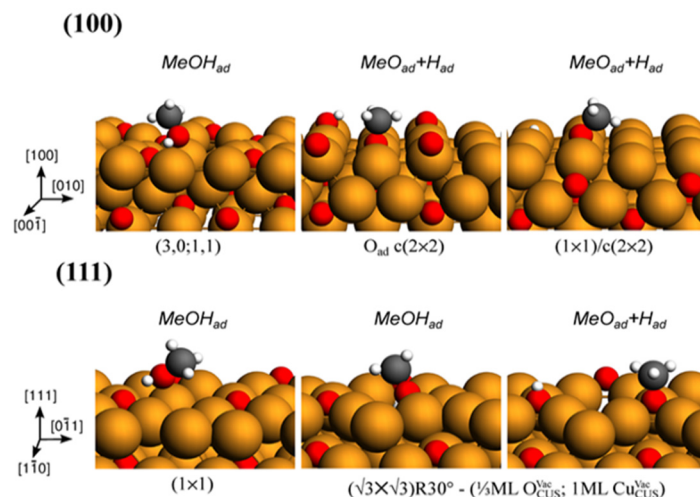


Figure 44: selection of the MeOH adsorption structures. On the **(100)**: initial adsorption state on to the (3,0;1,1) (left), dissociative ME OH adsorption which MeO binds Cu bridge and H binds  $O_{ad}$  c(2x2) intermediate structure (middle), reconstructed surface with MeOH dissociation to form the (1x1)/c(2x2) surface (right). On the **(111)**: the molecular MeOH adsorption onto the  $Cu_{CUS}$  site on ideal (1x1) surface (left), molecular adsorption to the  $Cu_{CUS}$  vacancy of the  $(\sqrt{3} \times \sqrt{3})R30^\circ$  surface with  $\frac{1}{3}ML O_{CUS}$  and 1ML  $Cu_{CUS}$  missing (middle), dissociative adsorption onto the same surface termination (right). Colour codes: Cu (orange), O (red), C (grey) and H (white). Note that the relative sizes of the atoms are not reflecting the true size ratio.

Table 4-4: Preferred adsorption sites and energies for methanol, methoxy, and hydrogen on different  $Cu_2O$ (111) and (100) surface reconstructions.

Surface	Preferred adsorption site			Adsorption energy	
	MeOH	MeO	H	Molecule	Dissociative
<b>(100)</b>					
Ideal - 1x1	Cu bridge	Cu bridge	Cu bridge	-1.1 eV	-2.6 eV
Ridge dimer c(2x2)	Cu bridge	Cu bridge	Cu bridge	-0.8 eV	-2.3 eV
(3,0;1,1)	Cu trimer	Cu trimer	Cu trimer	-0.7 eV	+0.3 eV
<b>(111)</b>					
Ideal - 1x1	$Cu_{CUS}$	$Cu_{CUS}$	$Cu_{CUS}$	-0.9 eV	+0.4 eV
1x1- $O_{CUS}$ -vac	$Cu_{CUS}$	$Cu_{CUS}$	$O_{CS}$	-1.1 eV	-0.2 eV
$(\sqrt{3} \times \sqrt{3})R30^\circ - \frac{1}{3}O_{CUS}$ -vac	$Cu_{CUS}$	$Cu_{CUS}$	$O_{CUS}$	-1.2 eV	-1.0 eV
$(\sqrt{3} \times \sqrt{3})R30^\circ - \frac{1}{3}O_{CUS} + Cu_{CUS}$ -vac	$Cu_{CUS}$ -V	$Cu_{CS}$	$O_{CUS}$	-0.8 eV	-1.4 eV



#### 4.2.2.2. Methanol adsorption on $\text{Cu}_2\text{O}(100)$ and (111)

##### *Experimental results for $\text{Cu}_2\text{O}(100)$*

Methanol was exposed to the  $\text{Cu}_2\text{O}(100)$  surface with three different dosages at 120 K, and then heated up step-wise. Figure 45 shows the O1s spectra for different preparation conditions plus numerical fitting of some selected spectra. O1s spectra numerically fitted with three different components on the clean surface are indicated by B, S1 and S2. (See Figure 45 in the left). Since, the  $\text{Cu}_2\text{O}$  surface, particularly the (100) surface, has problems with charging effects at low temperatures, the B peak which belongs to the bulk oxygen has been positioned at 0 eV. The O1s components at lower binding energies (S1 and S2) are associated with surface oxygen (CuO like) which are known as coordinately unsaturated oxygen anions [23]. After adsorption of 2.8L methanol, S1 and S2 disappeared but two new components appear at high binding energy. The component at 1.1 eV which named A1 is assigned to methoxy and it binds to the surface. The component at 2.3eV named A2 is assigned to methanol and it binds as a second layer (physisorbed). The separation between these two peaks is in agreement with similar work in other groups [163]. However, A1 could be representative of a range of components such as methoxy, formaldehyde and OH with similar O1s binding energy [164, 165]. DFT calculations in this work show that the (3,0;1,1) structure is stabilized to the  $(1 \times 1)/c(2 \times 2)$  structure by methanol adsorption which is more thermodynamically favored. According to the calculation, O1s components at 0.93 eV and 1.95 eV are assigned to methoxy and methanol components, respectively and they are close to the experimentally measured binding energies.

C1s spectra in different dosages, and heat treatment plus numerical fitting of some selected spectra are shown in Figure 46. C1s spectra were numerically fitted with two components during the adsorption indicated by C1 at 286.0 eV and C2 at 286.8 eV (see Figure 46 in the left). The DFT calculations show the 0.65 eV shifts for these components which are assigned to methoxy at lower energy and methanol at higher energy.

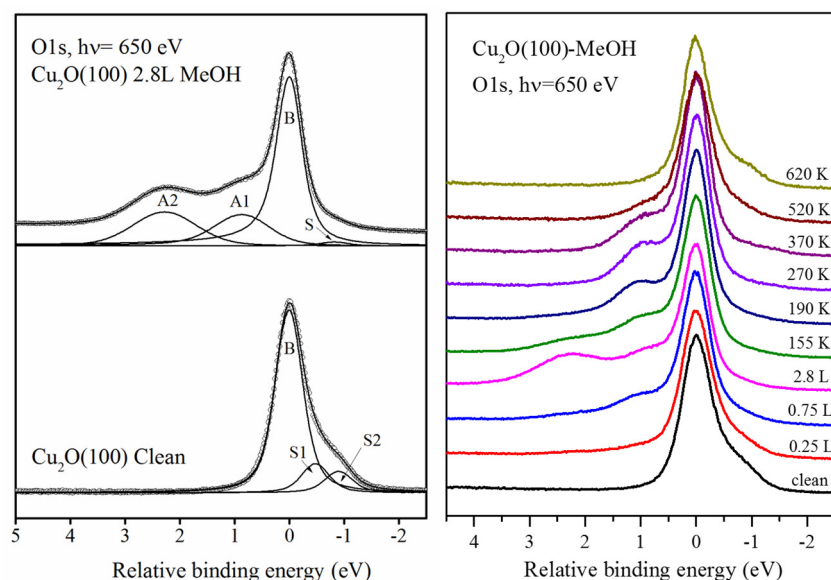


Figure 45: numerical fits of O1s spectra from clean  $\text{Cu}_2\text{O}(100)$  and 2.8L methanol dosage. O1s peak fits with Lorentzian width ( $W_L=0.35$  eV) and variable Gaussian width ( $W_G$ ) between 0.7 to 1.1 eV (Left). O1s spectra recorded from methanol adsorption on  $\text{Cu}_2\text{O}(100)$  for different dosages and heat treatments. The O1s spectra have been aligned to the main peak (Right).

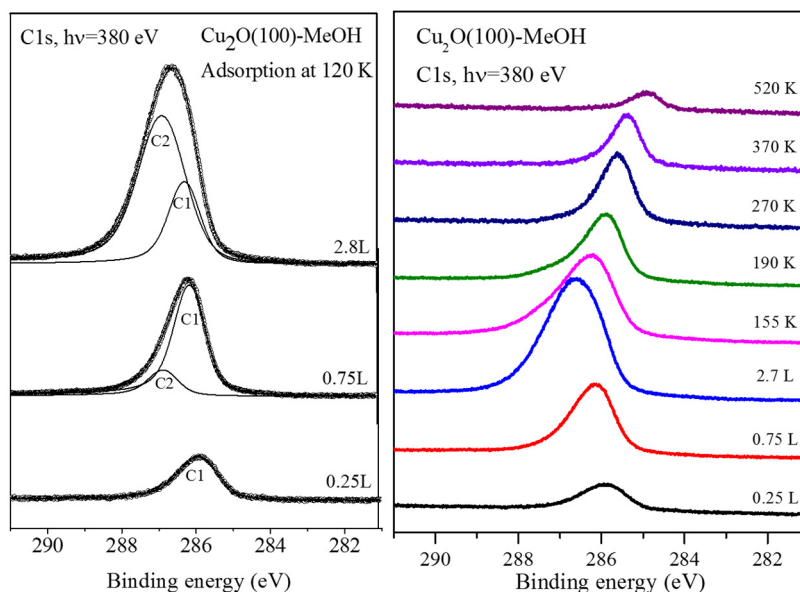


Figure 46: numerical fits of C1s spectra from 0.25L, 0.75L and 2.8L methanol dosed. C1s peak fits with Lorentzian width ( $W_L=0.35$  eV) and variable Gaussian width ( $W_G$ ) between 0.8 to 1.15 eV (Left). C1s spectra recorded from methanol adsorption on  $\text{Cu}_2\text{O}(100)$  for different dosages and heat treatments. The C1s binding energy scale is with respect to the Fermi level (Right).

In Figure 47 the intensities of the O1s peaks (A1 and A2) corresponding to methoxy and methanol are compared with the intensities of these compounds in C1s

peaks (C1 and C2). The intensities of A2 and C2 are perfectly matched in both the adsorption cycle and desorption cycle. Thus, they have not made any chemical modification and they belong to physisorbed layer. The physisorbed layer almost disappeared at 190 K. Further heating of the sample to 270 K shows that the methanol peaks (A2, C2) are completely gone from the surface in agreement with temperature program deposition (TPD) results from Cox et al [160]. After the physisorbed methanol layer is gone, chemisorbed (A1, C1) layer was removed at higher temperature. C1s spectra shift to lower binding energies by increasing the temperature from 285.6 eV (at 270 K) to 285.1 eV (520 K), and then after the adsorbed component are completely gone. The TPD results from ref 161 show the desorption of formaldehyde and hydrogen from the  $\text{Cu}_2\text{O}(100)$  surface after methanol adsorption [160]. Therefore this shift in C1s spectra could be due to more dehydrogenation and formation of formaldehydes.

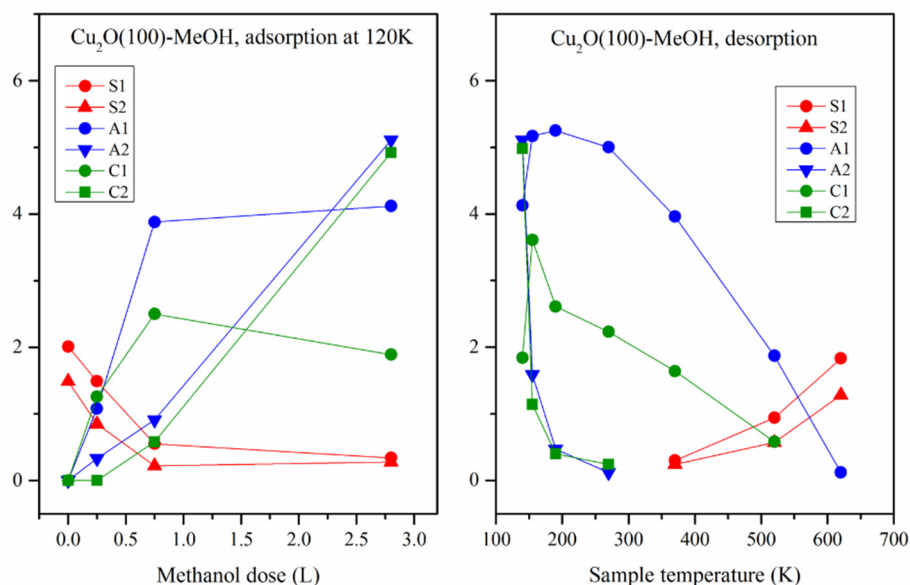


Figure 47: intensities of separate components from the numerical fits of O1s and C1s

In contrast to C2 and A2, development of C1 and A1 during adsorption and annealing are different. A1 decreased slower than C1 when temperature was increased from 180 K to 270 K, whereas the trend of A1 reduction became faster than C1 from 270 K to 520 K. The reason for changes in the C1 and A1 trends during annealing could be due to hydrogen binding with surface oxygen. Atomic hydrogen is released when the methanol becomes dehydrated to methoxy and formaldehyde. Hydrogen in the  $c(2 \times 2)$  structure binds to Cu which does not contribute to the O1s peak. However, during the transition from  $(3,0;1,1)$  to  $(1 \times 1)/c(2 \times 2)$ , there is the possibility of formation of an intermediate  $\text{O}_{\text{ad}}-c(2 \times 2)$  structure. In this structure,

as explained before, oxygen is pushed out to the oxygen adatom position and these adatoms can react with stored atomic hydrogen.

In the other study on the same sample used in this work was done at the same time on the same beamline which using similar experimental parameters, the  $\text{Cu}_2\text{O}(100)$  surface was exposed to water. The intensity ratio of the A1 and B peaks from O1s spectra at 270 K was used for calculation of OH coverage [166]. Since the same experimental parameter were used, the same method can be used here for calculating the A1 coverage. The A1 component in the O1s spectrum has 0.47 ML of oxygen species which includes methoxy, surface hydroxyls and possibly some percentage of formaldehyde.

### *Experimental results for $\text{Cu}_2\text{O}(111)$*

Methanol was exposed to the  $\text{Cu}_2\text{O}(111)$  surface with three different dosages at 120 K and then heated stepwise. Figure 48 shows the O1s and C1s spectra for different preparation conditions plus their intensity evolution. O1s spectra contain a main peak from the emitted electrons from surface ions at lower binding energy which is in agreement with Önsten et.al [164]. Due to methanol adsorption, the surface peak is reduced significantly, but still has small percentage at the 2.8L dosage level. At the same time, broad peaks appear on the higher binding energy side which could be equivalent to A1 and A2 in  $\text{Cu}_2\text{O}(100)$  surface. However, there is no clear separation between the A1 and A2 peaks in both the adsorption and desorption cycles. The adsorption energies of methanol and methoxy on the  $\text{Cu}_2\text{O}(111)$  surface are close and their indicated peaks overlap each other and cause a broader peak on the higher binding energy side. The variety of adsorption sites on the (111) surface is higher than for (100) which could cause the adsorption of mixed methanol/methoxy on different sites of the (111) surface in comparison to bridge sites for methoxy in the (100) surface. (See Table 4-4)

C1s spectra at 0.25 L include a main peak at 286.0 eV and a shoulder at 285.6 eV. After increasing methanol dosage to 0.75 L, C1s broadens at higher binding energies with a shoulder around 286.5 eV. The main peak at higher binding energy (at 286.0 eV) is assigned to a physisorbed layer of methanol that binds on top of the site  $\text{Cu}_{\text{CS}}$ . The component at lower binding energy (at 285.6 eV) is assigned to methoxy and binds in a hollow site of the  $\text{Cu}_{\text{CS}}$  trimer. After increasing dosage to 2.8 L, one peak is resolved around 286.6 eV (similar to (100)). At higher coverage the trimer site will be less favorable to more adsorbate. The integrated intensity of C1s spectra from methanol adsorption at 2.8 L on  $\text{Cu}_2\text{O}(111)$  is slightly higher than on  $\text{Cu}_2\text{O}(100)$ . Therefore, the 2.8 L methanol dosage on  $\text{Cu}_2\text{O}(111)$  results in creation of a bi-layer with both methoxy and methanol.

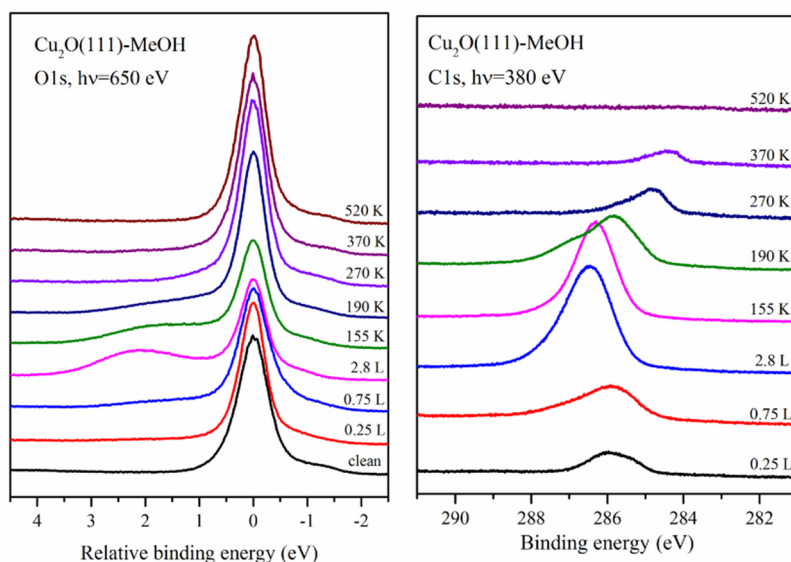


Figure 48: O1s and C1s spectra in different methanol dosage and step wise heating treatment of  $\text{Cu}_2\text{O}(111)$ . The O1s spectra have been aligned to the main peak, whereas the C1s binding energy scale is with respect to the Fermi level.

Heating the sample from 155 K to 190 K causes reduction of the C1s intensity mostly due to desorption of the physisorbed layer. There are two peaks at 190 K; methoxy at 286.0 eV and methanol at 287.1 eV. Increasing the temperature to 270 K causes a negative shift in binding energy to  $\sim 285$  eV and further heating (370 K) even shifts C1s more to 284.4 eV. The binding energy shift stems from dehydrogenation during increase in temperature. Since the shifts in binding energy of C1s spectra due to temperature are larger for (111) than for (100), it indicates that more dehydrogenation happens on (111) than on (100). CO desorption from  $\text{Cu}_2\text{O}(111)$  dosed with methanol was detected in TPD by Cox et.al [160]. The study by Sun et.al showed CO binding to the metal ions with C down geometry [167], but dehydrogenation of formaldehyde will eventually lead to formation of CO with oxygen facing the surface and binding with Cu. The individual CO adsorption on  $\text{Cu}_2\text{O}(100)$  shows the CO binding energy to be 288 eV, but the calculation shows that CO with the oxygen-down geometry to the Cu surface has a much lower binding energy than for the C-down geometry [167].

In contrast to development of O1s (A1) and C1s (C1) at (100), the variation of O1s (A1+A2) and C1s in (111) surfaces during both adsorption and desorption are very similar (see Figure 48 right). This is due to the lower surface hydrogen binding contribution in O1s for the (111) sample. The question arises - why less hydrogen when there is a greater possibility of dehydrogenation? The answer is that atomic hydrogen adsorbs on the surface oxygen and are stored until other atomic hydrogen

comes. Then hydrogen desorbs molecularly from the surface. The (111) surface with  $1/3$  ML oxygen vacancies and  $2/3$  ML oxygen on the surface has a high number of adsorption sites for storage of atomic hydrogen at short distances which will lead to formation of  $H_2$  and, consequently, dehydrogenation at lower temperatures.

## 5. Conclusions

The specific objective of this thesis is to investigate the surface structure of metal and metal oxides and the effect of thin films of adsorbates on their characteristics. One important motive for these studies is to compare the investigated system under different conditions such as atmospheric, in aqueous solution, as well as under high vacuum.

Self-assembled monolayers (SAMs) on a gold surface is evaluated in detail in the first part of this thesis (section 4-1). SAMs are made under different kind of depositions such as from liquid solution or gas deposition.

The SAMs consisting of a single type of thiol with polar termination groups have an ordered structure which adsorb conventionally via sulfur groups on the surface and their alkyl chains are axially upright to the surface plane. These functional groups respond to changes of pH in an aqueous medium. Therefore, mixtures of thiols with polar termination groups are more flexible in modifying the surface for different applications. The result from this work shows that mixed SAMs made by thiols with polar terminal groups behave quite differently from unmixed SAMs. The difference in behavior stems from the adsorption of complexes formed in solution due to hydrogen bond formation. The observed mixed MPA/AUT layers are less sensitive and more stable when subject to pH changes, and are more robust when nano-shaved than unmixed SAMs. These properties could be utilized in biomimetic surface and adhesion modification systems. For example, the complexes observed in this system incorporate essential charged groups present at the hair surface and constitutes a versatile biomimetic model for studying stimuli-dependent surface properties of interest in cosmetics.

Comparing the deposition of thiols from solution and gas deposition (sublimation in UHV) could reveal the mechanism of thiols/selenol adsorption or the role of contamination in the creation of SAMs. Se-C cleavage in organoselenium compounds which hinder the use of these biocompatible compounds has been reported in previous studies. Contamination is claimed as one of the possible reasons for this dissociation. The strength of Se-C bonds was calculated by DFT. However, the Se-C dissociation is not well understood. In the selenol study, where adsorption was accomplished by sublimation in UHV, STM images show clearly where the Se-C dissociation occurs. Dissociation of Se-C bond occurs primarily at step edges. Atoms at steps with lower coordination have more reactivity than atoms on the terrace.

The last section in the first part of thesis evaluates the adsorption of two different dye molecules on TiO<sub>2</sub> surfaces and compares the effect of their structure on the adsorption mechanism. The adsorption mechanism and the equilibrium constant for the adsorption is determined by investigation of adsorbed amount as a function of

dye concentration for two different dyes. The effect of deposition from liquid or by sublimation are investigated. In DSSCs, it is very important that adsorption not exceed more than a monolayer or agglomeration in the adsorbed dye films will occur. This type of work could be very helpful for designing more efficient dye molecules which have less possibility of agglomeration or less interaction between dye molecules.

The second part of the thesis (section 4-2) focuses mainly on  $\text{Cu}_2\text{O}(100)$  and  $(111)$  surfaces. An accurate picture of the structure of the  $\text{Cu}_2\text{O}(100)$  surface was obtained experimentally and the results were in agreement with DFT calculations. Surface structure relative to the bulk unit cell suggested in earlier studies is corrected in this work, and the creation of different ordered surfaces is explained in detail. The interaction of methanol with  $\text{Cu}_2\text{O}(100)$  and  $(111)$  surfaces having different surface structures and associated adsorption sites is investigated in detail by PES and DFT simulation. This work contributes to research on  $\text{Cu}_2\text{O}$  materials such as copper oxide based catalysts in fuel cells or in photocatalytic water splitting. Knowledge about the surface structure could lead to an understanding of the reaction between  $\text{Cu}_2\text{O}$  and adsorbates.



## 6. Acknowledgements

I would like to thank many people who were involved in my work and my life during my PhD years.

Professor Mats Göthelid - it has been honor to work under your valuable supervision. Thanks for trusting me and encouraging me to continue even after the first project gave me lots of challenges. Your knowledge and wisdom are impressive and come with a good sense of humor. I appreciate all your support during these years. Singing opera or even some Persian songs makes the lab more fun. I am happy that the new PhD adds to the symphony by whistling with you, and those in your corridor seem to enjoy it.

Professor Mark Rutland, I would like to thank you for being my co- supervisor. Although, we sometimes have different ideas I am grateful for your support, especially during the time after my accident. It was the most difficult time of my life and you made me feel like a family member. Our discussions and your deep insight into surface chemistry gave me opportunities to learn more and become more interested in this field.

Dr. Magnus Johnson, when I started in Surfcorr I was supposed to work with you. Scientific research takes its own path so it turns out that we have not worked much in your field of expertise, but it was a pleasure getting to know you

Dr. Deborah Wakeham, it was my pleasure to work with you. Despite that you were always working on lots of projects, you always gave me your time, especially when I could not find answers for my organic chemistry questions. I learn a lot from you, thanks.

Dr. Anneli Önsten, I would like to thank you for supporting me through all the years that I have known you, even before I started my PhD. You have a very good sense of humor and I enjoyed all time I spent with you.

Dr. Eric Tyrode, you were very helpful and I appreciate your guidance.

Dr Jonas Weissenrieder, it was my pleasure to work with you and I learned a lot during the beamline in MAX lab. Your deep insight into surface study gave me opportunities to learn more and become more interested.

Professor Per Classon, I did not have a chance to work with you, but your support during these years was very meaningful for me.

Professor Christofer Leygraf, it is my great pleasure to meet you here.

Dr Ruben Alvarez, you were very helpful and I appreciate your company and your guide line in the AFM measurement in my first project.

Madeleine Printzsköld, thanks for your kind support during these years.

The financial support from the Swedish Research Council (VR) is gratefully acknowledged. I would like to acknowledge our collaborator, Dr Mikko Kanerva from Aalto University and the Synoste company.

I would like to thank all co-authors, *Gustavo S. Luengo, Andrew Greaves, Prof Inger Odnevall Wallinder, Milad Ghadami, Shun Yu, Haining Tian* thanks for the valuable scientific collaboration. Special thanks to *Matthew Fielden* for helping me to know more about AFM. Special thanks to Markus Soldemo for being the best colleague anyone could have. Your sense of humor and your supportive behavior made MAX lab as an interesting place for work.

I would like to thank all my colleges at *ICT Kista, SP and Surfcorr* for making such a nice place to work. I would like to dedicate a special thanks to a few colleagues and friends who have helped me during this research. To *Dr Anna Maria Elert, Dr Andra Dédinaité, Dr Eva Blomberg, Dr Abhilash Sugunan, Karin Törne, Dr Annika Dahlman, Dr Niklas Nordgren and Mikael Sundin*. Thanks to *Dr Esben Thormann* and *Shadi* as a good friend and colleagues who were very nice and supportive. To current and past PhD candidates *Majid, Golorkh, Maziar, Neda, Akanksha, Sulena, Krishnan, Mahtab*, both *Maria* in *SP* and new *Marie, Adrien, Elizaveta, Laetitia, Rasmus, Gunnar, Petru, Jesper, Elenora, Mattias, Chao, Min, Tingru, Litao, Chengdong, Illia*, and master student *Maria Eliza, Angelika, Rebeka and Sepideh*. Thanks to my office mate, *Olga, Xian, Junxue, Yousef, Gen and Xiaoyan*. My sincere thanks also go to Jonathan Liljeblad for all his support and advice during these years. *Hui* thanks for company me in the office during cold dark January this year.

Thanks to my friends who make my life happier here, *Iman, Sooror, Sahar, Amir, Mansor, Bitu, Euhanna, Elahe, Behdad, Alibaba, Roya and Danuta*. Thanks to Afrooz who always there for me.

My deepest gratitude is going to my parents, sisters and brothers. You are the best people in my life and I feel very strong bond between us. Mom and Dad I would not be reach here without your support. *Jaleh, Ali, Amir Jamshid, Khale Aghdas and Amo Hoshang* you are the best. Thanks for all support you gave me these years. My sweet *Ahora and Anita*, I love you. *Mitra* you are my best friend before being my sister. I learn most of the life experience from you. I always admire your personality, your kind heart. If somebody were to ask me who my hero is, I would say your name.

مادر مهربانم پدر عزیزم از همه زحمت های بی دریغتان متشکرم و سپاسگذارم.

## References

- [1] K.B. Blodgett, I. Langmuir, Built-up films of barium stearate and their optical properties, *Physical Review* 51(11) (1937) 964-982.
- [2] K.B. Blodgett, Films built by depositing successive monomolecular layers on a solid surface, *Journal of the American Chemical Society* 57(6) (1935) 1007-1022.
- [3] J.C. Love, L.A. Estroff, J.K. Kriebel, R.G. Nuzzo, G.M. Whitesides, Self-assembled monolayers of thiolates on metals as a form of nanotechnology, *Chemical Reviews* 105(4) (2005) 1103-1170.
- [4] F. Schreiber, Structure and growth of self-assembling monolayers, *Progress in Surface Science* 65(5-8) (2000) 151-257.
- [5] O.V. Krylov, *Catalysis by nonmetals: rules for catalyst selection*, Academic Press 2013.
- [6] J. Shen, W. Shan, Y. Zhang, J. Du, H. Xu, K. Fan, W. Shen, Y. Tang, Gas-phase selective oxidation of alcohols: In situ electrolytic nano-silver/zeolite film/copper grid catalyst, *Journal of Catalysis* 237(1) (2006) 94-101.
- [7] K.L. Deutsch, B.H. Shanks, Active species of copper chromite catalyst in C-O hydrogenolysis of 5-methylfurfuryl alcohol, *Journal of Catalysis* 285(1) (2012) 235-241.
- [8] C.E.D. Chidsey, D.N. Loiacono, T. Sleator, S. Nakahara, STM study of the surface morphology of gold on mica, *Surface Science* 200(1) (1988) 45-66.
- [9] Y. Tolstova, S.T. Omelchenko, A.M. Shing, H.A. Atwater, Heteroepitaxial growth of Pt and Au thin films on MgO single crystals by bias-assisted sputtering, *Scientific Reports* 6 (2016) 23232.
- [10] A.R. Sandy, S.G.J. Mochrie, D.M. Zehner, K.G. Huang, D. Gibbs, Structure and phases of the Au(111) surface: X-ray-scattering measurements, *Physical Review B* 43(6) (1991) 4667-4687.
- [11] J.V. Barth, H. Brune, G. Ertl, R.J. Behm, Scanning tunneling microscopy observations on the reconstructed Au(111) surface - atomic-structure, long-range superstructure, rotation domains, and surface-defects, *Physical Review B* 42(15) (1990) 9307-9318.
- [12] J.A. Strosio, D.T. Pierce, R.A. Dragoset, P.N. First, Microscopic aspects of the initial growth of metastable fcc iron on Au(111), *Journal of Vacuum Science & Technology A* 10(4) (1992) 1981-1985.
- [13] K. Nakata, A. Fujishima, TiO<sub>2</sub> photocatalysis: Design and applications, *Journal of Photochemistry and Photobiology C: Photochemistry Reviews* 13(3) (2012) 169-189.
- [14] A.L. Linsebigler, G. Lu, J.T. Yates, Photocatalysis on TiO<sub>2</sub> surfaces: Principles, mechanisms, and selected results, *Chemical Reviews* 95(3) (1995) 735-758.
- [15] J. Nisar, Z. Topalian, A. De Sarkar, L. Österlund, R. Ahuja, TiO<sub>2</sub>-based gas sensor: A possible application to SO<sub>2</sub>, *ACS Applied Materials & Interfaces* 5(17) (2013) 8516-8522.
- [16] M. Grätzel, Dye-sensitized solar cells, *Journal of Photochemistry and Photobiology C: Photochemistry Reviews* 4(2) (2003) 145-153.

- [17] P. Poizot, S. Laruelle, S. Grugeon, L. Dupont, J.M. Tarascon, Nano-sized transition-metal oxides as negative-electrode materials for lithium-ion batteries, *Nature* 407(6803) (2000) 496-499.
- [18] C.M. McShane, K.S. Choi, Photocurrent enhancement of n-type  $\text{Cu}_2\text{O}$  electrodes achieved by controlling dendritic branching growth, *Journal of the American Chemical Society* 131(7) (2009) 2561-2569.
- [19] R.G. Herman, K. Klier, G.W. Simmons, B.P. Finn, J.B. Bulko, T.P. Kobylinski, Catalytic synthesis of methanol from  $\text{COH}_2$ : I. Phase composition, electronic properties, and activities of the  $\text{Cu/ZnO/M}_2\text{O}_3$  catalysts, *Journal of Catalysis* 56(3) (1979) 407-429.
- [20] J. Kondo,  $\text{Cu}_2\text{O}$  as a photocatalyst for overall water splitting under visible light irradiation, *Chemical Communications* (3) (1998) 357-358.
- [21] A. Önsten, M. Göthelid, U.O. Karlsson, Atomic structure of  $\text{Cu}_2\text{O}(111)$ , *Surface Science* 603(2) (2009) 257-264.
- [22] K.H. Schulz, D.F. Cox, Photoemission and low-energy-electron-diffraction study of clean and oxygen-dosed  $\text{Cu}_2\text{O}$  (111) and (100) surfaces, *Physical Review B* 43(2) (1991) 1610-1621.
- [23] M. Soldemo, J.H. Stenlid, Z. Besharat, M. Ghadami Yazdi, A. Önsten, C. Leygraf, M. Göthelid, T. Brinck, J. Weissenrieder, The surface structure of  $\text{Cu}_2\text{O}(100)$ , *The Journal of Physical Chemistry C* 120(8) (2016) 4373-4381.
- [24] P.E. Laibinis, M.A. Fox, J.P. Folkers, G.M. Whitesides, Comparisons of self-assembled monolayers on silver and gold: mixed monolayers derived from  $\text{HS}(\text{CH}_2)_{21}\text{X}$  and  $\text{HS}(\text{CH}_2)_{10}\text{Y}$  ( $\text{X}, \text{Y} = \text{CH}_3, \text{CH}_2\text{OH}$ ) have similar properties, *Langmuir* 7(12) (1991) 3167-3173.
- [25] P.E. Laibinis, G.M. Whitesides, .Omega.-terminated alkanethiolate monolayers on surfaces of copper, silver, and gold have similar wettabilities, *Journal of the American Chemical Society* 114(6) (1992) 1990-1995.
- [26] C. Bertoni, D. Gallardo, S. Dunn, N. Gaponik, A. Eychmüller, Fabrication and characterization of red-emitting electroluminescent devices based on thiol-stabilized semiconductor nanocrystals, *Applied Physics Letters* 90(3) (2007) 034107.
- [27] M.D. Malinsky, K.L. Kelly, G.C. Schatz, R.P. Van Duyne, Chain length dependence and sensing capabilities of the localized surface plasmon resonance of silver nanoparticles chemically modified with alkanethiol self-assembled monolayers, *Journal of the American Chemical Society* 123(7) (2001) 1471-1482.
- [28] A.D. McFarland, R.P. Van Duyne, Single silver nanoparticles as real-time optical sensors with zeptomole sensitivity, *Nano Letters* 3(8) (2003) 1057-1062.
- [29] E. Ruckenstein, Z.F. Li, Surface modification and functionalization through the self-assembled monolayer and graft polymerization, *Advances in Colloid and Interface Science* 113(1) (2005) 43-63.
- [30] E.L. Hanson, J. Schwartz, B. Nickel, N. Koch, M.F. Danisman, Bonding self-assembled, compact organophosphonate monolayers to the native oxide surface of silicon, *Journal of the American Chemical Society* 125(51) (2003) 16074-16080.
- [31] C. Vericat, M.E. Vela, G. Benitez, P. Carro, R.C. Salvarezza, Self-assembled monolayers of thiols and dithiols on gold: new challenges for a well-known system, *Chemical Society Reviews* 39(5) (2010) 1805-1834.

- [32] S. Ferretti, S. Paynter, D.A. Russell, K.E. Sapsford, D.J. Richardson, Self-assembled monolayers: a versatile tool for the formulation of bio-surfaces, *TrAC Trends in Analytical Chemistry* 19(9) (2000) 530-540.
- [33] N.T. Flynn, T.N.T. Tran, M.J. Cima, R. Langer, Long-term stability of self-assembled monolayers in biological media, *Langmuir* 19(26) (2003) 10909-10915.
- [34] V. Chaudhari, H.M.N. Kotresh, S. Srinivasan, V.A. Esaulov, Substitutional self-assembly of alkanethiol and selenol SAMs from a lying-down doubly tethered butanedithiol SAM on gold, *The Journal of Physical Chemistry C* 115(33) (2011) 16518-16523.
- [35] S. Pawsey, K. Yach, L. Reven, Self-assembly of carboxyalkylphosphonic acids on metal oxide powders, *Langmuir* 18(13) (2002) 5205-5212.
- [36] C.D. Bain, G.M. Whitesides, Formation of monolayers by the coadsorption of thiols on gold: variation in the length of the alkyl chain, *Journal of the American Chemical Society* 111(18) (1989) 7164-7175.
- [37] M. Irie, Light-induced reversible pH change, *Journal of the American Chemical Society* 105(7) (1983) 2078-2079.
- [38] S. Wang, Y. Song, L. Jiang, Photoresponsive surfaces with controllable wettability, *Journal of Photochemistry and Photobiology C: Photochemistry Reviews* 8(1) (2007) 18-29.
- [39] C.D. Bain, G.M. Whitesides, A study by contact angle of the acid-base behavior of monolayers containing .omega.-mercaptocarboxylic acids adsorbed on gold: an example of reactive spreading, *Langmuir* 5(6) (1989) 1370-1378.
- [40] D. Burshtain, D. Mandler, The effect of surface attachment on ligand binding: studying the association of  $Mg^{2+}$ ,  $Ca^{2+}$  and  $Sr^{2+}$  by 1-thioglycerol and 1, 4-dithiothreitol monolayers, *Physical Chemistry Chemical Physics* 8(1) (2006) 158-164.
- [41] P.L. Schilardi, P. Dip, P.C. dos Santos Claro, G.A. Benítez, M.H. Fonticelli, O. Azzaroni, R.C. Salvarezza, Electrochemical deposition onto self-assembled monolayers: New insights into micro-and nanofabrication, *Chemistry A European Journal* 12(1) (2006) 38-49.
- [42] C.D. Bain, J. Evall, G.M. Whitesides, Formation of monolayers by the coadsorption of thiols on gold: variation in the head group, tail group, and solvent, *Journal of the American Chemical Society* 111(18) (1989) 7155-7164.
- [43] C.D. Bain, G.M. Whitesides, Molecular-level control over surface order in self-assembled monolayer films of thiols on gold, *Science* 240(4848) (1988) 62-63.
- [44] A. Ulman, Formation and structure of self-assembled monolayers, *Chemical Reviews* 96(4) (1996) 1533-1554.
- [45] C.D. Bain, E.B. Troughton, Y.T. Tao, J. Evall, G.M. Whitesides, R.G. Nuzzo, Formation of monolayer films by the spontaneous assembly of organic thiols from solution onto gold, *Journal of the American Chemical Society* 111(1) (1989) 321-335.
- [46] G.E. Poirier, M.J. Tarlov, H.E. Rushmeier, Two-dimensional liquid phase and the  $\sqrt{3} \times \sqrt{3}$  phase of alkanethiol self-assembled monolayers on Au(111), *Langmuir* 10(10) (1994) 3383-3386.
- [47] O. Dannenberger, M. Buck, M. Grunze, Self-assembly of n-alkanethiols: a kinetic study by second harmonic generation, *The Journal of Physical Chemistry B* 103(12) (1999) 2202-2213.

- [48] G.E. Poirier, Coverage-dependent phases and phase stability of decanethiol on Au(111), *Langmuir* 15(4) (1999) 1167-1175.
- [49] G. Poirier, E. Pylant, The self-assembly mechanism of alkanethiols on Au (111), *Science* 272(5265) (1996) 1145.
- [50] G. Yang, G.y. Liu, New insights for self-assembled monolayers of organothiols on Au(111) revealed by scanning tunneling microscopy, *The Journal of Physical Chemistry B* 107(34) (2003) 8746-8759.
- [51] H. Wu, K. Sotthewes, A. Kumar, G.J. Vancso, P.M. Schön, H.J. Zandvliet, Dynamics of decanethiol self-assembled monolayers on Au (111) studied by time-resolved scanning tunneling microscopy, *Langmuir* 29(7) (2013) 2250-2257.
- [52] K. Sotthewes, H. Wu, A. Kumar, G.J. Vancso, P.M. Schön, H.J. Zandvliet, Molecular dynamics and energy landscape of decanethiolates in self-assembled monolayers on Au (111) studied by scanning tunneling microscopy, *Langmuir* 29(11) (2013) 3662-3667.
- [53] J.D. Monnell, J.J. Stapleton, J.J. Jackiw, T. Dunbar, W.A. Reinert, S.M. Dirk, J.M. Tour, D.L. Allara, P.S. Weiss, Ordered local domain structures of decaneselenolate and dodecaneselenolate monolayers on Au{111}, *The Journal of Physical Chemistry B* 108(28) (2004) 9834-9841.
- [54] S.B. Darling, A.W. Rosenbaum, Y. Wang, S.J. Sibener, Coexistence of the  $(23 \times \sqrt{3})$  Au(111) reconstruction and a striped phase self-assembled monolayer, *Langmuir* 18(20) (2002) 7462-7468.
- [55] G.E. Poirier, W.P. Fitts, J.M. White, Two-dimensional phase diagram of decanethiol on Au(111), *Langmuir* 17(4) (2001) 1176-1183.
- [56] H. Grönbeck, M. Odellius, Photoemission core-level shifts reveal the thiolate-Au(111) interface, *Physical Review B* 82(8) (2010) 085416.
- [57] P. Maksymovych, D.C. Sorescu, J.T. Yates, Gold-adatom-mediated bonding in self-assembled short-chain alkanethiolate species on the Au(111) surface, *Physical Review Letters* 97(14) (2006).
- [58] P. Maksymovych, O. Voznyy, D.B. Dougherty, D.C. Sorescu, J.T. Yates Jr, Gold adatom as a key structural component in self-assembled monolayers of organosulfur molecules on Au(1 1 1), *Progress in Surface Science* 85(5-8) (2010) 206-240.
- [59] A. Chaudhuri, T.J. Lerotoli, D.C. Jackson, D.P. Woodruff, V.R. Dhanak, The local adsorption structure of methylthiolate and butylthiolate on Au(1 1 1): a photoemission core-level shift investigation, *Surface Science* 604(2) (2010) 227-234.
- [60] D.P. Woodruff, The interface structure of n-alkylthiolate self-assembled monolayers on coinage metal surfaces, *Physical Chemistry Chemical Physics* 10(48) (2008) 7211-7221.
- [61] O. Azzaroni, M.E. Vela, H. Martin, A. Hernández Creus, G. Andreassen, R.C. Salvarezza, Electrodesorption kinetics and molecular interactions at negatively charged self-assembled thiol monolayers in electrolyte solutions, *Langmuir* 17(21) (2001) 6647-6654.
- [62] E.J. Calvo, M.S. Rothacher, C. Bonazzola, I.R. Wheeldon, R.C. Salvarezza, M.E. Vela, G. Benitez, Biomimetics with a self-assembled monolayer of catalytically active tethered isoalloxazine on Au, *Langmuir* 21(17) (2005) 7907-7911.

- [63] N. Camillone, C.E.D. Chidsey, G.y. Liu, G. Scoles, Superlattice structure at the surface of a monolayer of octadecanethiol self-assembled on Au(111), *The Journal of Chemical Physics* 98(4) (1993) 3503-3511.
- [64] G.E. Poirier, M.J. Tarlov, The  $c(4\times 2)$  superlattice of n-alkanethiol monolayers self-assembled on Au(111), *Langmuir* 10(9) (1994) 2853-2856.
- [65] D. Anselmetti, A. Baratoff, H.J. Güntherodt, E. Delamarche, B. Michel, G. Ch, H. Kang, H. Wolf, H. Ringsdorf, Domain and molecular superlattice structure of dodecanethiol self-assembled on Au(111), *EPL (Europhysics Letters)* 27(5) (1994) 365.
- [66] M. Tachibana, K. Yoshizawa, A. Ogawa, H. Fujimoto, R. Hoffmann, Sulfur-gold orbital interactions which determine the structure of alkanethiolate/Au(111) self-assembled monolayer systems, *The Journal of Physical Chemistry B* 106(49) (2002) 12727-12736.
- [67] J. Gottschalck, B. Hammer, A density functional theory study of the adsorption of sulfur, mercapto, and methylthiolate on Au(111), *The Journal of Chemical Physics* 116(2) (2002) 784-790.
- [68] T. Hayashi, Y. Morikawa, H. Nozoye, Adsorption state of dimethyl disulfide on Au(111): Evidence for adsorption as thiolate at the bridge site, *The Journal of Chemical Physics* 114(17) (2001) 7615-7621.
- [69] X. Torrelles, C. Vericat, M.E. Vela, M.H. Fonticelli, M.A. Daza Millone, R. Felici, T.L. Lee, J. Zegenhagen, G. Muñoz, J.A. Martín-Gago, R.C. Salvarezza, Two-site adsorption model for the  $(\sqrt{3} \times \sqrt{3})\text{-R}30^\circ$  dodecanethiolate lattice on Au(111) surfaces, *The Journal of Physical Chemistry B* 110(11) (2006) 5586-5594.
- [70] P. Maksymovych, D.C. Sorescu, J.T. Yates, Gold-adatom-mediated bonding in self-assembled short-chain alkanethiolate species on the Au(111) surface, *Physical Review Letters* 97(14) (2006) 146103.
- [71] L. Ferrighi, Y.x. Pan, H. Grönbeck, B. Hammer, Study of alkylthiolate self-assembled monolayers on Au(111) using a semilocal meta-GGA density functional, *The Journal of Physical Chemistry C* 116(13) (2012) 7374-7379.
- [72] A. Chaudhuri, T.J. Lerotoli, D.C. Jackson, D.P. Woodruff, V. Dhanak, Local methylthiolate adsorption geometry on Au(111) from photoemission core-level shifts, *Physical Review Letters* 102(12) (2009) 126101.
- [73] K.F. Tonigold, A. Groß, A systematic DFT study of substrate reconstruction effects due to thiolate and selenolate adsorption, *Surface Science* 640 (2015) 18-24.
- [74] D.K. Schwartz, Mechanisms and kinetics of self-assembled monolayer formation *Annual Review of Physical Chemistry* 52(1) (2001) 107-137.
- [75] K.A. Peterlinz, R. Georgiadis, In situ kinetics of self-assembly by surface plasmon resonance spectroscopy, *Langmuir* 12(20) (1996) 4731-4740.
- [76] Y. Ryo, S. Hidetada, U. Kohei, Solvent effect on the structure of the self-assembled monolayer of alkanethiol, *Chemistry Letters* 28(7) (1999) 667-668.
- [77] S.D. Techane, L.J. Gamble, D.G. Castner, Multitechnique characterization of self-assembled carboxylic acid-terminated alkanethiol monolayers on nanoparticle and flat gold surfaces, *The Journal of Physical Chemistry C* 115(19) (2011) 9432-9441.
- [78] W.A. Marmisollé, D.A. Capdevila, E. de la Llave, F.J. Williams, D.H. Murgida, Self-assembled monolayers of  $\text{NH}_2$ -terminated thiols: order, pKa, and specific adsorption, *Langmuir* 29(17) (2013) 5351-5359.

- [79] H. Finklea, Electrochemistry of organized monolayers of thiols and related molecules on electrodes, *Electroanalytical Chemistry: A Series of Advances*, 19 19 (1996) 109-335.
- [80] C. Vericat, M.E. Vela, R.C. Salvarezza, Self-assembled monolayers of alkanethiols on Au(111): Surface structures, defects and dynamics, *Physical Chemistry Chemical Physics* 7(18) (2005) 3258-3268.
- [81] M.C. Daniel, D. Astruc, Gold nanoparticles: Assembly, supramolecular chemistry, quantum-size-related properties, and applications toward biology, catalysis, and nanotechnology, *Chemical Reviews* 104(1) (2004) 293-346.
- [82] C.D. Bain, H.A. Biebuyck, G.M. Whitesides, Comparison of self-assembled monolayers on gold: Coadsorption of thiols and disulfides, *Langmuir* 5(3) (1989) 723-727.
- [83] J.F. Kang, S. Liao, R. Jordan, A. Ulman, Mixed self-assembled monolayers of rigid biphenyl thiols: Impact of solvent and dipole moment, *Journal of the American Chemical Society* 120(37) (1998) 9662-9667.
- [84] W.H. Chuang, J.C. Lin, Surface characterization and platelet adhesion studies for the mixed self-assembled monolayers with amine and carboxylic acid terminated functionalities, *Journal of Biomedical Materials Research Part A* 82A(4) (2007) 820-830.
- [85] L. Yan, C. Marzolin, A. Terfort, G.M. Whitesides, Formation and reaction of interchain carboxylic anhydride groups on self-assembled monolayers on gold, *Langmuir* 13(25) (1997) 6704-6712.
- [86] P. Marquet, G. Andersson, A. Snedden, L. Kloo, R. Atkin, Molecular scale characterization of the titania-dye-solvent interface in dye-sensitized solar cells, *Langmuir* 26(12) (2010) 9612-9616.
- [87] A. Hagfeldt, M. Grätzel, Molecular photovoltaics, *Accounts of Chemical Research* 33(5) (2000) 269-277.
- [88] A. J. Frank, N. Kopidakis, J.v.d. Lagemaat, Electrons in nanostructured TiO<sub>2</sub> solar cells: Transport, recombination and photovoltaic properties, *Coordination Chemistry Reviews* 248(13-14) (2004) 1165-1179.
- [89] C.-Y. Lin, Y.H. Lai, H.W. Chen, J.G. Chen, C.W. Kung, R. Vittal, K.C. Ho, Highly efficient dye-sensitized solar cell with a ZnO nanosheet-based photoanode, *Energy & Environmental Science* 4(9) (2011) 3448-3455.
- [90] A. Birkel, Y.G. Lee, D. Koll, X.V. Meerbeek, S. Frank, M.J. Choi, Y.S. Kang, K. Char, W. Tremel, Highly efficient and stable dye-sensitized solar cells based on SnO<sub>2</sub> nanocrystals prepared by microwave-assisted synthesis, *Energy & Environmental Science* 5(1) (2012) 5392-5400.
- [91] D.P. Hagberg, T. Marinado, K.M. Karlsson, K. Nonomura, P. Qin, G. Boschloo, T. Brinck, A. Hagfeldt, L. Sun, Tuning the HOMO and LUMO energy levels of organic chromophores for dye sensitized solar cells, *The Journal of Organic Chemistry* 72(25) (2007) 9550-9556.
- [92] C.R. Zhang, L. Liu, J.W. Zhe, N.Z. Jin, Y. Ma, L.H. Yuan, M.L. Zhang, Y.Z. Wu, Z.J. Liu, H.S. Chen, The role of the conjugate bridge in electronic structures and related properties of tetrahydroquinoline for dye sensitized solar cells, *International journal of molecular sciences* 14(3) (2013) 5461-5481.



- [93] K.M. Karlsson, X. Jiang, S.K. Eriksson, E. Gabrielsson, H. Rensmo, A. Hagfeldt, L. Sun, Phenoxazine dyes for dye-sensitized solar cells: Relationship between molecular structure and electron lifetime, *Chemistry-A European Journal* 17(23) (2011) 6415-6424.
- [94] A. Hagfeldt, G. Boschloo, L. Sun, L. Kloo, H. Pettersson, Dye-sensitized solar cells, *Chemical reviews* 110(11) (2010) 6595-6663.
- [95] C. Yasuo, I. Ashraful, W. Yuki, K. Ryoichi, K. Naoki, H. Liyuan, Dye-sensitized solar cells with conversion efficiency of 11.1%, *Japanese Journal of Applied Physics* 45(7L) (2006) L638.
- [96] H.A. Harms, N. Tetreault, V. Gusak, B. Kasemo, M. Gratzel, In situ investigation of dye adsorption on TiO<sub>2</sub> films using a quartz crystal microbalance with a dissipation technique, *Physical Chemistry Chemical Physics* 14(25) (2012) 9037-9040.
- [97] D. Attwood, *Soft x-rays and extreme ultraviolet radiation: principles and applications*, Cambridge university press 2007.
- [98] M.P. Seah, W.A. Dench, Quantitative electron spectroscopy of surfaces: A standard data base for electron inelastic mean free paths in solids, *Surface and Interface Analysis* 1(1) (1979) 2-11.
- [99] M. Seah, W. Dench, Quantitative electron spectroscopy of surfaces: a standard data base for electron inelastic mean free paths in solids, *Surface and interface analysis* 1(1) (1979) 2-11.
- [100] C. Davisson, L.H. Germer, Diffraction of electrons by a crystal of nickel, *Physical Review* 30(6) (1927) 705-740.
- [101] J. Drelich, J.D. Miller, R.J. Good, The effect of drop (bubble) size on advancing and receding contact angles for heterogeneous and rough solid surfaces as observed with sessile-drop and captive-bubble techniques, *Journal of Colloid and Interface Science* 179(1) (1996) 37-50.
- [102] J.J.I. Ramos, S.E. Moya, Water content of hydrated polymer brushes measured by an in situ combination of a quartz crystal microbalance with dissipation monitoring and spectroscopic ellipsometry, *Macromolecular Rapid Communications* 32(24) (2011) 1972-1978.
- [103] M. Rodahl, B. Kasemo, A simple setup to simultaneously measure the resonant frequency and the absolute dissipation factor of a quartz crystal microbalance, *Review of Scientific Instruments* 67(9) (1996) 3238-3241.
- [104] G. Sauerbrey, Verwendung von Schwingquarzen zur Wägung dünner Schichten und zur Mikrowägung, *Zeitschrift für Physik* 155(2) (1959) 206-222.
- [105] F. Höök, B. Kasemo, T. Nylander, C. Fant, K. Sott, H. Elwing, Variations in coupled water, viscoelastic properties, and film thickness of a Mefp-1 protein film during adsorption and cross-linking: A quartz crystal microbalance with dissipation monitoring, ellipsometry, and surface plasmon resonance study, *Analytical Chemistry* 73(24) (2001) 5796-5804.
- [106] M. Rodahl, F. Hook, C. Fredriksson, C. A. Keller, A. Krozer, P. Brzezinski, M. Voinova, B. Kasemo, Simultaneous frequency and dissipation factor QCM measurements of biomolecular adsorption and cell adhesion, *Faraday Discussions* 107(0) (1997) 229-246.

- [107] M.V. Voinova, M. Rodahl, M. Jonson, B. Kasemo, Viscoelastic acoustic response of layered polymer films at fluid-solid interfaces: Continuum mechanics approach, *Physica Scripta* 59(5) (1999) 391.
- [108] K. Keiji Kanazawa, J.G. Gordon II, The oscillation frequency of a quartz resonator in contact with liquid, *Analytica Chimica Acta* 175 (1985) 99-105.
- [109] B. Pittenger, N. Erina, C. Su, Quantitative mechanical property mapping at the nanoscale with PeakForce QNM, Application Note Veeco Instruments Inc.
- [110] E. Thormann, T. Pettersson, P.M. Claesson, How to measure forces with atomic force microscopy without significant influence from nonlinear optical lever sensitivity, *Review of Scientific Instruments* 80(9) (2009) 093701.
- [111] C.P. Green, H. Lioe, J.P. Cleveland, R. Proksch, P. Mulvaney, J.E. Sader, Normal and torsional spring constants of atomic force microscope cantilevers, *Review of Scientific Instruments* 75(6) (2004) 1988-1996.
- [112] B. Cappella, G. Dietler, Force-distance curves by atomic force microscopy, *Surface Science Reports* 34(1-3) (1999) 1-104.
- [113] J. Wintterlin, R. Behm, H. Güntherodt, R. Wiesendanger, *Scanning Tunneling Microscopy I*, Vol. 1 Springer, Berlin (1992).
- [114] T. Sawaguchi, Y. Sato, F. Mizutani, Ordered structures of self-assembled monolayers of 3-mercaptopropionic acid on Au(111): In situ scanning tunneling microscopy study, *Physical Chemistry Chemical Physics* 3(16) (2001) 3399-3404.
- [115] H. Wang, S. Chen, L. Li, S. Jiang, Improved method for the preparation of carboxylic acid and amine terminated self-assembled monolayers of alkanethiolates, *Langmuir* 21(7) (2005) 2633-2636.
- [116] E. Jagst, Surface functional group characterization using chemical derivatization X-ray photoelectron spectroscopy (CD-XPS), BAM Bundesanstalt für Materialforschung und -prüfung, Berlin, 2011.
- [117] W.C. Lin, S.H. Lee, M. Karakachian, B.-Y. Yu, Y.Y. Chen, Y.C. Lin, C.H. Kuo, J.J. Shyue, Tuning the surface potential of gold substrates arbitrarily with self-assembled monolayers with mixed functional groups, *Physical Chemistry Chemical Physics* 11(29) (2009) 6199-6204.
- [118] M. Ryadnov, E. Farkas, *Amino Acids, Peptides and Proteins*, Royal Society of Chemistry 2014.
- [119] J. Schmalisch, O. Seitz, Acceleration of thiol additive-free native chemical ligation by intramolecular S → S acyl transfer, *Chemical Communications* 51(35) (2015) 7554-7557.
- [120] E.E. Bedford, S. Boujday, V. Humblot, F.X. Gu, C.-M. Pradier, Effect of SAM chain length and binding functions on protein adsorption:  $\beta$ -lactoglobulin and apotransferrin on gold, *Colloids and Surfaces B: Biointerfaces* 116 (2014) 489-496.
- [121] J.A. Tamada, A.S. Kertes, C.J. King, Extraction of carboxylic acids with amine extractants. 1. Equilibria and law of mass action modeling, *Industrial & Engineering Chemistry Research* 29(7) (1990) 1319-1326.
- [122] T.L. Lebedeva, G.A. Shandryuk, T.I. Sycheva, V.S. Bezborodov, R.V. Talroze, N.A. Platé, Structure of  $\beta$ -N-dimethylamino-4-dodecyloxypropylphenone complexes with di- and polycarboxylic acids, *Journal of Molecular Structure* 354(2) (1995) 89-96.

- [123] K. Wang, Z. Chang, Y. Ma, C. Lei, S. Jin, Y. Wu, I. Mahmood, C. Hua, H. Liu, Equilibrium study on reactive extraction of propionic acid with N1923 in different diluents, *Fluid Phase Equilibria* 278(1–2) (2009) 103-108.
- [124] E.A. Yerger, G.M. Barrow, Acid-base reactions in non-dissociating solvents. Acetic acid and diethylamine in carbon tetrachloride and chloroform, *Journal of the American Chemical Society* 77(17) (1955) 4474-4481.
- [125] J.A. Tamada, C.J. King, Extraction of carboxylic acids with amine extractants. 2. Chemical interactions and interpretation of data, *Industrial & Engineering Chemistry Research* 29(7) (1990) 1327-1333.
- [126] S.R. Holmes-Farley, R.H. Reamey, T.J. McCarthy, J. Deutch, G.M. Whitesides, Acid-base behavior of carboxylic acid groups covalently attached at the surface of polyethylene: The usefulness of contact angle in following the ionization of surface functionality, *Langmuir* 1(6) (1985) 725-740.
- [127] M.C. Leopold, J.A. Black, E.F. Bowden, Influence of gold topography on carboxylic acid terminated self-assembled monolayers, *Langmuir* 18(4) (2002) 978-980.
- [128] M.L. Carot, V.A. Macagno, P. Paredes-Olivera, E.M. Patrino, Structure of mixed carboxylic acid terminated self-assembled monolayers: Experimental and theoretical investigation, *The Journal of Physical Chemistry C* 111(11) (2007) 4294-4304.
- [129] J. Li, K.S. Liang, G. Scoles, A. Ulman, Counterion overlayers at the interface between an electrolyte and an  $\omega$ -functionalized monolayer self-assembled on gold. An X-ray reflectivity study, *Langmuir* 11(11) (1995) 4418-4427.
- [130] X. Zhai, H. Lee, T. Tian, T. Lee, J. Garino, Nanoscale lithography mediated by surface self-assembly of 16-[3,5-Bis(Mercaptomethyl) phenoxy] hexadecanoic acid on Au(111) investigated by scanning probe microscopy, *Molecules* 19(9) (2014) 13010.
- [131] S. Xu, S. Miller, P.E. Laibinis, G.y. Liu, Fabrication of nanometer scale patterns within self-assembled monolayers by nanografting, *Langmuir* 15(21) (1999) 7244-7251.
- [132] L. Cai, Y. Yao, J. Yang, D.W. Price, J.M. Tour, Chemical and potential-assisted assembly of thiolacetyl-terminated oligo(phenylene ethynylene)s on gold surfaces, *Chemistry of Materials* 14(7) (2002) 2905-2909.
- [133] M.H. Dishner, J.C. Hemminger, F.J. Feher, Scanning tunneling microscopy characterization of organoselenium monolayers on Au(111), *Langmuir* 13(18) (1997) 4788-4790.
- [134] M.H. Dishner, J.C. Hemminger, F.J. Feher, Formation of a self-assembled monolayer by adsorption of thiophene on Au(111) and its photooxidation, *Langmuir* 12(26) (1996) 6176-6178.
- [135] M.J. Tarlov, D.R.F. Burgess, G. Gillen, UV photopatterning of alkanethiolate monolayers self-assembled on gold and silver, *Journal of the American Chemical Society* 115(12) (1993) 5305-5306.
- [136] J. Ossowski, T. Wächter, L. Silies, M. Kind, A. Noworolska, F. Blobner, D. Gnatek, J. Rysz, M. Bolte, P. Feulner, Thiolate versus selenolate: structure, stability, and charge transfer properties, *ACS nano* 9(4) (2015) 4508-4526.
- [137] Y. Tong, T. Jiang, A. Bendounan, M.N.K. Harish, A. Giglia, S. Kubsy, F. Sirotti, L. Pasquali, S. Sampath, V.A. Esaulov, Case studies on the formation of chalcogenide

self-assembled monolayers on surfaces and dissociative processes, *Beilstein Journal of Nanotechnology* 7(1) (2016) 263-277.

[138] L.V. Romashov, V.P. Ananikov, Self-assembled selenium monolayers: From nanotechnology to materials science and adaptive catalysis, *Chemistry – A European Journal* 19(52) (2013) 17640-17660.

[139] A. Shaporenko, A. Ulman, A. Terfort, M. Zharnikov, Self-assembled monolayers of alkaneselenolates on (111) gold and silver, *The Journal of Physical Chemistry B* 109(9) (2005) 3898-3906.

[140] K. Heister, M. Zharnikov, M. Grunze, L.S.O. Johansson, Adsorption of alkanethiols and biphenylthiols on Au and Ag substrates: A high-resolution X-ray photoelectron spectroscopy study, *The Journal of Physical Chemistry B* 105(19) (2001) 4058-4061.

[141] J.J. Yeh, I. Lindau, Atomic subshell photoionization cross sections and asymmetry parameters, *Atomic Data and Nuclear Data Tables* 32(1) (1985) 1-155.

[142] F. Cometto, E. Patrito, P. Paredes Olivera, G. Zampieri, H. Ascolani, Electrochemical, high-resolution photoemission spectroscopy and vdW-DFT study of the thermal stability of benzenethiol and benzeneselenol monolayers on Au (111), *Langmuir* 28(38) (2012) 13624-13635.

[143] F.P. Cometto, C.A. Calderón, M. Morán, G. Ruano, H. Ascolani, G. Zampieri, P. Paredes-Olivera, E.M. Patrito, Formation, characterization, and stability of methaneselenolate monolayers on Au(111): An electrochemical high-resolution photoemission spectroscopy and DFT study, *Langmuir* 30(13) (2014) 3754-3763.

[144] M. Bowker, Introduction to surface chemistry and catalysis. By Gabor A. Somorjai, Wiley, Chichester, UK 1994, XXIV, 667 pp., hardcover, ISBN 0-471-03192-5, *Chemical Vapor Deposition* 1(3) (1995) 90-90.

[145] J.R. Mann, M.K. Gannon, T.C. Fitzgibbons, M.R. Detty, D.F. Watson, Optimizing the photocurrent efficiency of dye-sensitized solar cells through the controlled aggregation of chalcogenoxanthylum dyes on nanocrystalline titania films, *The Journal of Physical Chemistry C* 112(34) (2008) 13057-13061.

[146] B. O'Regan, M. Gratzel, A low-cost, high-efficiency solar cell based on dye-sensitized colloidal TiO<sub>2</sub> films, *Nature* 353(6346) (1991) 737-740.

[147] A. Kay, M. Grätzel, Dye-sensitized core-shell nanocrystals: Improved efficiency of mesoporous tin oxide electrodes coated with a thin layer of an insulating oxide, *Chemistry of Materials* 14(7) (2002) 2930-2935.

[148] L. Ellis-Gibbings, V. Johansson, R.B. Walsh, L. Kloo, J.S. Quinton, G.G. Andersson, Formation of N719 dye multilayers on dye sensitized solar cell photoelectrode surfaces investigated by direct determination of element concentration depth profiles, *Langmuir* 28(25) (2012) 9431-9439.

[149] V. Gusak, E. Nkurunziza, C. Langhammer, B. Kasemo, Real-time adsorption and desorption kinetics of dye Z907 on a flat mimic of dye-sensitized solar cell TiO<sub>2</sub> photoelectrodes, *The Journal of Physical Chemistry C* 118(30) (2014) 17116-17122.

[150] T. Kitamura, M. Ikeda, K. Shigaki, T. Inoue, N.A. Anderson, X. Ai, T. Lian, S. Yanagida, Phenyl-conjugated oligoene sensitizers for TiO<sub>2</sub> solar cells, *Chemistry of Materials* 16(9) (2004) 1806-1812.

[151] S. Yu, S. Ahmadi, M. Zuleta, H. Tian, K. Schulte, A. Pietzsch, F. Hennies, J. Weissenrieder, X. Yang, M. Göthelid, Adsorption geometry, molecular interaction,

- and charge transfer of triphenylamine-based dye on rutile  $\text{TiO}_2(110)$ , *The Journal of Chemical Physics* 133(22) (2010) 224704.
- [152] H. Idriss, E.G. Seebauer, Reactions of ethanol over metal oxides, *Journal of Molecular Catalysis A: Chemical* 152(1–2) (2000) 201–212.
- [153] J. Weissenrieder, J. Gustafson, D. Stacchiola, Reactivity and mass transfer of low-dimensional catalysts, *The Chemical Record* 14(5) (2014) 857–868.
- [154] A. Soon, M. Todorova, B. Delley, C. Stampfl, Thermodynamic stability and structure of copper oxide surfaces: A first-principles investigation, *Physical Review B* 75(12) (2007) 125420.
- [155] M.M. Islam, B. Diawara, V. Maurice, P. Marcus, Surface reconstruction modes of  $\text{Cu}_2\text{O}(001)$  surface: A first principles study, *Surface Science* 604(17–18) (2010) 1516–1523.
- [156] I.J. Drake, K.L. Fajdala, A.T. Bell, T.D. Tilley, Dimethyl carbonate production via the oxidative carbonylation of methanol over  $\text{Cu}/\text{SiO}_2$  catalysts prepared via molecular precursor grafting and chemical vapor deposition approaches, *Journal of Catalysis* 230(1) (2005) 14–27.
- [157] C. Leygraf, T. Graedel, *Atmospheric Corrosion* John Wiley, New York.
- [158] A. Soon, M. Todorova, B. Delley, C. Stampfl, Surface oxides of the oxygen–copper system: Precursors to the bulk oxide phase?, *Surface Science* 601(24) (2007) 5809–5813.
- [159] K.H. Schulz, D.F. Cox, Propene oxidation over  $\text{Cu}_2\text{O}$  single-crystal surfaces: A surface science study of propene activation at 1 atm and 300 K, *Journal of Catalysis* 143(2) (1993) 464–480.
- [160] D.F. Cox, K.H. Schulz, Methanol decomposition on single crystal  $\text{Cu}_2\text{O}$ , *Journal of Vacuum Science & Technology A* 8(3) (1990) 2599–2604.
- [161] E.I. Solomon, P.M. Jones, J.A. May, Electronic structures of active sites on metal oxide surfaces: Definition of the copper-zinc oxide methanol synthesis catalyst by photoelectron spectroscopy, *Chemical Reviews* 93(8) (1993) 2623–2644.
- [162] Z. Riguang, L. Hongyan, L. Lixia, L. Zhong, W. Baojun, A DFT study on the formation of  $\text{CH}_3\text{O}$  on  $\text{Cu}_2\text{O}(1\ 1\ 1)$  surface by  $\text{CH}_3\text{OH}$  decomposition in the absence or presence of oxygen, *Applied Surface Science* 257(9) (2011) 4232–4238.
- [163] P.M. Jones, J.A. May, J.B. Reitz, E.I. Solomon, Electron spectroscopic studies of  $\text{CH}_3\text{OH}$  chemisorption on  $\text{Cu}_2\text{O}$  and  $\text{ZnO}$  single-crystal surfaces: Methoxide bonding and reactivity related to methanol synthesis, *Journal of the American Chemical Society* 120(7) (1998) 1506–1516.
- [164] A. Önsten, J. Weissenrieder, D. Stoltz, S. Yu, M. Göthelid, U.O. Karlsson, Role of defects in surface chemistry on  $\text{Cu}_2\text{O}(111)$ , *The Journal of Physical Chemistry C* 117(38) (2013) 19357–19364.
- [165] D.R. Mullins, M.D. Robbins, J. Zhou, Adsorption and reaction of methanol on thin-film cerium oxide, *Surface Science* 600(7) (2006) 1547–1558.
- [166] M.S. J. H. Stenlid, A. J. Johansson, C. Leygraf, M. Göthelid, J. Weissenrieder, T. Brinck, Reactivity at the  $\text{Cu}_2\text{O}(100):\text{Cu}-\text{H}_2\text{O}$  interface: A combined DFT and PES study, *Physical Chemistry Chemical Physics* Submitted (2016).
- [167] B.Z. Sun, W.K. Chen, J.D. Zheng, C.H. Lu, Roles of oxygen vacancy in the adsorption properties of CO and NO on  $\text{Cu}_2\text{O}(1\ 1\ 1)$  surface: Results of a first-principles study, *Applied Surface Science* 255(5, Part 2) (2008) 3141–3148.